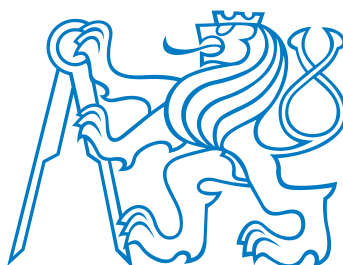


Optical measurement of displacements using subpixel image registration

Jakub Antoš

supervisor: **Václav Nežerka, Ph.D.**



Czech Technical University in Prague
Faculty of Civil Engineering

A thesis submitted for the degree of

Doctor of Philosophy

October, 2020

I would like to dedicate this thesis to my parents.

Acknowledgements

First of all, I would like to thank my supervisor Václav Nežerka for his support, encouragement, patience, and motivation. It has been a pleasure to cooperate with Václav; he has inspired me to develop new skills since my bachelor study. Next, I want to express my gratitude to Vít Šmilauer for the opportunity to participate in his project during the first twelve months of my doctoral study. Special thanks go to Pavel Tesárek, Petr Kabele, and Jiří Novák for many fruitful discussions, numerous consultations, and the opportunity to cooperate on their research projects. Last but not least, the long-term support provided by the SGS grant (Principal Investigator Daniel Rypl) and GAČR grant (Principal Investigator Petr Havlásek) are also gratefully acknowledged.

Abstract

Development of Internet-of-things (IoT) technologies opened the way for remote assessment of structural health. Such an assessment can be accomplished by monitoring relative displacements of structural elements since the imminent failure of civil engineering structures usually manifests through a loss of stiffness and hence excessive displacements under static loading or change in vibration frequencies due to dynamic excitation.

With these facts in mind, an open-source tool for real-time measurement of relative displacements based on image registration was developed. The use of upsampled matrix-multiplication discrete Fourier transform and measurement limited to pre-defined points of interest by virtual extensometers allowed high sampling frequencies with subpixel accuracy. The accuracy of the system with respect to a physical length-scale was assessed, and the software was successfully verified through experimental testing in a laboratory.

Besides the proof-of-concept laboratory testing using delicate equipment, the developed software was accommodated in portable hardware to fully benefit from the lightweight algorithms. Existence of such a measurement system enabled remote monitoring of displacements and deformations outdoors. Two types of hardware solutions were tested: (i) intended for real-time measurement with a collection of data at high sampling rates and (ii) reliability-focused hardware for off-grid long-term measurements. Both solutions were tested outdoors; the first for measurement of bridge deflections due to traffic loading and the latter for monitoring of a rock massif stability.

Besides real-time measurements, the algorithms were also employed for measurements in an off-line mode. Here, the computationally efficient algorithms allowed processing of larger sequences of images recorded, e.g., using high-speed cameras.

Abstrakt

Vývoj technologií internetu věcí (IoT) otevřel cestu pro vzdálené hodnocení statického stavu konstrukcí. Takové posouzení může být provedeno monitorováním relativních posunů konstrukčních prvků, protože bezprostřední selhání stavebních konstrukcí se obvykle projevuje ztrátou tuhosti a tím i nadmernými deformacemi při statickém namáhání nebo změnou vlastních frekvencí v důsledku dynamického buzení.

Za tímto účelem byl vyvinut open-source nástroj pro měření relativních posunů v reálném čase na základě registrace obrazu. Použití diskrétní Fourierovy transformace a převzorkovanou maticí obrazu, omezené na předem vybrané body na konstrukci umožňuje vysoké vzorkovací frekvence s přesností menší, než jeden pixel. V rámci disertační práce byla posouzena přesnost systému s ohledem na fyzické měřítko a software byl úspěšně ověřen experimentálním testováním v laboratoři.

Kromě laboratorního testování k ověření funkčnosti prototypu pomocí laboratorního vybavení byl navržen přenosný hardware plně benefitující z jednoduchosti používaných algoritmů. Tento hardware byl testován v reálných podmínkách, přičemž byla ověřována funkčnost dvou řešení: (i) zařízení určené pro měření v reálném čase se shromažďováním dat při vysokých frekvencích vzorkování a (ii) hardware zaměřený na spolehlivost pro dlouhodobá měření mimo dosah elektrického napájení. Obě řešení byla testována ve venkovním prostředí; první pro měření průhybů mostů v důsledku dopravního zatížení a druhý pro monitorování stability horninového masivu.

Kromě měření v reálném čase byly algoritmy použity také pro měření v off-line režimu. Výpočtově efektivní algoritmy zde umožňovaly zpracování velkých obrazových sekvencí, např. z měření pomocí vysokorychlostních kamer.

Contents

Goals	1
1 Introduction and state of art	3
1.1 Contact measurement	3
1.1.1 Strain gauges	4
1.1.2 LVDTs	5
1.2 Non-contact measurement	5
1.3 Digital image correlation	6
1.3.1 DIC principles	8
1.3.2 Real-time DIC	11
2 Digital image acquisition	13
2.1 Aperture	13
2.2 Shutter speed	14
2.3 ISO number	14
2.4 Lenses	15
2.5 Image compression and file formats	16
3 Image registration	19
3.1 Fourier transform	19
3.2 Phase correlation	21
3.3 Subpixel registration	23
4 Assessment of stochastic patterns for DIC	27
4.1 Assessment criteria	28
4.1.1 Normalized cross-correlation	28
4.1.2 Mean intensity gradient	28

4.1.3	Shannon entropy	29
4.2	Assessment of patterns and textures	29
4.3	Virtual Stretching of Patterns and Textures	33
5	Hardware	35
5.1	Basic components for measurements	35
5.1.1	Camera	35
5.1.2	Lenses	36
5.1.3	Camera mounting	37
5.1.4	Computing unit	38
5.2	Real-time measurement at high sampling rates	38
5.3	Remote long-term monitoring	39
6	Real-time measurements	45
6.1	Algorithms and program work flow	46
6.1.1	Sub-pixel registration	46
6.1.2	Registration of large displacements	48
6.2	Testing and validation	48
6.2.1	Measurement bias	49
6.2.2	Experimental verification	52
6.2.3	Outdoor measurements	52
7	Off-line mode measurements	57
7.1	Audio recovery	57
7.2	Modal analysis	58
8	Conclusions and Final Remarks	61
Research outcomes		63
References		65

Goals

The main objective of the presented research was to develop a solution capable of optical real-time measurement of displacements/deformations at high sampling rates. To achieve these goals, it was necessary to divide the research into the following sub-goals:

- Review state-of-the-art technologies and algorithms and find a niche in the area of real-time optical measurements, Chapters [1](#) and [2](#),
- Develop and validate software tools for computationally efficient calculation of displacement and deformations, suitable for real-time measurement, Chapter [3](#),
- Find suitable criteria for the assessment of stochastic patterns for DIC measurements, Chapter [4](#),
- Design suitable hardware for autonomous monitoring of structural movements/deformations and data transfer, Chapter [5](#),
- Present practical use and results of the developed solutions, Chapter [6](#) and [7](#).

Chapter 1

Introduction and state of art

Recent failures of several bridges^{1,2} have led to a discussion about the evaluation of safety and the need for a continuous assessment of structural health. Displacements at critical points under a certain loading condition provide crucial information about deterioration and their monitoring can alert people in case of suspicious behavior [1, 2]. The validity of this statement is not limited to bridges; climate changes and frequent extreme weather episodes in some geographical locations may cause problems not only on building or civil engineering structures [3] but also with the stability of slopes [4, 5]. In addition, monitoring of displacement fields on existent structures can be very useful in case of any human interventions, such as excavation works, in the neighborhood.

The imminent failure of a load-bearing structure can be manifested through a loss of stiffness and hence excessive displacements under static loading [6–8] or change in vibration frequencies due to dynamic excitation [9]. However, measuring these displacements or frequencies is not easy, since for example, most bridges overpass a river or sea where installation of conventional measurement instrumentation is extremely inconvenient or nearly impossible.

These issues are even more pronounced in the case of long-term measurements, e.g., for continuous health monitoring. Long-term monitoring of structures requires a reliable and cheap solution with easily accessible results on-line. These requirements can be fulfilled by employing optical measurements with cameras connected to a computer capable of sending data on a cloud server. Despite relatively straightforward principles, such devices are not commonly employed outdoors and even commercial solutions are usually restricted to a laboratory use. Before diving into the developments of such a measurement solution, an overview of techniques and principles adopted in the measurement of displacements and deformations is provided next.

1.1 Contact measurement

Contact measurement techniques have been traditionally exploited in structural assessment, but their use is often challenging in terms of measurement accuracy. Moreover, their installation is

¹<https://www.bbc.com/news/world-europe-45241842>

²<https://www.dw.com/en/prague-bridge-collapse-leaves-4-injured/a-41629175>

often laborious and requires a sufficiently flat surface allowing the use of adhesives or drilling. Yet, in some cases, their superior accuracy to other measurement techniques, scalability, and the possibility to embed devices for contact-based measurement of deformations makes contact measurement indispensable.

1.1.1 Strain gauges

Strain gauges or linear variable differential transformers (LVDTs) [10] are the most commonly used instruments for contact measurement of strains and displacements. A principle of strain gauge measurement was first described by Edward E. Simmons and Arthur C. Ruge in 1938 [11]. The principle is based on detecting changes in electric resistance of a gauge grid due to its deformation (elongation). The most widely used metallic strain gauge consists of a fine wire (thickness approximately 0.025 mm) or metallic foil arranged in a regular pattern. Strain gauges must be connected to an electric circuit and usually employ three additional resistors to form a Wheatstone bridge circuit (Figure 1.1). This pattern is designed in such a way to maximize the amount of a metal to be subjected to elongation/shortening when the gauge is deformed. The cross-sectional area of a grid is minimized to reduce the impacts of shear strain and Poisson ratio. Strain gauges are reinforced by a foil to which metal grids are bonded using adhesives. This backing foil, called a carrier, must be attached directly to a test specimen surface. Therefore, strain experienced by the test specimen is transferred directly to the strain gauge, which responds with a linear change in electrical resistance [12]. This resistance is calculated based on recorded voltage. Therefore, proper attachment of a strain gauge to a surface of tested structures is of the greatest importance and the interface is usually the weakest link in the system [13].

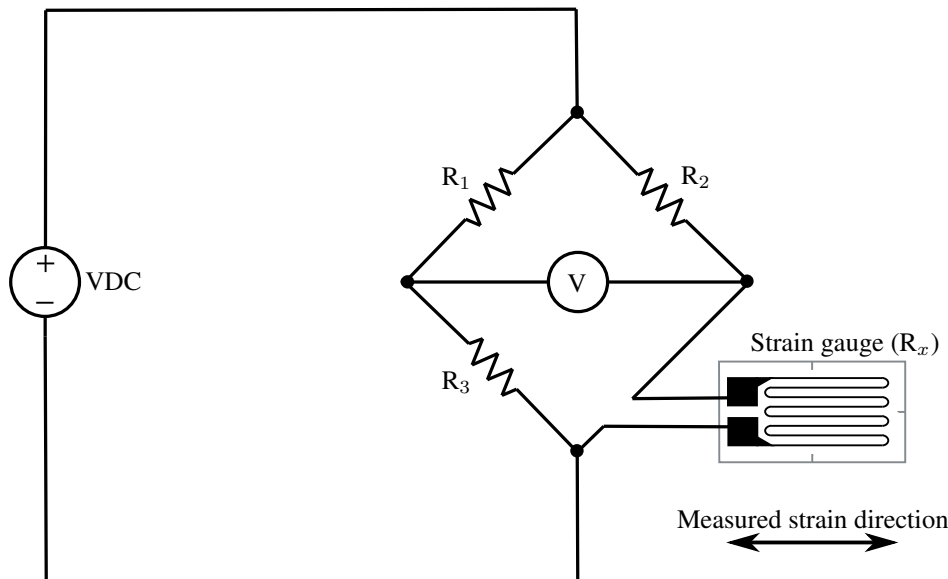


Figure 1.1: Scheme of a quarter-bridge strain gauge basic circuit, where volts direct current (VDC) represents a source of direct current, R_1 , R_2 , R_3 , and R_x (the strain gauge) represent resistors, and V is a voltmeter.

When selecting a suitable strain gauge for a given application, it is necessary to consider

not only the characteristics of the sensor, but also its stability and temperature sensitivity. Since materials used in strain gauges are sensitive to temperature changes, long-term measurements require employing additional unloaded strain gauge for compensation. There are numerous drawbacks associated with the use of strain gauges that must be kept in mind. It was reported by Koval and Boiko [14] that strain-gauges that can suffer from fatigue. Moreover, imperfect attachment to the measured surface can significantly influence the measurement accuracy [15, 16] and the additional stiffness can influence the behavior of compliant specimens [17].

1.1.2 LVDTs

Unlike strain gauges capable of measuring local deformations, linear variable differential transformers (LVDTs) can be used for the measurement of relative displacements at discrete points. Their measurement range is limited only by the production technology and, in theory, it is fully scalable. The advantage of using LVDT displacement transducers is that the moving core does not have any contact with other electrical components of the assembly and thus it offers high reliability and long life. LVDTs are temperature independent, but the entire sensor must be shielded to prevent misreadings due to sensitivity to magnetic fields.

In the simplest form, LVDT consists of a cylindrical array of a primary and secondary coils with a separate cylindrical core passing through a center of the sensor body (Figure 1.2). The primary coil is powered by a constant amplitude of alternating current (AC) supply at a frequency of 1 kHz to 10 kHz. This produces an alternating magnetic field in the center of the transducer which induces a signal into the secondary coils. The amplitude of the magnetic field depends on the position of the movable core that is attached to the measured surface. The winding of the coils is such that the signal output has a linear relationship with the movement of the core. The secondary output signal can be then processed by a phase-sensitive demodulator which is switched at the same frequency as the primary current supply. The final output, after rectification and filtering, generates a direct current proportional to the core movement and also indicates its direction, positive or negative from the central zero point [18].

1.2 Non-contact measurement

Non-contact measurement methods can be generally categorized on those based on laser technology [19], radars [20], GPS [21], or video/digital image processing [22–26]. In some applications, it is advantageous to combine these technologies in order to increase the performance and reliability of measurement [27]. Unlike conventional contact-based methods, non-contact techniques are capable of capturing even the most complex deformation until the ultimate failure of the tested specimen/structure [28, 29].

Even though radar-based technology has been successfully adopted for structural health monitoring [20, 30, 31] as well as less accurate GPS tracking [32–34], laser sensors are discussed here for their similarity to optical measurements, being the subject of this thesis. These sensors exploit laser light propagation and reflection from a measured object; the distance of a monitored surface changes an angle of a reflected laser beam, which is received on a sensor [35] (Figure 1.3). It is obvious that the measurement accuracy can be negatively affected

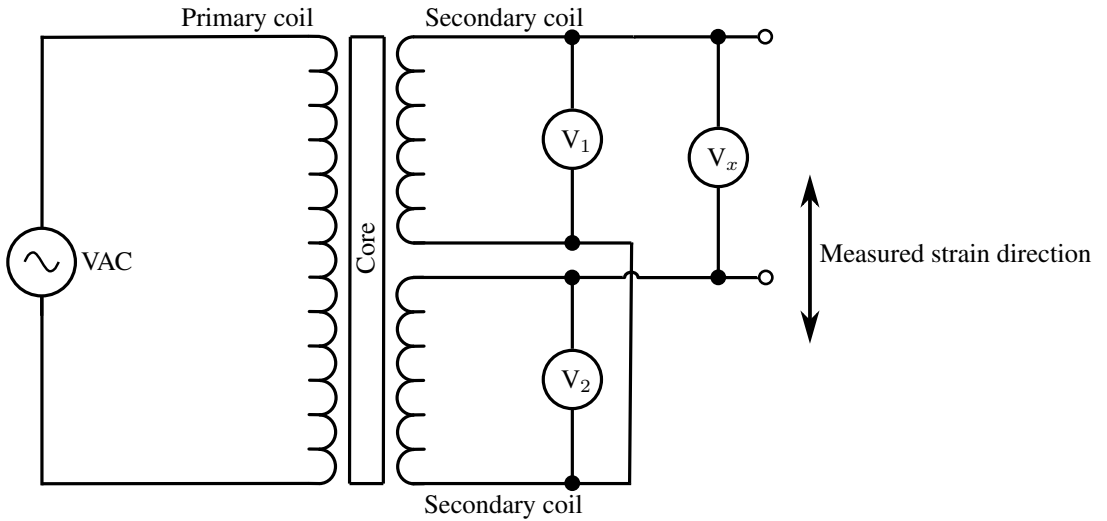


Figure 1.2: Scheme of an LVDT displacement sensor basic circuit, where volts alternating current (VAC) represents a source of alternating current and V_1 and V_2 are voltmeters; the difference in voltage on these voltmeters is proportional to a measured displacement.

and the installation of such a measurement line requires a seasoned operator. On the other hand, if conducted properly, the measurements are very accurate and the use of programmable logic controllers (PLCs) allows to compensate temperature changes [36].

The reflected laser beam is usually captured using a charge-coupled device (CCD) or a complementary metal-oxide-semiconductor (CMOS). These are light-sensitive integrated circuits that store and display image data in such a way that each pixel within the image is converted into an electrical charge. The charge is proportional to the light intensity and CCD/CMOS sensors are capable of detecting a peak of the light intensity distribution on a sensor pixel array. In addition to observing object translations, time-of-flight technology employing pulsing transmitter diode and a sensitive laser energy detector allow calculating the distance of a measured surface from the sensor [37].

Besides digital image correlation (DIC) thoroughly described in the following text, various non-contact optical measurement methods based on interferometry exist: holography interferometry [38], speckle interferometry [39], and moiré interferometry [40]. These methods allow for computing displacement fields, but with the development of DIC they lose their significance [41]. The same applies for the non-interferometric full-field grid method [42].

1.3 Digital image correlation

DIC technique enables evaluating kinematic fields from a series of digital images. The development of DIC benefited from the rapid development of digital cameras and computers in the last decade of 20th century. DIC principles were first proposed by Yamaguchi [43] and Peters and Ranson [44]. Since then, the method has been used in a wide range of applications, from biomechanics [45, 46] to structural mechanics [47, 48] or dynamics [49], and across multiple scales, from microscopic observations [50, 51] to large-scale structures, such as dams [52] or bridges [53].

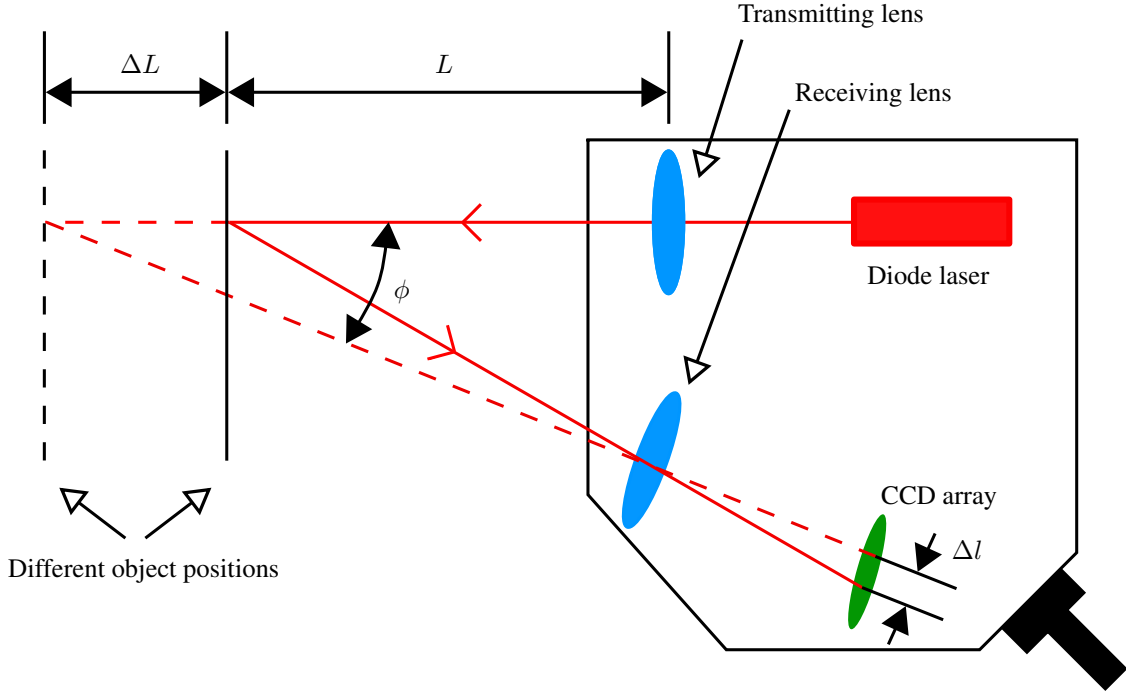


Figure 1.3: Principle of laser-based displacement measurement; ΔL is a translation distance traveled by an observed surface originally positioned at a distance L , ϕ is a reflection angle, and Δl is the change of light intensity distribution peak on a CCD array.

DIC became indispensable when monitoring and analyzing the development of kinematic fields. Besides a pure experimental assessment, knowledge of displacement and deformation fields allows us to identify global and local material parameters, validate material models, and verify numerical tools [54–56]. Unlike contact measurement techniques or laser-based measurements, DIC can capture strain localization on an observed surface, independent of a direction of principal strains [41, 57].

To ensure an accurate and reliable correlation of subsets within images, a homogeneous random pattern must be applied to the observed surface to provide gray-level variations if not present naturally [58]. The evaluation of a subset displacements and deformations is accomplished by minimizing the correlation function [59] using an optimization algorithm [60–63]. The optimization becomes more demanding with an increasing size of subsets, but subsets that are too small do not contain a sufficient number of features to track, resulting in poor correlation results [64]. Therefore, a resolution of calculated displacement/deformation fields and DIC precision are limited by image resolution and density and sharpness of the observed pattern. Besides bad settings of the subset size, lens distortions, or changes in camera temperature, unwanted camera/sample motion can introduce the most significant inaccuracies in DIC measurements [65].

Unlike 2D DIC, based on matching subsets within images to a reference one, stereo (3D) DIC operates with a series of image pairs. The images of an observed surface must be acquired by a set of a synchronized couple of cameras (or a binocular camera) and each pair of images is correlated with a reference one. 3D surface geometry is reconstructed from each couple

of images from intrinsic and extrinsic parameters using triangulation. Intrinsic parameters describe characteristics of a camera, such as an intersection between its optical axis and sensor plane, camera lens distortions, and focal length. The extrinsic parameters describe a relative position of lenses [66]. The correlation and 3D surface reconstruction provide positions of subsets within 3D space, from which 3D displacement vectors are calculated [67, 68]. Due to the impact of camera position and image distortions on results of stereo DIC, the system must be calibrated for each measurement [67, 68]. Moreover, the computational costs associated with 3D surface reconstruction make stereo DIC much more demanding than 2D DIC.

1.3.1 DIC principles

When dealing with 2D DIC, the algorithms can be divided into two categories: (i) local (subset-based) DIC [59, 69–72] and (ii) global DIC, which employs similar principles as finite element (FE) calculations and therefore also referred to as FE-based DIC [73–78]. In the local DIC, each subset is processed at a time independently without enforced continuity of displacement fields. In global DIC, a region of interest is usually discretized into elements connected by nodes. Similarly to the FE method, the displacements of all elements are evaluated simultaneously to ensure continuity of displacement fields. Wang and Pan [79] conducted a comprehensive study on the performance of local and global DIC. They reported higher displacement precision and computational efficiency of local formulations. The global DIC appears advantageous for comparisons between numerical models and experimental observations. Since comparison with computational models is not discussed in this thesis and the emphasis was put on the development of computationally efficient algorithms for local evaluation of displacements, only the principles of local DIC are presented further.

The main idea of DIC is to find a correspondence between material points, usually positioned on a regular grid, in an undeformed (reference) and a deformed (current) images. This unique correspondence cannot be found for a single pixel and therefore a correspondence of a group of pixels (a subset) located around a material point is sought. The seeking process is accomplished via finding a maximum of a correlation matrix between a current subset and a reference image. This matching procedure yields a position of the current subset within the reference image and the initial displacement with an integer-pixel accuracy is obtained. Specific algorithms to estimate displacement with a subpixel accuracy, such as non-linear optimization or curve-fitting [80], have to be employed next. After repeating this procedure for each subset and time step, the evolution of the displacement field is obtained. Due to the sensitivity of derivatives to local disturbances of differentiated fields, most DIC software employ least-squares fitting, where displacement distributions within the strain calculation window are approximated by a linear plane [62].

An example of a subset transformation is provided in Figure 1.4. Here, local coordinates (i, j) are established for points denoted as 1, 2, ..., 7 as follows

$$\mathbf{S} = [(-1, 0), (-1, 1), (0, -1), (0, 0), (0, 1), (1, -1), (1, 0)] . \quad (1.1)$$

The translation and deformation of the reference subset points to the current shape is typically expressed as a linear transformation using a first-order displacement mapping function in

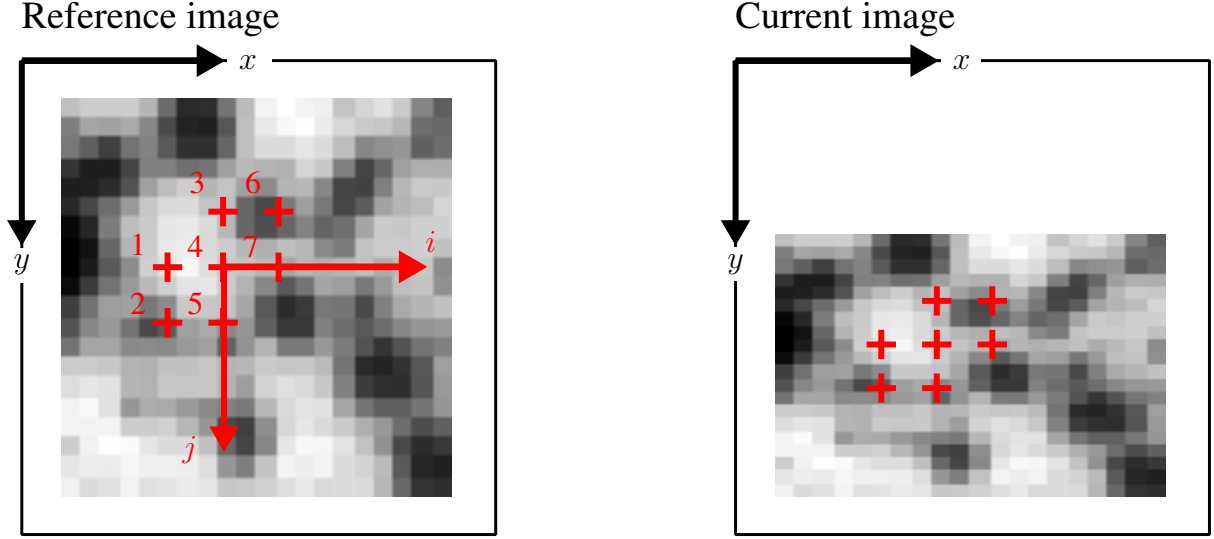


Figure 1.4: Coordinates of subset points represented by the red crosses, located within a reference and a current image.

the following form:

$$\begin{aligned}\tilde{x}_{\text{cur},i} &= x_{\text{ref},i} + u_{\text{rc}} + \frac{\partial u}{\partial x_{\text{rc}}}(x_{\text{ref},i} - x_{\text{ref},c}) + \frac{\partial u}{\partial y_{\text{rc}}}(y_{\text{ref},j} - y_{\text{ref},c}), \\ \tilde{y}_{\text{cur},j} &= y_{\text{ref},j} + v_{\text{rc}} + \frac{\partial v}{\partial x_{\text{rc}}}(x_{\text{ref},i} - x_{\text{ref},c}) + \frac{\partial v}{\partial y_{\text{rc}}}(y_{\text{ref},j} - y_{\text{ref},c}),\end{aligned}\quad (1.2)$$

where $(i, j) \in S$, $x_{\text{ref},i}$ and $y_{\text{ref},j}$ are the x and y coordinates of an initial reference subset point, $x_{\text{ref},c}$ and $y_{\text{ref},c}$ are the x and y coordinates of the center of the initial reference subset, $\tilde{x}_{\text{cur},i}$ and $\tilde{y}_{\text{cur},j}$ are the x and y coordinates of a final current subset point and $\partial u / \partial x_{\text{rc}}$, $\partial u / \partial y_{\text{rc}}$, $\partial v / \partial x_{\text{rc}}$, $\partial v / \partial y_{\text{rc}}$ are displacement gradient components, and u , v are translations of the subset center in the x and y directions, respectively. The "rc" subscript indicates that the coordinate system is transformed from reference to current.

A general form of the deformation array can be written as

$$\mathbf{p} = \begin{bmatrix} u & v & \frac{\partial u}{\partial x} & \frac{\partial u}{\partial y} & \frac{\partial v}{\partial x} & \frac{\partial v}{\partial y} \end{bmatrix}^T \quad (1.3)$$

with geometrical meaning of individual entries illustrated in Figure 1.5. Any linear combination of the six components in \mathbf{p} can be described by a warp function w , allowing for rewriting Equation (1.2) in a matrix form:

$$\xi_{\text{ref},c} + w(\Delta\xi_{\text{ref}}, \mathbf{p}_{\text{rc}}) = \begin{bmatrix} x_{\text{ref},c}^T \\ y_{\text{ref},c}^T \\ 1 \end{bmatrix} + \begin{bmatrix} 1 + \frac{\partial u}{\partial x_{\text{rc}}} & \frac{\partial u}{\partial y_{\text{rc}}} & u_{\text{rc}} \\ \frac{\partial v}{\partial x_{\text{rc}}} & 1 + \frac{\partial v}{\partial y_{\text{rc}}} & v_{\text{rc}} \\ 0 & 0 & 1 \end{bmatrix} \begin{bmatrix} \Delta x_{\text{ref}}^T \\ \Delta y_{\text{ref}}^T \\ 1 \end{bmatrix}, \quad (1.4)$$

where ξ is an augmented vector which contains the x and y coordinates of subset points, Δx and Δy are the distances between the subset points and the center of the subset, and w is a warp

function. It is necessary to allow deformation of the reference subset as follows [81]

$$\begin{aligned}\tilde{x}_{\text{ref},i} &= x_{\text{ref},i} + u_{\text{rr}} + \frac{\partial u}{\partial x_{\text{rr}}} (x_{\text{ref},i} - x_{\text{ref},c}) + \frac{\partial u}{\partial y_{\text{rr}}} (y_{\text{ref},j} - y_{\text{ref},c}), \\ \tilde{y}_{\text{ref},j} &= y_{\text{ref},j} + v_{\text{rr}} + \frac{\partial v}{\partial x_{\text{rr}}} (x_{\text{ref},i} - x_{\text{ref},c}) + \frac{\partial v}{\partial y_{\text{rr}}} (y_{\text{ref},j} - y_{\text{ref},c}),\end{aligned}\quad (1.5)$$

where $\tilde{x}_{\text{ref},i}$ and $\tilde{y}_{\text{ref},j}$ are the x and y coordinates of the final reference subset point. The subscript denotation "rr" is meant to represent the transformation from one reference coordinate system to another.

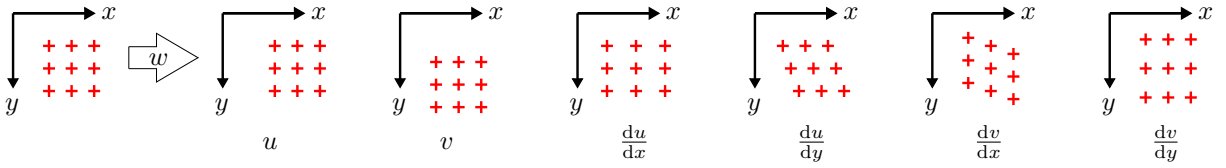


Figure 1.5: Linear transformations for subset coordinates, reproduced from [82].

The aim of DIC algorithms is to find optimal \mathbf{p}_{rc} when $\mathbf{p}_{\text{rr}} = 0$ such that the evaluated coordinates $\tilde{x}_{\text{ref},i}$ and $\tilde{y}_{\text{ref},j}$ match the coordinates $\tilde{x}_{\text{cur},i}$ and $\tilde{y}_{\text{cur},j}$.

There have been numerous similarity criteria developed for comparing gray-scale intensity distributions within a reference and current subsets, classified into categories according to their mathematical definitions: cross-correlation (CC), a sum of absolute differences (SAD), a sum of squared differences (SSD), and a parametric sum of squared differences (PSSD) [63, 72, 83–86]. For example, the most popular open-source software Ncorr [87] exploits normalized cross-correlation (NCC) metric for the initial guess when finding integer-pixel translations u and v , defined as

$$C_{\text{CC}} = \frac{\sum_{(i,j) \in S} (f(\tilde{x}_{\text{ref},i}, \tilde{y}_{\text{ref},j}) - f_m)(g(\tilde{x}_{\text{cur},i}, \tilde{y}_{\text{cur},j}) - g_m)}{\sqrt{\sum_{(i,j) \in S} [f(\tilde{x}_{\text{ref},i}, \tilde{y}_{\text{ref},j}) - f_m]^2 \sum_{(i,j) \in S} [g(\tilde{x}_{\text{cur},i}, \tilde{y}_{\text{cur},j}) - g_m]^2}}, \quad (1.6)$$

where f and g represent gray-scale values and f_m and g_m are the mean gray scale values of the reference and current subset, defined as

$$\begin{aligned}f_m &= \frac{\sum_{(i,j) \in S} f(\tilde{x}_{\text{ref},i}, \tilde{y}_{\text{ref},j})}{n(S)}, \\ g_m &= \frac{\sum_{(i,j) \in S} g(\tilde{x}_{\text{cur},i}, \tilde{y}_{\text{cur},j})}{n(S)},\end{aligned}\quad (1.7)$$

where $n(S)$ is the number of elements in S . Normalization of the cross-correlation in Equation (1.6) is necessary from practical reasons, since illumination can change during an experiment and the histogram of gray-scale values can shift towards brighter or darker shades.

In the next step, instead of maximizing C_{CC} defined in Equation (1.6), it is advantageous to optimize the subsets least-squares correlation C_{LS} introduced in Equation (1.8) to reach

$C_{\text{LS}}(\mathbf{p}_{\text{rc}}) = \text{minimum}$ [88].

$$C_{\text{LS}} = \sum_{(i,j) \in S} \left[\frac{f(\tilde{x}_{\text{ref},i}, \tilde{y}_{\text{ref},j}) - f_m}{\sqrt{\sum_{(i,j) \in S} [f(\tilde{x}_{\text{ref},i}, \tilde{y}_{\text{ref},j}) - f_m]^2}} - \frac{g(\tilde{x}_{\text{cur},i}, \tilde{y}_{\text{cur},j}) - g_m}{\sqrt{\sum_{(i,j) \in S} [g(\tilde{x}_{\text{cur},i}, \tilde{y}_{\text{cur},j}) - g_m]^2}} \right]^2. \quad (1.8)$$

Optimal \mathbf{p}_{rc} can be found using, e.g., the inverse compositional Gauss-Newton (IC-GN) method as the nonlinear optimizer [72, 89]. Full description of the optimization is beyond the scope of this work.

The Green-Lagrangian strains are obtained via displacement gradients as

$$\begin{aligned} \varepsilon_{xx} &= \frac{1}{2} \left(2 \frac{\partial u}{\partial x} + \left(\frac{\partial u}{\partial x} \right)^2 + \left(\frac{\partial v}{\partial x} \right)^2 \right), \\ \varepsilon_{xy} &= \frac{1}{2} \left(\frac{\partial u}{\partial y} + \frac{\partial v}{\partial x} + \frac{\partial u}{\partial x} \frac{\partial u}{\partial y} + \frac{\partial v}{\partial x} \frac{\partial v}{\partial y} \right), \\ \varepsilon_{yy} &= \frac{1}{2} \left(2 \frac{\partial v}{\partial y} + \left(\frac{\partial u}{\partial y} \right)^2 + \left(\frac{\partial v}{\partial y} \right)^2 \right). \end{aligned} \quad (1.9)$$

Calculation of strain fields by a numerical differentiation is usually accomplished by least-squares fitting of a plane (Equations (1.10) and (1.11)) to a strain averaging window within a displacement field to find the plane parameters used for calculating strains according to Equation (1.9). This approach renders the obtained strain field noiseless if the averaging window is large enough; on the other hand, if the averaging window is too large, strain localizations can be smoothed.

$$u_{\text{plane}}(x, y) = a_{u,\text{plane}} + \left(\frac{\partial u}{\partial x_{\text{plane}}} \right) x + \left(\frac{\partial u}{\partial y_{\text{plane}}} \right) y \quad (1.10)$$

$$v_{\text{plane}}(x, y) = a_{v,\text{plane}} + \left(\frac{\partial v}{\partial x_{\text{plane}}} \right) x + \left(\frac{\partial v}{\partial y_{\text{plane}}} \right) y \quad (1.11)$$

1.3.2 Real-time DIC

Real-time displacement and strain measurement using DIC have been tackled by a handful of authors [90–92]. Despite significantly improved efficiency of DIC provided by optimized minima-searching strategy, the reported real-time tracking rate is usually below 20 Hz. For instance, when controlling actuators during a destructive test, the evaluated region had to be limited to 15×15 pixel to enable data sampling around 10–20 Hz [93, 94].

Recently published research by Wu et al. [95] introduced a new coherent approach to DIC real-time processing, consisting of an efficient integer-pixel search scheme with a combination of an improved particle swarm optimization [96] algorithm and the block-based gradient descent search algorithm [97, 98]. Incorporated with the inverse compositional IC-GN algorithm for sub-pixel registration and parallel computing, a real-time DIC algorithm for a displacement or strain measurement during the dynamic tests could be evaluated in real-time at a rate of up to 60 Hz.

Commercial packages such as VIC-2D offer real-time DIC measurements at 11 MPx resolution images with up to 5 Hz frame rate when gathering virtual extensometer data (corresponding to the calculation of displacements at two discreet locations). Such a system is offered by Correlated Solutions³ as a complete bundle, including both software and hardware (CCD camera, tripod, and illumination). The costs of basic kit (VIC-2D SR) starts at EUR 12,000⁴.

³<http://correlatesolutions.com/>

⁴As of date December 1, 2019.

Chapter 2

Digital image acquisition

The development of high sensitivity CCD (charge-coupled device) and CMOS (complementary metal-oxide-semiconductor) matrix sensors used by most modern digital cameras contributed to the rapidly increasing popularity of DIC. These sensors convert light into electrons and capture the entire image frame at once, produce low digital noise, provide high luminance range, and enable to achieve relatively high resolutions [99]. On the other hand, there are a few drawbacks associated with their use, such as relatively high cost, increased power consumption, and quite complex construction of cameras.

One could argue that modern cell phones are capable of accommodating CMOS sensors without compromising phone construction and offer high-quality photos. But the CCD/CMOS sensor size matters in case of very delicate DIC measurements, since it determines how much light it uses to create an image. That is why large DSLR (digital single-lens reflect) cameras with sensors (see Figure 2.1) reaching full-frame size (equivalent to traditional 36×24 mm camera film window size) offer images with a high dynamic range, less noise, and improved quality when acquired in low-light conditions without artificial enhancements in a post-processing software.

2.1 Aperture

In digital photography, the term aperture is used for a lens diaphragm opening. It regulates the amount of light passing onto the sensor inside a camera when a shutter curtain opens during an exposure process. The aperture number, sometimes called f-number, does not only regulate the amount of light that passes through lens, but also affects the depth of field. Since 2D DIC is tailored for monitoring of planar surfaces, the f-number must be set to capture only projections resulting from the unevenness of a measured surface. F-number should be set with respect to the settings of shutter speed and ISO number in order to achieve proper exposure of a monitored surface.

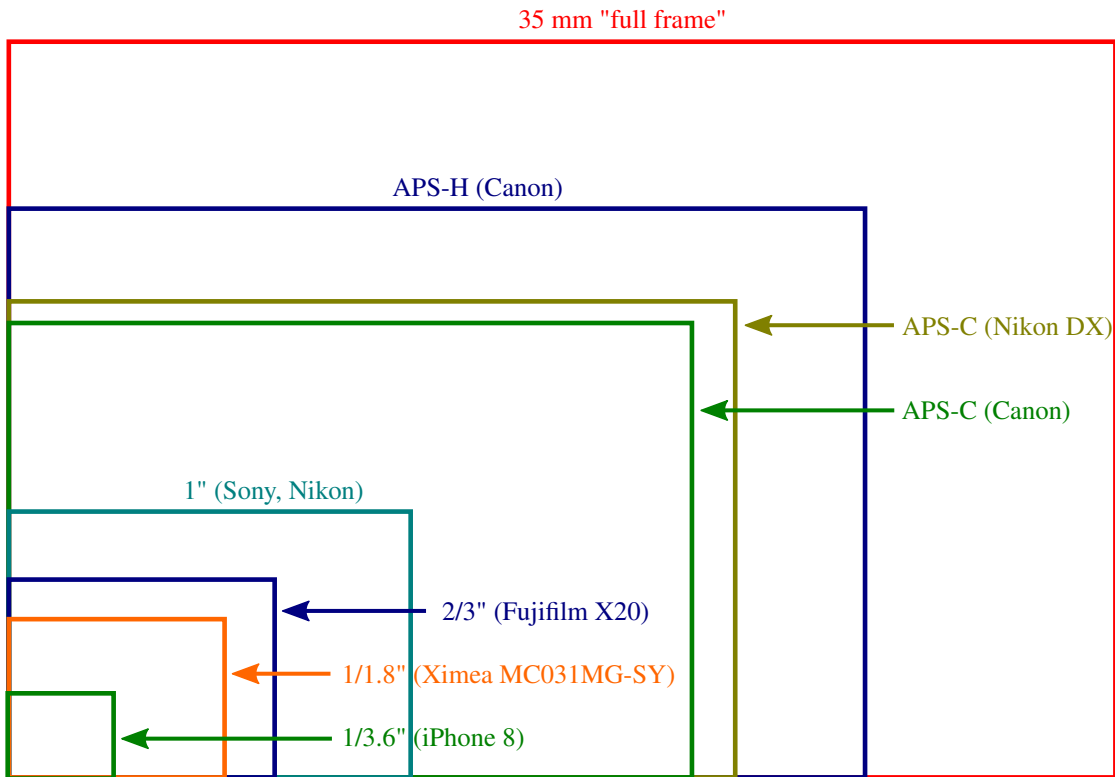


Figure 2.1: Comparative dimensions of sensor sizes.

2.2 Shutter speed

Shutter speed represents another main ingredient required to form a right exposure; it is the opening and closing time of a shutter curtain. Shutter speed has to be chosen carefully with respect to light conditions and setting of f-number in order to obtain blur-free images, needless to mention that sharpness of images is crucial for DIC analysis. In the case of quasi-static tests performed with satisfactory lighting conditions, it is recommended to have the shutter speed set to about 1/10 s. Destructive tests with an abrupt failure require extremely short shutter speeds to avoid fuzzy images, therefore increasing demands on illumination.

2.3 ISO number

In very basic terms, ISO represents a level of sensitivity to light. The lower the ISO number, the less sensitive the sensor is. ISO number needs to be set as low as possible for DIC analysis since low ISO numbers produce the smallest amount of noise that makes images appear grainy. From a technical point of view, noise in images represents a visual manifestation of a low signal-to-noise ratio, which can be defined as the ratio of the power of a signal (meaningful information) and power of background noise. All modern cameras equipped with CCD/CMOS sensors have their base ISO number equal to 100. The impact of the ISO number on the quality of images is presented in Figure 2.2.



Figure 2.2: Comparison of a sharp image taken with setting of ISO number to 100 (left) and an image with noise due to setting ISO to 1600 (right).

Cameras with smaller sensors, such as cell phones or compact cameras having thumbnail-sized sensors can reach unacceptable noise levels even at ISO 400.

2.4 Lenses

The design and quality of optical lenses play a crucial role in providing high-quality undistorted images. Optical aberration usually associated with the use of low-quality lenses results in non-uniform geometric distortions of images and introduces additional errors in the measurement [100]. Especially short objective lenses are not suitable for DIC because of large distortions at the edges of acquired images [101–103]. The most frequent are barrel, pincushion, and mustache distortions (Figure 2.3) [102, 104–106]. To tackle these issues, several camera calibration techniques using regular chessboard or circle dot target [107–109] have been developed in the field of computer vision and used in DIC measurements [41]. A simple, easy-to-implement lens distortion correction method tailored for 2D-DIC was later introduced by Pan et al. [110].

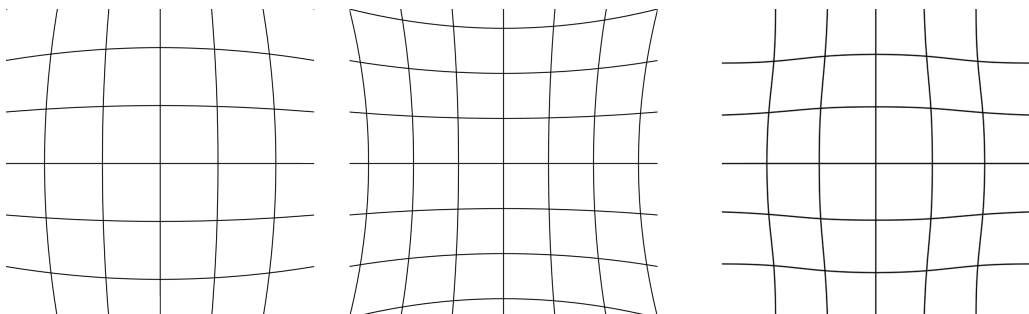


Figure 2.3: Schematic examples of a photographed grid distorted due to barrel, pincushion, and mustache distortions (from left to right).

Despite the availability of correction algorithms, it is of major importance to use high-quality lenses, suitable for DIC measurements. Telephoto lenses are most suitable; these lenses have the outermost element of a short focal length and the second set of elements close to a sensor in order to extend the cone of light so that it appears to have come from a lens of much greater focal length. This behavior, in turn, eliminates to a great extent the effects of perspective and fish eye. Generally, a perfectly orthographic view can be achieved using telecentric lenses [111], but even in the orthographic view out-of-plane deformations caused by rotations of an observed object cause errors in 2D-DIC and should be avoided [45, 112]. Moreover, to reach very precise measurement, the experimentalist has to keep in mind that even in case of extremely expensive high-quality telecentric lenses image distortions may exist due to aberrations and misalignment of optical elements [110].

2.5 Image compression and file formats

A camera raw image file contains unprocessed data from a sensor. Cameras transform exposure of CCD/CMOS sensor pixels, recorded in an analog form of voltage level, to a digital signal [113]. Commonly available sensors can handle grayscale (monochrome), red-green-blue (RGB), or cyan-magenta-yellow-black (CMYK) color channels for each pixel. The intensities for each channel are usually stored in 8 bits of memory per pixel, yielding $2^8 = 256$ color resolution. In the case of grayscale, even 12 bits per pixel are common. Besides pixel intensities, cameras also store metadata containing information about the matrix size, color depth, bit depth, camera settings, byte-ordering, and image thumbnails in so-called RAW files [114].

Even though RAW format can be handled by modern computer programs, it is in most cases inconvenient format to work with and RAW data are usually encoded. The encoding of data bits is standardized to attain a certain structure. There are several formats that identify themselves as an image when loaded. While infinitely scalable vector images defined mathematically as geometric primitives are suitable for drawings or letters, photography images attain a form of a rectangular grid of pixels, i.e., are stored in a form of a raster (bitmap). Examples of raster image formats are BMP, JPEG, TIFF, and PNG.

To save computer memory, most formats allow compression to be applied to the image data [115] based on eliminating redundancies in the image data. Mathematical redundancy elimination is referred to as lossless compression, based on a search for repeating patterns that are encoded using various mathematical formulas [116]. In such a case, decompression yields identical images to the original source and achieve up to 50% memory savings. The lossless compression is most efficient in the case of simple images such as line art and flat colors [117]. On the other hand, lossy compression discards data considered nonessential to human perception, such as very bright or dark tones [118]. Lossy compression algorithms are therefore not irreversible and reduce the image detail quality, but the compression rates are usually higher compared to lossless compression, reaching about 90% memory savings.

Uncompressed BMP file format was first introduced by Microsoft and despite its simple encoding and lack of many features, it is still considered as the most basic standard for interchanging images between software environments. JPEG (joint photographic experts group) format developed in the 1980s represents a standard for lossy image compression in a frequency

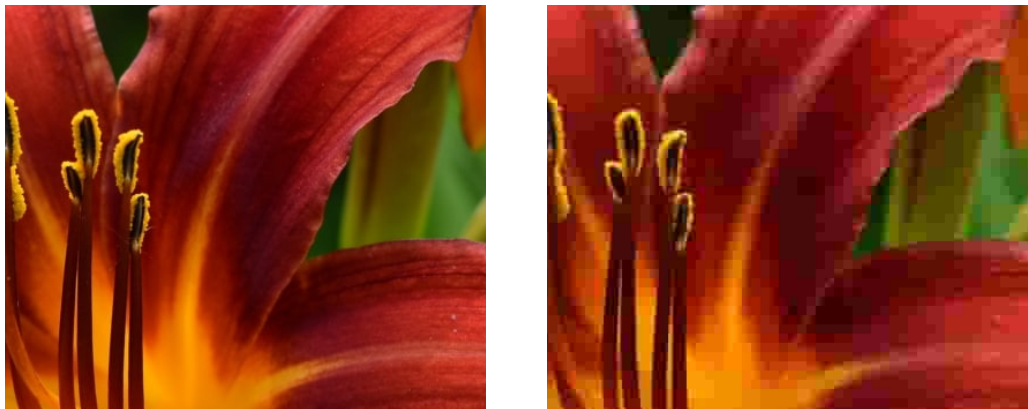


Figure 2.4: Illustration of lossy compression; uncompressed image (left) and the same image compressed to 10% of its original size (right).

domain. The compression losses result in introducing errors in DIC and therefore high compression is not recommended for DIC analysis. Unlike JPEG, TIFF (tagged image file format) and PNG (portable network graphics) formats allow employing lossless compression. TIFF format allows, in addition, inclusion of capabilities in a form of tags. Unlike BMP, JPEG, or TIFF capable of handling RGB channels, PNG format also includes a fourth channel that defines transparency.

Chapter 3

Image registration

In general terms, registration of images involves techniques for finding geometrical transformations that enable aligning two or more images taken at different times, from a different location, and/or using different sensors. These techniques are utilized in various areas, such as remote sensing (including multispectral classification, environmental monitoring, change detection, or integrating information into geographic information systems) [119–121], in medicine [122–125] to obtain complete information from various diagnostics procedures, in cartography for map updating [126], and in computer vision for target localization [127–129] or automatic quality control [130].

The methods can be divided into three major groups: algorithms that work with values of intensity in the spatial domain [131], those that utilize Fourier transform [132–135], and algorithms that exploit feature detection [136–138]. A comprehensive survey of image registration techniques was first carried out Ghaffary and Sawchuk [139], followed by Brown [140], or later by Zitová and Flusser [141].

The utilization of Fast Fourier transform algorithms proved to be computationally efficient [134] and elegant solution for fast registration of images corrupted with optical noise or changes in illumination [142, 143]. These algorithms exploit a Fourier representation of images in a frequency domain for locating correlation peak, as introduced next.

3.1 Fourier transform

The Fourier transform $F(\alpha)$ decomposes a signal, being a function of time $f(t)$, into the frequencies α the signal consists of. Hence, the Fourier transform is called the frequency domain representation of a signal expressed in the time domain. $F(\alpha)$ of $f(t)$ is a complex-valued function of frequency, whose absolute value represents the amount of that frequency present in the original function, and whose complex argument is the phase offset in that frequency [144]. Mathematically, the Fourier transform can be written as

$$\mathcal{F}\{f(t)\} = F(\alpha) = \int_{-\infty}^{\infty} f(t) e^{-2\pi i \alpha t} dt, \quad (3.1)$$

where α is a frequency, $-2\pi\alpha$ is the angular frequency, t represents time, and $i = \sqrt{-1}$.

In practice the continuous signal $f(t)$ is measured as a sequence $f(x)$ containing N consecutive samples, and the function of frequency attains the form of an array called discrete Fourier transform (DFT) defined as [145]:

$$\mathcal{D}\{f(x)\} = F(\xi) = \sum_{x=1}^{N-1} f(x) e^{-2\pi i \frac{x\xi}{N}}. \quad (3.2)$$

To compute a transformation of the original (time or spatial) domain into a frequency domain, fast Fourier transform algorithms (FFT) based on factorizing the DFT matrix into a product of sparse matrices are used [146, 147]. Such an approach allows reducing the complexity of computing the DFT from $O(N^2)$ to $O(N \log(N))$. The number of frequencies in $F(\xi)$ always equals the number of samples in the time/spatial domain.

For simplicity, the DFT extension into two dimensions is illustrated considering a square matrix $N \times N$ representing an image. The expression (3.1) becomes [148]

$$\mathcal{D}\{f(x, y)\} = F(\xi, \eta) = \sum_{x=1}^{N-1} \sum_{y=1}^{N-1} f(x, y) e^{-2\pi i \left(\frac{x\xi}{N} + \frac{y\eta}{N} \right)}, \quad (3.3)$$

where $f(x, y)$ is the image represented by the matrix of pixel intensities, while $F(\xi, \eta)$ having the same size as $f(x, y)$ represents the image in the frequency domain. The inverse transform is calculated as

$$\mathcal{D}^{-1}\{F(\xi, \eta)\} = f(x, y) = \frac{1}{N^2} \sum_{\xi=1}^{N-1} \sum_{\eta=1}^{N-1} F(\xi, \eta) e^{2\pi i \left(\frac{x\xi}{N} + \frac{y\eta}{N} \right)}, \quad (3.4)$$

where $\frac{1}{N^2}$ is the normalization term in the inverse transformation.

Analogically to one-dimensional arrays, DFT decomposes an image into its sine and cosine components [149, 150]. It is an essential operation in the field of image processing, especially in filtering, image reconstruction, or image compression [151]. Moreover, Fourier transform can be exploited for image registration as translation, rotation, reflection, and scale have their counterpart in the frequency domain. Each component (pixel) in $F(\xi, \eta)$ represents a particular frequency contained in the spatial domain image, see Figure 3.1. DFT produces a complex number valued output which can be displayed with two images, either with the real and imaginary part or with magnitude and phase.

To obtain the results from Eq. (3.4) in two dimensions, a double sum has to be calculated for each image pixel. Because the Fourier transform is separable, the expression can be written as

$$F(\xi, \eta) = \frac{1}{N} \sum_{y=1}^{N-1} P(\xi, y) e^{-2\pi i \frac{y\eta}{N}}, \quad (3.5)$$

where

$$P(\xi, y) = \frac{1}{N} \sum_{x=1}^{N-1} f(x, y) e^{-2\pi i \frac{\xi x}{N}}, \quad (3.6)$$

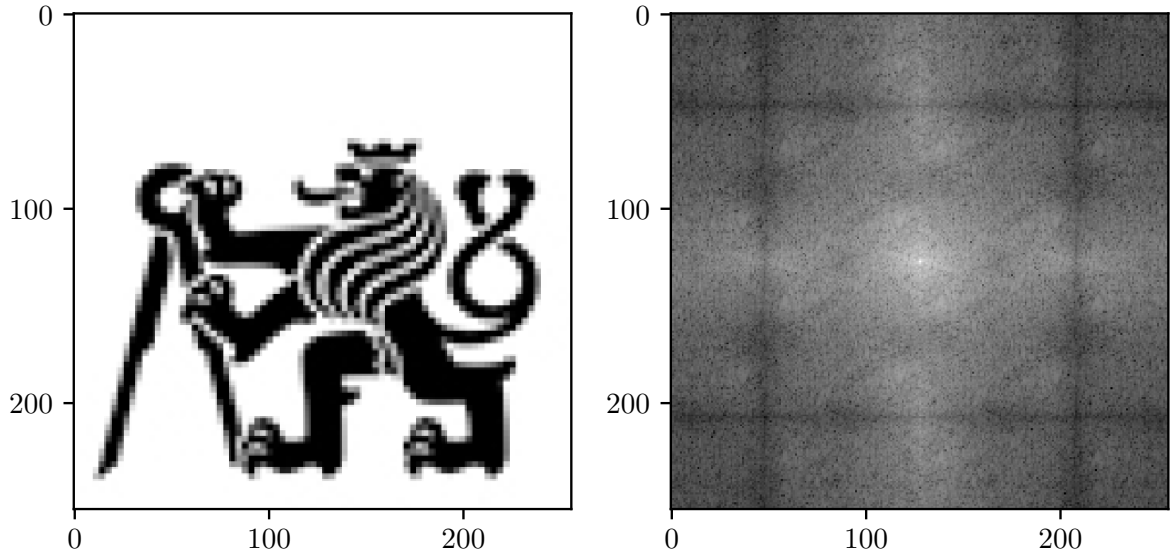


Figure 3.1: Gray scale image (left) transformed to a frequency domain displayed in a logarithmic scale (right).

Expressing the two-dimensional Fourier transform in the form of $2N$ one-dimensional transforms decreases the number of required computations and allows to use DFT matrix multiplication⁴ for each dimension separately.

3.2 Phase correlation

The mathematical principles of the phase correlation alignment method for measuring translation, rotation, and scaling are thoroughly described in numerous handbooks and papers, e.g., [140, 141, 152, 153]. The approach proposed by Kuglin and Hines [132] can be exploited for registering images that have been shifted relative to each other as described next.

The Fourier transform $F(\xi, \eta)$ can be decomposed into its real $R(\xi, \eta)$ and imaginary part $I(\xi, \eta)$:

$$F(\xi, \eta) = R(\xi, \eta) + iI(\xi, \eta), \quad (3.7)$$

which can be also expressed using the exponential form as

$$F(\xi, \eta) = |F(\xi, \eta)| e^{i\phi(\xi, \eta)}, \quad (3.8)$$

where $|F(\xi, \eta)|$ is the magnitude of the Fourier transform and $\phi(\xi, \eta)$ is the phase angle [140].

Let $f_1(x, y)$ and $f_2(x, y)$ be two images which are related through $f_2(x, y) = f_1(x - x_0, y - y_0)$, as indicated in Figure 3.2, and there are no periodic structures in these images. Their corresponding Fourier transforms $F_1(\xi, \eta)$ and $F_2(\xi, \eta)$ will be related by

$$F_2(\xi, \eta) = F_1(\xi, \eta) e^{-2\pi i(\xi x_0 + \eta y_0)}. \quad (3.9)$$

⁴https://en.wikipedia.org/wiki/DFT_matrix

The normalized cross-power spectrum of the two images $f_1(x, y)$ and $f_2(x, y)$ with their Fourier transforms $F_1(\xi, \eta)$ and $F_2(\xi, \eta)$ is defined as

$$Z_{f_1, f_2}(\xi, \eta) = \frac{F_1(\xi, \eta) F_2^*(\xi, \eta)}{|F_1(\xi, \eta) F_2(\xi, \eta)|} = e^{2\pi i(\xi x_0 + \eta y_0)} \quad (3.10)$$

where $F^*(\xi, \eta)$ is the complex conjugate of $F(\xi, \eta)$.

As the correlation theorem [140] states, the Fourier transform of the correlation of two images is the product of the Fourier transform of one image and the complex conjugate of the Fourier transform of the other. Therefore, as the shift theorem [132] guarantees, the cross-power spectrum is equivalent to the phase difference between the images. However, the cross-correlation must be normalized since intensity changes (non-uniform illumination in time) would influence the measure. The inverse Fourier transform of the cross-power spectrum yields a discrete impulse function

$$\delta_{f_1, f_2}(x, y) = \mathcal{D}^{-1}\{Z_{f_1, f_2}(\xi, \eta)\}, \quad (3.11)$$

which is approximately zero everywhere except at the coordinates corresponding to the shift $(-x_0, -y_0)$:

$$\delta(x, y) = \begin{cases} 1 & \text{if } (x, y) = (-x_0, -y_0) \\ 0 & \text{otherwise} \end{cases}. \quad (3.12)$$

For illustration see Figure 3.3. In practice, there is never such a sharp peak in $\delta(x, y)$ because of optical noise, mutual rotation of images, and displacements different from whole pixels.

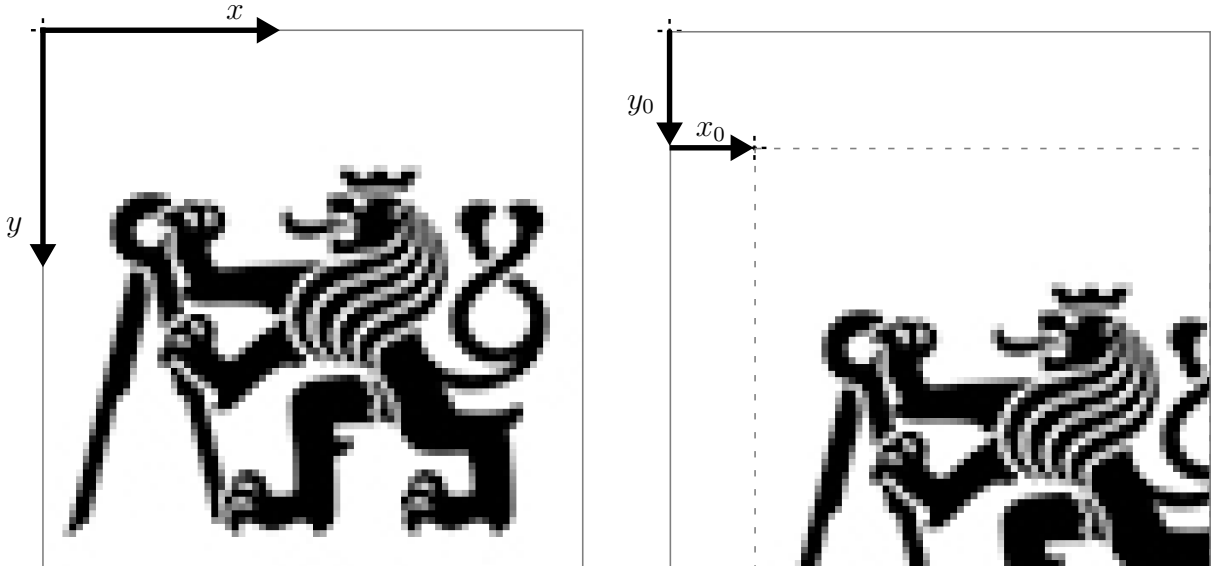


Figure 3.2: Example of two images shifted in Inscape [154] by $x_0 = 15.5\%$ and $y_0 = 21.5\%$, corresponding to 39.7 and 54.9 px, respectively.

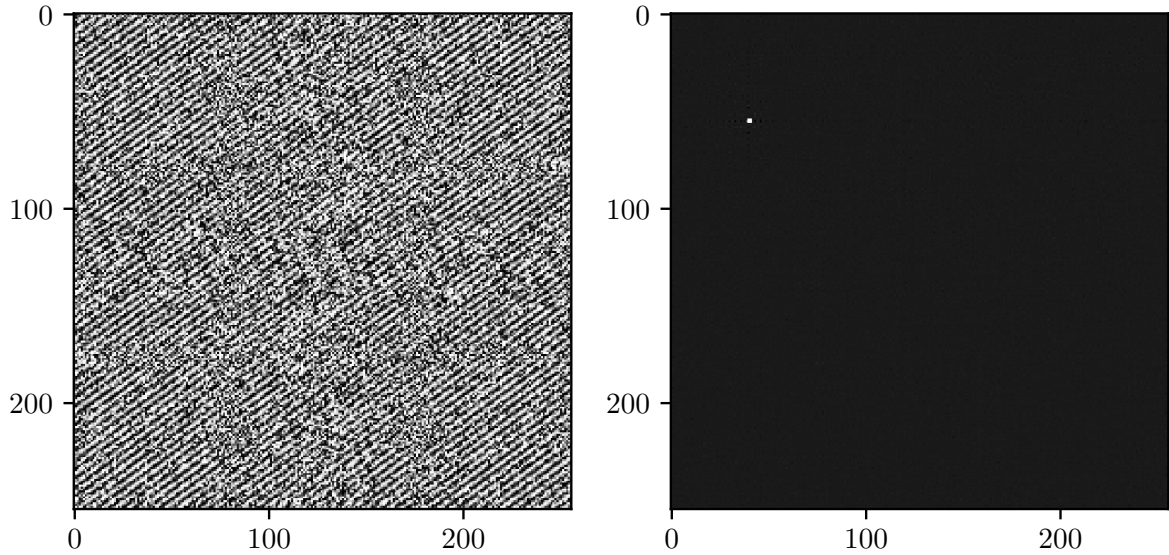


Figure 3.3: Cross-power spectrum of the two shifted images from Figure 3.2 (left) and a corresponding discrete impulse function (right) with a white pixel illustrating the maximum at $x = 40$ px and $y = 55$ px.

3.3 Subpixel registration

Although the method based on cross-correlation of images in the frequency domain is fast and robust, there are two considerable limitations: first, it handles only translations along Cartesian axes of the image, second, no sub-pixel precision can be reached because the peak is found in a matrix of the same size as the registered image. The first limitation was tackled by several authors who obtained angle and scaling factors through a slightly modified FFT procedure [152, 155]. As the measurement of displacements involves registering relatively small pixel subsets, the bigger demands on computational power would outweigh slight accuracy improvements by considering rotation and scaling. On the other hand, reaching subpixel accuracy is crucial.

There are several alternatives how to reach a subpixel accuracy of the image registration: (i) fitting a parabolic function around the correlation peak [156], (ii) computing the ratio between pixel values near the correlation peak [157], or (iii) upsampling the correlation peak in the Fourier space [158, 159]. The first approach (i) appears to be a bad solution since it was demonstrated that the peak fitting methods yield systematic errors [160, 161], while the second approach (ii) lacks robustness [159]. The algorithms based on (iii) that involve upsampling the Fourier transform around the correlation peak appear to be the most robust and resistant to noise, yet accurate and computationally efficient [158, 161].

The upsampling in the Fourier transform is a commonly used technique when enhancing the resolution of an image. This is accomplished by embedding the image in the Fourier domain in a larger matrix of zeros (a technique also known as zero padding), see Figure 3.4. The matrix size is dictated by the required size of input/output images or, in the case of image registration, the size of correlated images (pixel subsets) N and required subpixel accuracy κ . The size of

zero-padding band α can be calculated as

$$\alpha = \frac{N(\kappa - 1)}{2}. \quad (3.13)$$

Such addition of zero frequencies does not have any impact on the distribution of features within the image in the spatial domain since the non-zero frequencies and amplitudes are preserved and only the number of samples increases, see Figure 3.5. By applying the same technique on the cross-power spectrum from Figure 3.3, a refinement around of correlation peak can be achieved as demonstrated in Figure 3.6.

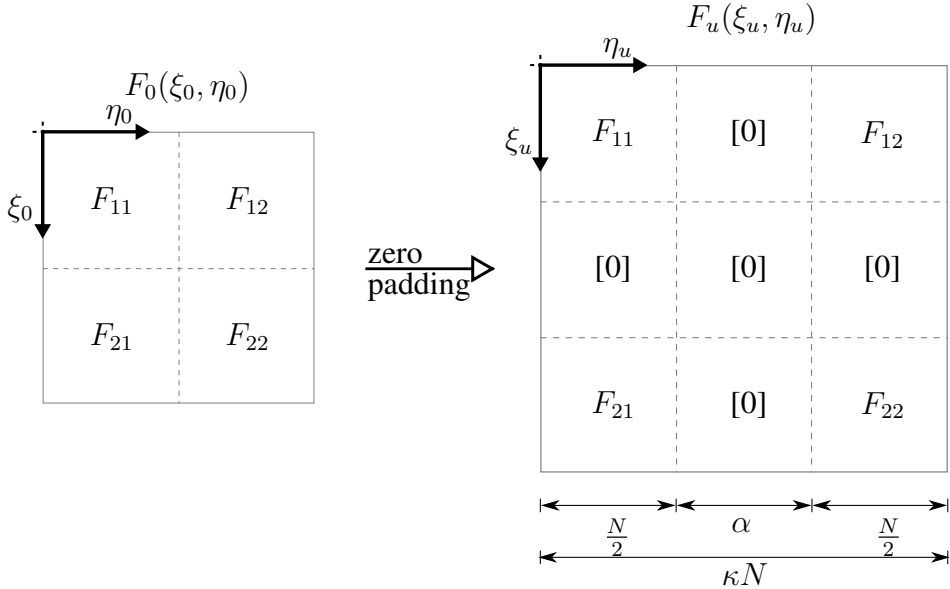


Figure 3.4: Illustration of zero-padding for reaching subpixel accuracy of the cross-correlation procedure.

The upsampling of $Z_{f_1, f_2}(\xi, \eta)$ by zero-padding of the product $F_1(\xi, \eta) F_2^*(\xi, \eta)$ and using the inverse DFT would be a straightforward approach to compute x_0 and y_0 with a subpixel accuracy. However, this procedure is computationally very inefficient since registering an image with the size of $N \times N$ and the required accuracy κ requires the computation of $\kappa N \times \kappa N$ Fourier transforms. The developed software introduced in Chapter 6 employs the algorithm proposed by Guizar-Sicairos et al. [158]. Using their approach, the upsampling is carried efficiently. It obtains an initial estimate of the cross-correlation peak by the FFT-based procedure described in Section 3.2 with the setting of $\kappa = 2$. Once the location of the cross-correlation peak is computed to within half a pixel, a matrix multiplication implementation of the DFT is used to refine the estimate of x_0 and y_0 by calculating the fully upsampled product $F_1(\xi, \eta) F_2^*(\xi, \eta)$ in a 1.5×1.5 region around the initial estimate [162]. Their approach was classified as one of the most reliable algorithms to register images using a phase correlation method [163, 164].

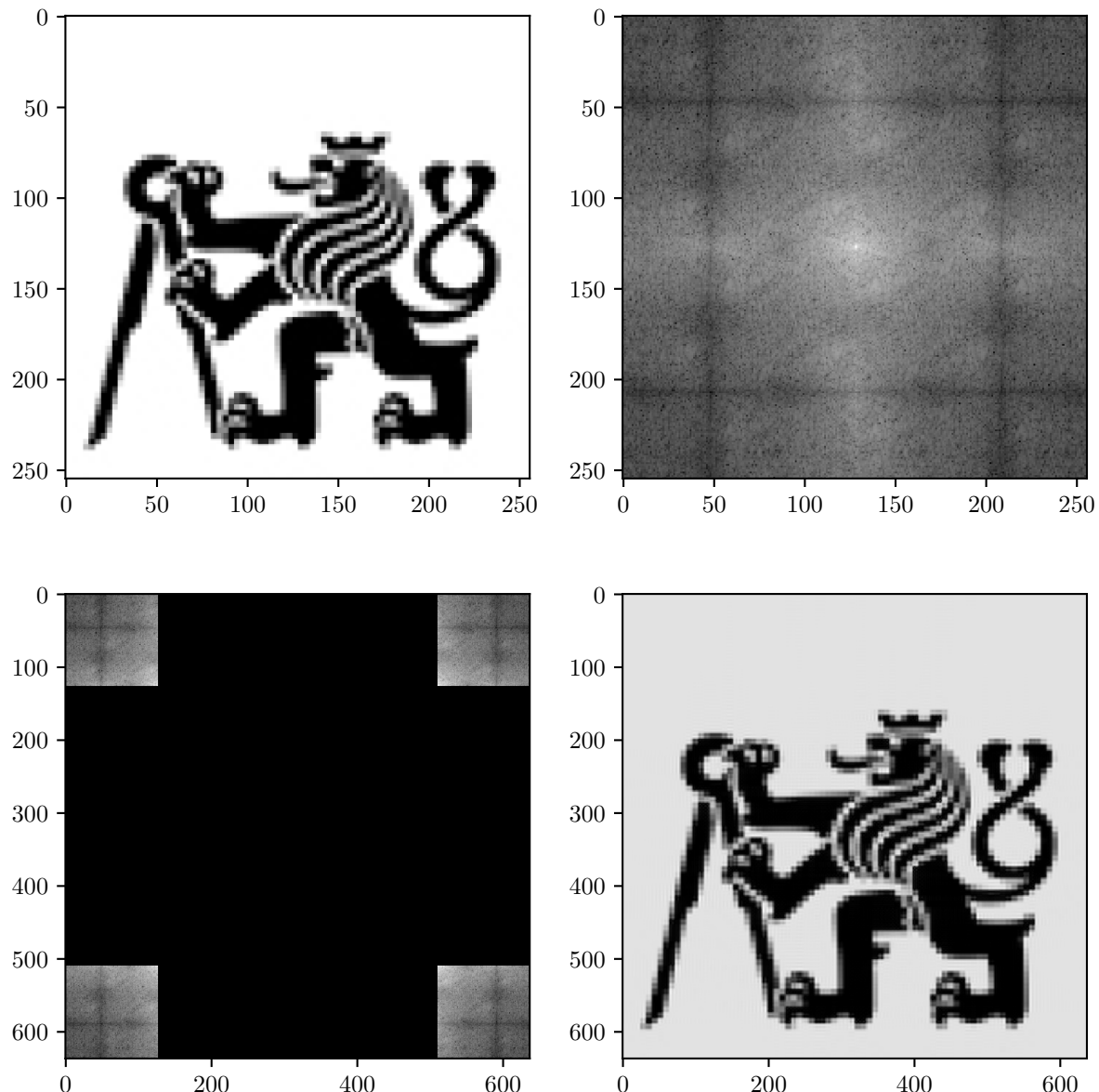


Figure 3.5: Image upscaling through upsampling in the frequency domain: original image (top left), cross-correlation spectrum (top right), zero-padded spectrum (bottom left), and the inverse of the upsampled spectrum yielding an upsampled original image (bottom right).

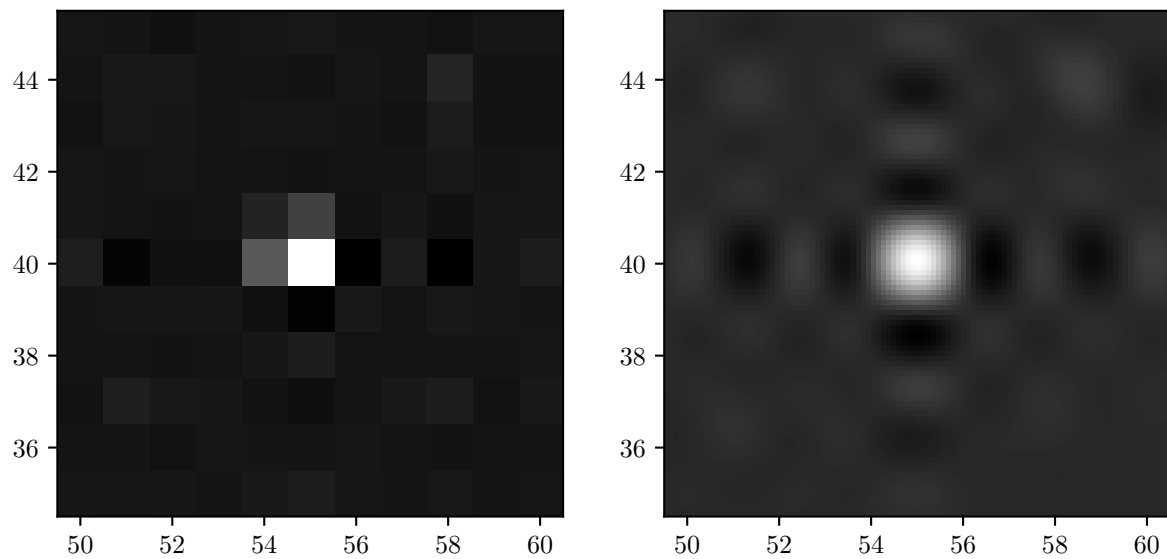


Figure 3.6: A peak in discrete impulse function $\delta(x, y)$ before (left) and after cross-power upscaling to reach a subpixel fraction accuracy κ ; the peaks are located at $x = 40$ px and $y = 55$ px, and $x = 39.7$ px and $y = 54.9$ px, respectively. The shift calculation was applied to the images from Figure 3.2.

Chapter 4

Assessment of stochastic patterns for DIC

Based on: J. Antoš, V. Nežerka, and M. Somr, Assessment of 2D-DIC stochastic patterns, *Acta Polytechnica CTU Proceedings* 13 (2017) 1–10, doi: [10.14311/APP.2017.13.0001](https://doi.org/10.14311/APP.2017.13.0001)

In order to facilitate correlation and obtain subset displacements/deformations by identifying areas of matching grey-scale values between the speckle pattern in each subset of deformed and undeformed (reference) images. To facilitate the correlation, a stochastic speckle pattern must be applied (if not present naturally) to a specimen surface in order to provide a random grey-level variations at the sufficient quality of which is fundamental to the precision of the measured displacement data. It is well established that the trade-off between the data resolution and precision is affected by the quality of a pattern. Resolution of displacement fields is maximized by reducing the size of the subsets, but as the subset size decreases, the uncertainty in the strain measurement increases due to a reduction in the number of features to track within each subset [64]. Therefore, the resolution and accuracy of the displacement and deformation fields are limited by the total number of pixels within an image.

The accuracy of DIC is an issue frequently discussed by both, theoreticians and experimentalists [85, 165]. Besides the choice of suitable DIC algorithms, other factors substantially influence the measurement accuracy. The errors may be classified into two categories: (i) systematic experimental errors such as bad calibration and setting of image acquisition system and (ii) errors produced by correlation algorithms. A majority of research into the accuracy of DIC is focused on correlation algorithms and processing parameters [166], shape function selection [167], or methods of obtaining subpixel accuracy [168]. Less attention has been paid to the effect of the quality of the speckle pattern. It is important for the artificial pattern or natural texture to be adjusted in accordance with the expected displacement field in order to maximize measurement accuracy, as speckles can be both too large and too small for the particular measurement [169]. Quantitative error analysis [170–173] shows that the measurement error depends crucially on the presence of large intensity gradients within the pattern. Therefore, the technique in most cases requires a specimen preparation procedure to enhance the surface texture, since the natural one does not provide a required quality in terms of intensity gradients and speckle-size distribution.

Pattern assessment has been discussed by a few authors [41, 174, 175], offering a number of methods to evaluate the quality of applied patterns. Pan et al. [86] presented a number of assessment criteria based upon the local subset intensity gradients [85] and the global mean intensity gradient (MIG) throughout the image. The latter criteria showed a good agreement to results obtained numerically. The benefit of applying the global criteria is that these are straightforward. High MIG values typically result in smaller bias and less dispersion in DIC measurements. On the other hand, Crammonde et al. [176] objected that global parameters, such as MIG, are not sufficient to evaluate strain accuracy. Based on their findings, simple means of a randomness assessment is to employ the outcomes of the Shannon entropy theory [177].

In this chapter, various patterns produced by the spraying white/black dots on a contrast background were investigated. In addition, natural textures of various materials were studied as well, to demonstrate their performance. The knowledge of a texture suitability is essential when monitoring existing structures where application of artificial patterns is not possible. To eliminate the impact caused by image acquisition system (such as the distortion of the camera lens, lighting variation, etc.) during the experiment, numerical approach was utilized to investigate the relationship between Shannon entropy, mean intensity gradient, values of correlation coefficient, and error in DIC measurements. The explanation of the mentioned parameters is provided next.

4.1 Assessment criteria

4.1.1 Normalized cross-correlation

Correlation between two signals [131] (also referred to as cross-correlation) is a standard approach to feature detection and image registration [178–180]). The normalized form of correlation takes into account intensities relative to the highest one, thus eliminating the sensitivity to changes in illumination intensity. However, it does not have a correspondingly simple and efficient frequency domain expression. For this reason, normalized cross-correlation must be computed in a spatial domain and fast spatial domain matching methods had to be developed.

4.1.2 Mean intensity gradient

Mean intensity gradient (MIG) was proposed by Pan et al. [86] as a suitable global parameter for evaluating the quality of a speckle pattern over the entire domain. Both a mean bias error and standard deviation of measured displacements are influenced by the MIG of a speckle pattern. The speckle pattern with a large MIG is supposed to produce small displacement measurement errors. MIG is defined as

$$\delta_f = \sum_{i=1}^W \sum_{j=1}^H |\nabla f(x_{ij})| \frac{1}{W \times H}, \quad (4.1)$$

where W and H are the image width and height in pixels, $|\nabla f(x_{ij})| = \sqrt{f_i(x_{ij})^2 + f_j(x_{ij})^2}$ is the modulus of the local intensity gradient. $f_i(x_{ij})$ and $f_j(x_{ij})$ are the i - and j -directional in-

tensity derivatives at pixel (x_{ij}) respectively, which can be computed using a central difference algorithm.

4.1.3 Shannon entropy

A high Shannon entropy value indicates a high level of texturing, or broadness in the greyscale distribution of the image, beneficial for maximizing the correlation function peak when a correct match has been found. The Shannon entropy parameter is defined as [181]

$$\Psi = \sum_{i=1}^W \sum_{j=1}^H f(x_{ij}) \log(f(x_{ij})). \quad (4.2)$$

4.2 Assessment of patterns and textures

Randomly distributed speckles must not exhibit any preferential directions. High contrasts are required to provide sharp peaks in the correlation function. To test this requirement, initial synthetic tests on samples of 400×400 px were performed on six model patterns (Figure 4.1). The patterns/textures were tested with respect to four quality indicators: value of cross-correlation coefficient for two different subset sizes (10×10 px and 30×30 px), Shannon entropy, and MIG. The summary of the investigated patterns and textures is provided in Table 4.1.

Based on the values of normalized cross-correlation functions presented in the form of surface plots in Figures 4.2 and 4.3, it can be concluded that the correlation function peaks can be highlighted by setting bigger subset size since these contain more distinct features. Especially in the case of small subset size, 10×10 px, the correlation peaks on coarse textures could not be clearly identified. This could lead to huge errors of DIC measurements in the case of significantly distorted images. However, the findings cannot be generalized, since in some patterns the cross-correlation correlation function does not exhibit any distinct peak in for small subsets, while correlation of the larger one results in unique match and low value of mean correlation coefficient (cf. Figures 4.2(b,f), 4.3(b,f), and Table 4.1). Therefore, the pattern assessment based on the the mean value of the cross-correlation function must be carried out for any subset size independently. Moreover, a statistical information about number of peaks in the form of a decay in the power law distribution would provide more accurate description.

Based on observation of distribution of correlation coefficient a power law distribution can be assumed (Figures 4.4 and 4.5). The power law function is defined by equation $y_p = x_p^{-\alpha}$, where α is the decay parameter which provides information about the distribution of correlation coefficient over the investigated domain. Larger α indicates smaller amount of unwanted correlation peaks which is desirable.

It is also clear that neither Shannon entropy nor MIG are capable of providing clear indication of the pattern quality since these two are not in agreement—once the pattern is, relative to other ones, regarded as superior to others based on Shannon entropy, MIG provides completely different results, see Table 4.1. Therefore, new more universal criteria taking into account size, contrast, and size-distribution of speckles should be proposed.

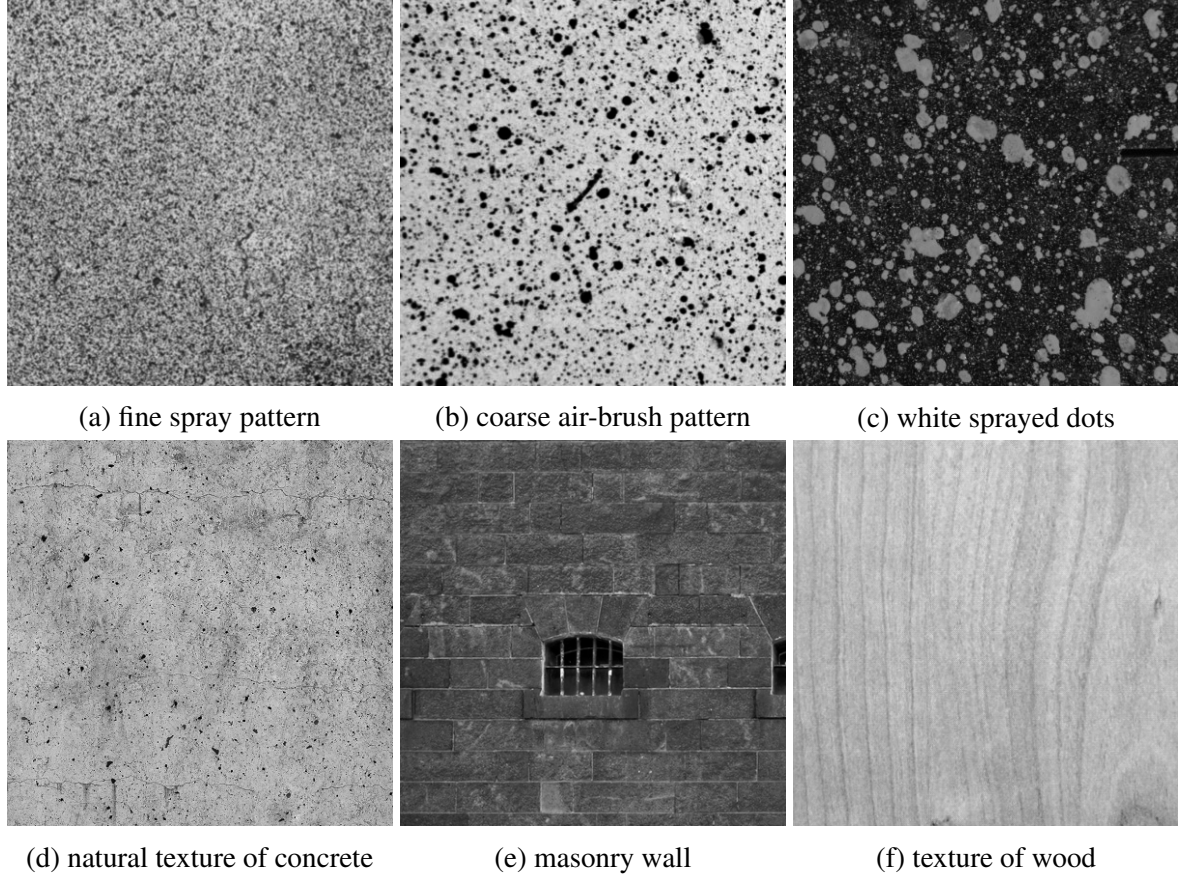


Figure 4.1: Investigated artificial patterns (top) and natural textures (bottom).

Table 4.1: Mean correlation coefficient, $\overline{\gamma(x_{ij})}$, power law distribution decay parameter α , Ψ , and δ_f for tested patterns/textures and different size of subsets.

Sample	$\overline{\gamma(x_{ij})}$		α		Ψ	δ_f
	10×10	30×30	10×10	30×30		
Fine spray pattern (a)	0.152	0.054	0.847	0.959	5.524	121.182
Coarse air-brush pattern (b)	0.190	0.107	1.009	1.046	5.413	127.614
White spray dots (c)	0.089	0.138	1.148	0.997	4.972	82.198
Natural texture of concrete (d)	0.090	0.039	1.027	0.975	6.292	75.849
Masonry wall (e)	0.200	0.187	0.879	0.939	4.250	50.914
Texture of wood (f)	0.208	0.097	0.878	0.981	5.012	29.027

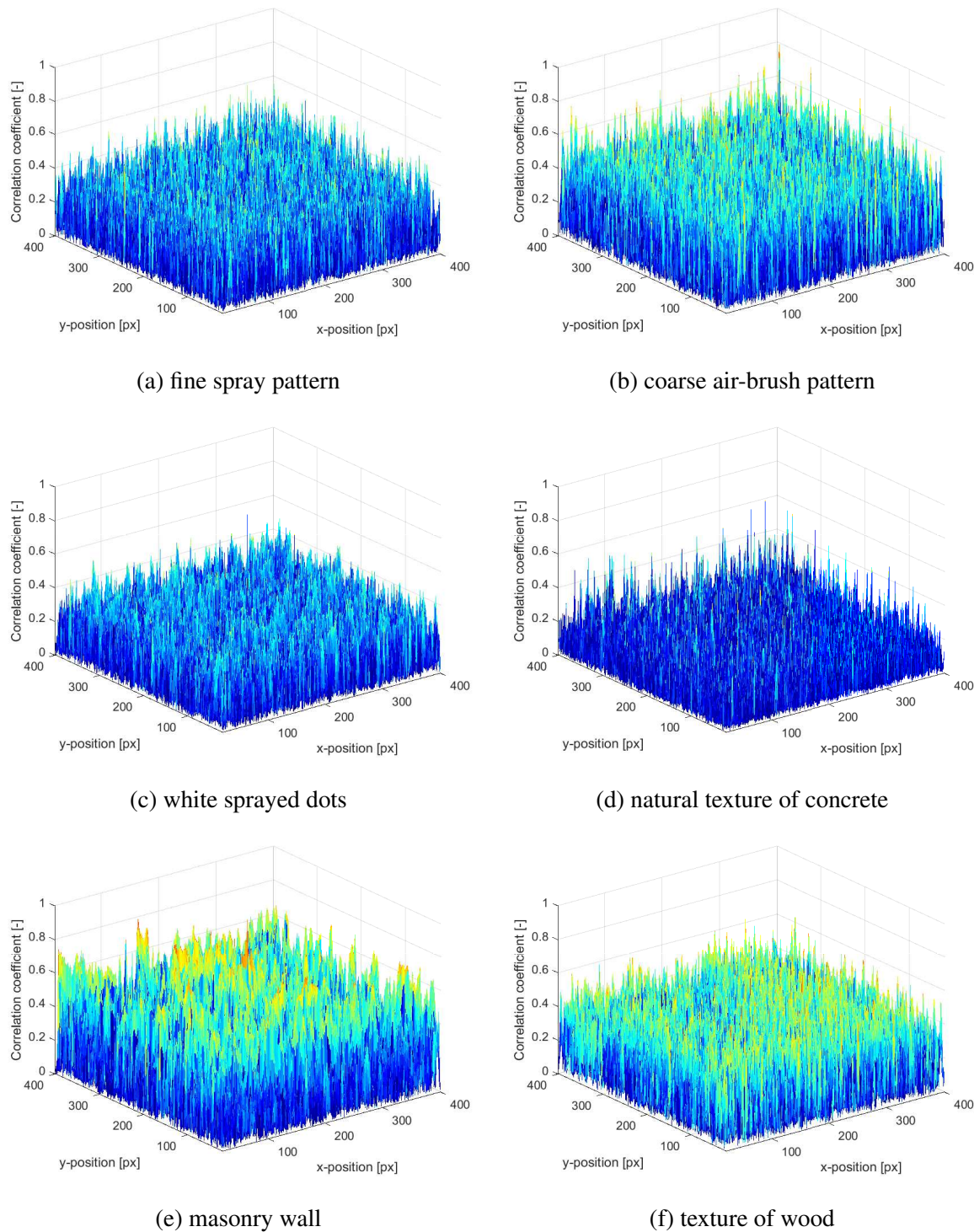


Figure 4.2: Correlation function values for 10×10 px subset size.

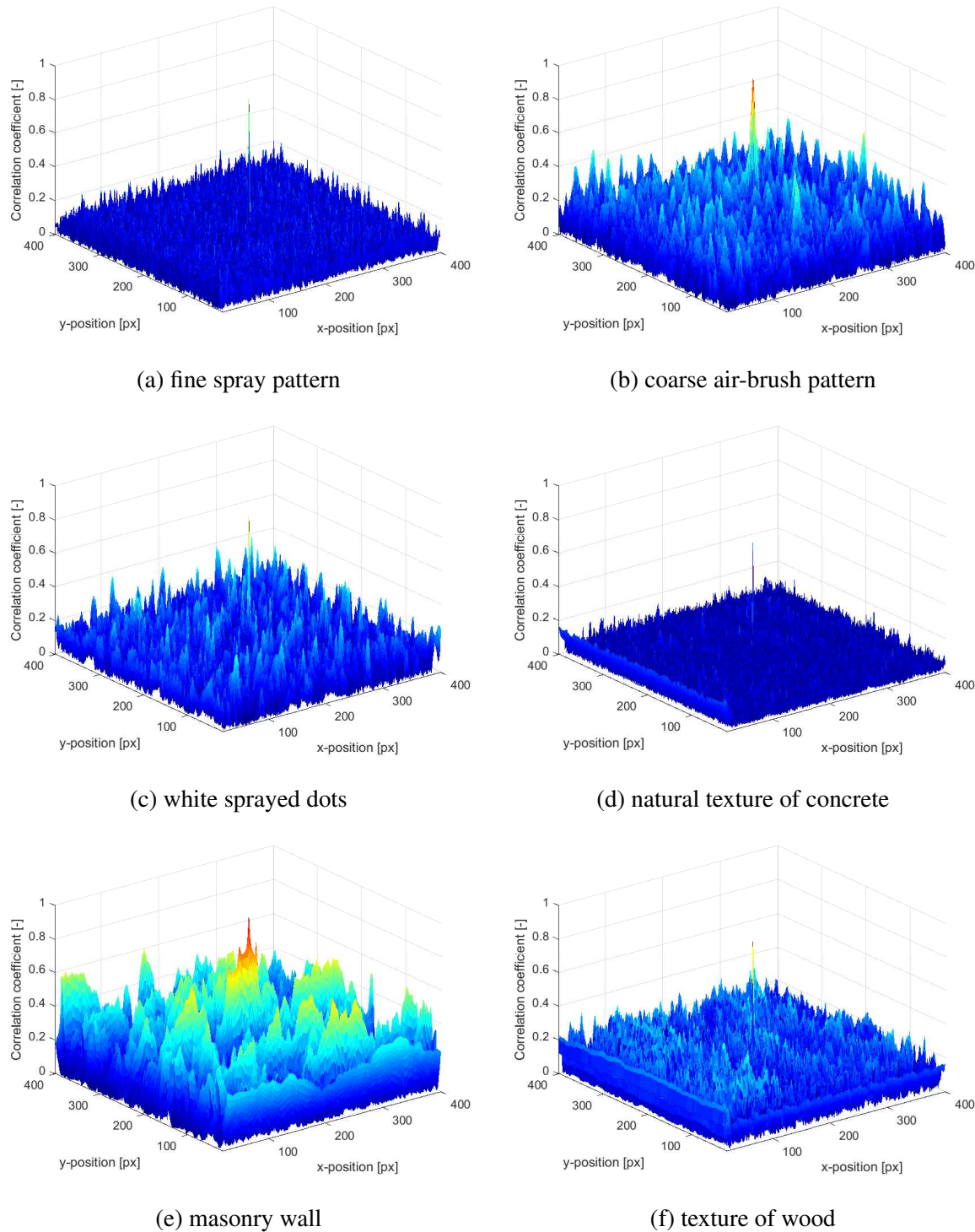


Figure 4.3: Correlation function values for 30×30 px subset size.

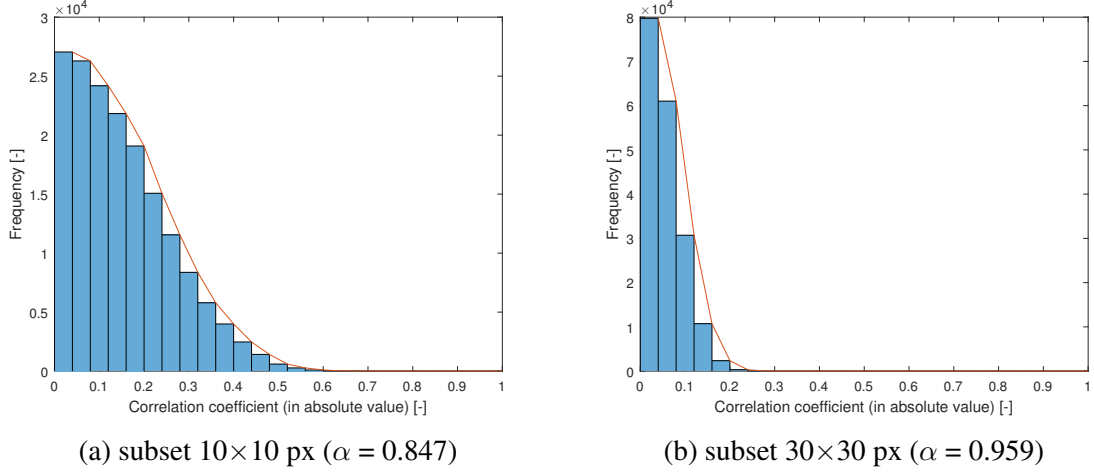


Figure 4.4: Distribution of correlation coefficient, fine spray pattern.

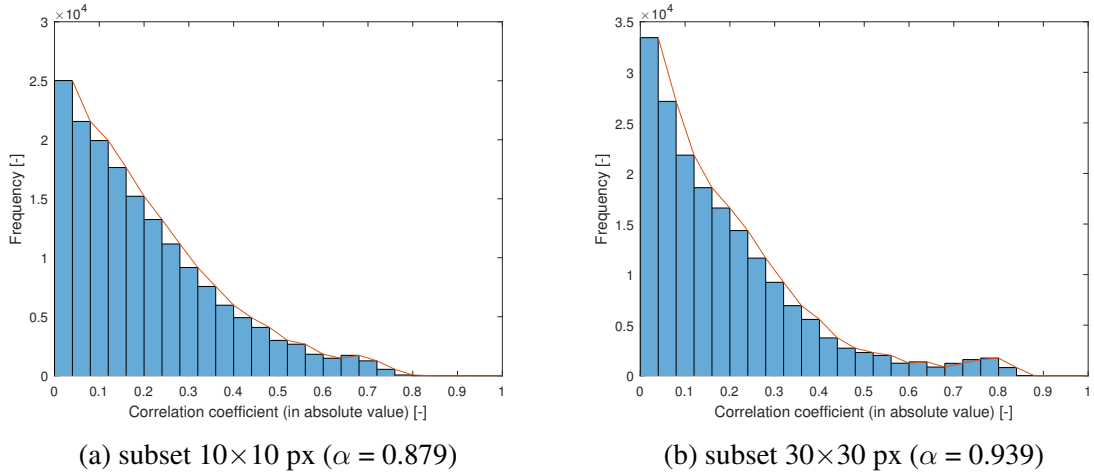


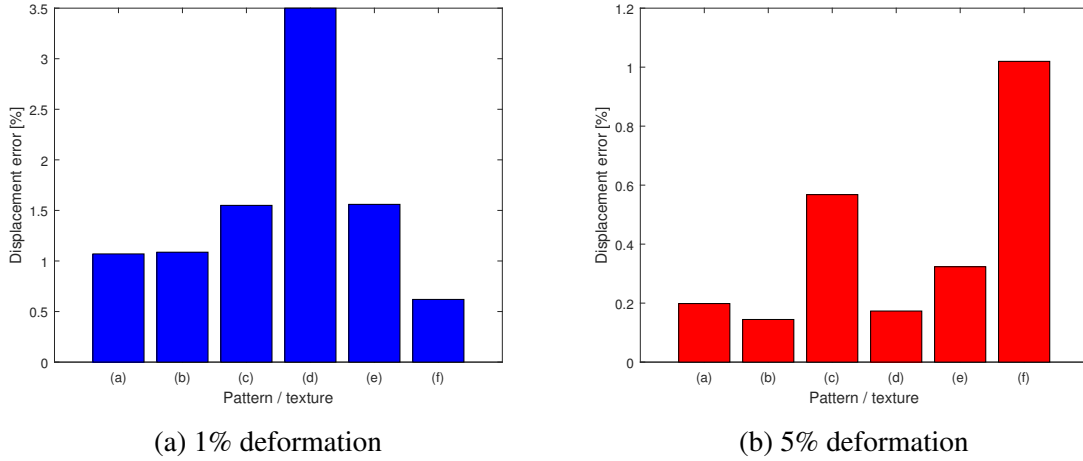
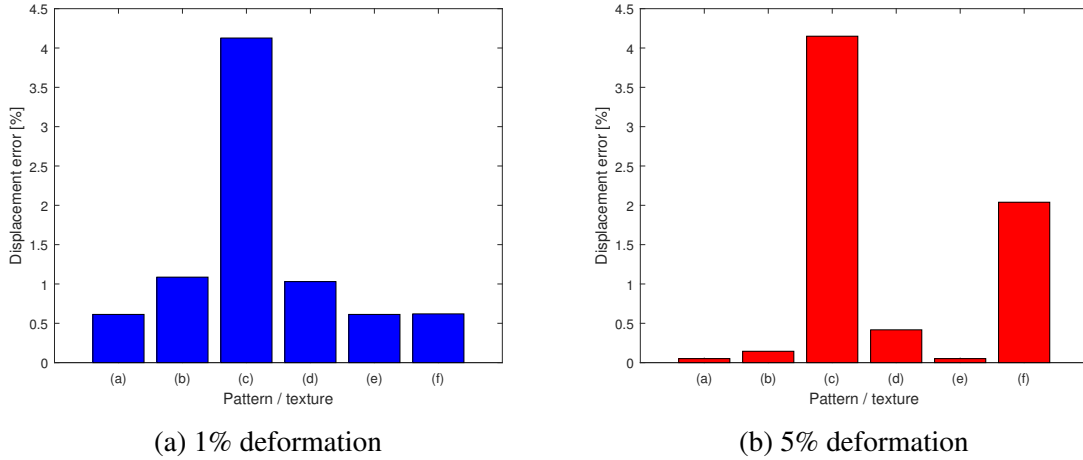
Figure 4.5: Distribution of correlation coefficient, masonry wall.

4.3 Virtual Stretching of Patterns and Textures

The artificial patterns and natural textures were tested in the proof-of-concept experiments carried out virtually on a computer by prescribing a constant deformation. Special attention was paid to the ability of the pattern to provide high-accuracy measurements at deformations reaching 5%, at which poor patterns fail [182].

The evaluation and testing of patterns was performed using own MATLAB scripts by placing virtual extensometers at the edges of the tested samples. In this initial study the images containing 8-bit speckle patterns were virtually stretched up to 5% in 10 steps. Image sequences were then evaluated in open-source 2D-DIC software package Ncorr [81] with the same setting of parameters. Subset sizes of 10 px and 30 px were chosen to demonstrate the correlation between the mean correlation coefficient mentioned in the Section 4.2 and measurement errors.

As the number of speckles within the patterns increased, the measurement errors decreased. Moreover, larger sized speckles provided lower error than patterns with smaller speckles. Global

Figure 4.6: Displacement error for 10×10 px subset size.Figure 4.7: Displacement error for 30×30 px subset size.

pattern quality parameters were discussed and Shannon entropy was used as an example to demonstrate that the global measures are not sufficient to assess the quality and properties of the patterns. This is illustrated by comparing errors at different stretching magnitude for different speckle sizes (Figure 4.6 and 4.7).

Based on the research of Crammond et al. [176] and outcomes of the presented study it can be concluded that multi-criteria approach has to be addressed. So far it appears that a combination of Shannon entropy and evaluation of decay in power law distribution of correlation coefficient values provide the most accurate estimate of a pattern performance and have been implemented in the software developed along with other research presented in this thesis.

Chapter 5

Hardware

Hardware solutions fully benefiting from the lightweight algorithms for high-frequency/long-term remote measurements of displacements were developed and tested in outdoor conditions. These solutions were developed with different goals in mind; the performance-focused assembly was intended for real-time measurements with a collection of data at high sampling rates, while the reliability-focused assembly was designed primarily to withstand rain, high/low temperatures, and most importantly a lack of electricity from the grid.

All DIC measurement systems employ one or more digital cameras (stereo DIC) equipped with an optical lens. Powerful flicker-free lamps that constantly illuminate the observed contrast pattern have to be utilized. For laboratory measurements, this equipment is accessible and easy to install, however, in outdoor applications the demands on equipment increase significantly. Next, basic hardware components for DIC measurements are described and specific modifications for real-time high-frequency/long-term measurements are outlined.

5.1 Basic components for measurements

5.1.1 Camera

Reliable cameras which have a sufficient resolution and for manual focusing are essential for any DIC measurement.

On the other hand, even with state-of-the-art cameras, a DIC measurement can be easily spoiled, e.g., by setting automatic image stabilization that prevents minute shifts within a sequence of images, thus working against the efforts of the experimentalist trying to capture these changes between images.

Besides the camera resolution, a physical pixel size matters. The advancing technological development of CCD and CMOS sensors allows for the production of finer and finer semiconductor structures. As a general trend, sensor and pixel sizes shrink in order to cut more and more sensors out of one wafer [183]. This is possible because the sensitivity of the pixels increasingly enhances, too, as much as the noise performance of the electronics is being optimized. Cameras having high resolution but small pixel size, typically in cellular phones,

cannot deliver high-quality images because electrons can leap to neighboring pixels, resulting in optical noise [183]. For that reason, cameras having a full-frame sensor size but low resolution are used for image analysis, rather than high-resolution cameras equipped with small sensors. A larger sensor with larger pixels is in almost every case the technically better choice, however, the price is always higher. For example, even the high-end iPhone 8 cellular phone has a pixel size of $1.22\text{ }\mu\text{m}$ (12 Mpx resolution), while a standard industrial camera Ximea MC031MG-SY designed for computer vision has a physical pixel size of $3.45\text{ }\mu\text{m}$ (resolution 3.1 Mpx). On the other hand, portable action GoPro⁵ cameras with tiny $1/2.3''$ sensors with a pixel size of $1.55\text{ }\mu\text{m}$ were successfully employed for outdoor DIC measurements [184].



Lens sun shield

Lens

Duplicator

Camera

Figure 5.1: Industrial camera Ximea MC031MG-SY with equipped Sigma lens 80-400 VR F/4.5-5.6D ED, duplicator and camera mount reduction ring.

Camera's construction also plays an important role in image acquisition for DIC measurements. Even though cameras equipped with a mechanical shutter (DSLR) traditionally provide images of a superior quality to mirrorless ones (but the difference has been diminishing over the past decade), the mechanism of a rolling shutter is prone to wear, making DSLR less suitable for long-term measurements where the acquisition of large quantities of images can be anticipated.

5.1.2 Lenses

When conducting a DIC measurement, optical lenses must be selected properly for that particular set-up. The chosen focal length should be sufficient enough to utilize the entire field of

⁵<https://gopro.com/>

vision for the region of interest in order to maximize the pixel/physical size (px/mm) ratio. The construction and quality of the whole lens optical system also play an important role in providing undistorted images. Optical aberrations result in non-uniform geometric distortions [100] and therefore short focal lengths are not suitable—such lenses introduce large distortions of images at the edges [101–103]. Telecentric lenses focused to infinity however provide a perfect orthographic view [65] (Figure 5.2).



Figure 5.2: A scene with two identical cups (top) photographed using common objective lenses putting the objects into a perspective view (bottom left) and using telecentric lenses (bottom right) creating an orthographic view perfectly suitable for optical measurements of in-plane translations and deformations.

5.1.3 Camera mounting

Even though a false rigid-body motion due to movements of a camera can be corrected by including a fixed point into the recorded images, camera rotations or out-of-plane movements introduce hard-to-fix or even irreparable errors to a measurement. Therefore, fixing the camera using a tripod or threaded rods (in extreme circumstances, such as exposure to wind) is essential. Due to small size of modern industrial cameras and impossibility of down-scaling objective lenses, not a camera but objective lenses are mounted using a specifically designed mounting ring near the center of gravity to avoid imbalance and deformations. To avoid camera vibrations (environmental influences or artificially induced vibrations), special rubber bearing pads or gyroscope-based gimbal holders with dampers should be used.

5.1.4 Computing unit

Acquired images are sent either by a manual transfer using memory cards or any other storage medium or (preferably) using cables/wireless connection to a computer for evaluation of texture changes within the images. The computational power matters mainly in the case of real-time high-frequency measurement (see Chapter 6, Section 6.2), but capability of processing high volumes of data in a short time is convenient also in case of off-line computations (see Chapter 7).

In this regard, a remote structural health monitoring when a limited number of images per day is required, presents the least demanding application with respect to the computational power and the computations can be accomplished using only a PLC unit/small single board computer, such as Raspberry Pi¹.

When designing a computer suitable for evaluation of displacements within images using commonly available DIC packages [71, 81, 185], central processing units (CPUs) have the major impact on computational speed as these packages are not designed for graphics processing unit (GPU)-based calculations. Production technology (CPU type and brand) greatly influence the performance, while CPU's clock rate has only a minor impact on DIC calculations (Table 6.1). The separability of regions in DIC allows parallelization and therefore multi-core (multi-thread) processors accelerate the calculations (for full-field calculations or when monitoring displacements using multiple virtual extensometers). The size of random access memory (RAM) matters mainly during postprocessing [186], but its frequency and latency are crucial and presents a calculation bottleneck if inadequately slow. For outdoor applications, a protective case and must be designed to provide a sufficient resilience.

5.2 Real-time measurement at high sampling rates

For real-time measurements, industrial cameras turned out to be most suitable because of their high sampling (frame) rates, sufficient resolution and sensitivity, pixel size, reliability, and availability of APIs for user-friendly development.

Wide range of C-mount thread industrial cameras plays the key role in area of computer vision nowadays. C-mount thread reduction rings enable using objective lenses designed, e.g., for Nikon DSLR cameras having F-mount thread in combination with these compact sensors. Magnification elements (duplicator or quadruplicator) enable to achieve higher focal lengths and thus increasing overall zooming ability of the whole optical system.

With such an advanced recording equipment, it is desired to avoid bottlenecks during the data transfer. If a user requires saving captured images during the measurement, solid state drive (SSD) is the prudent option. Nevertheless, selection of a proper communication port and connecting cable cannot be neglected. In this regard, usage of USB 3.x or Gigabit Ethernet (GigE) interfaces are recommended. It is important to keep in mind that the used cable must be shielded and cannot exceed 10 m in length. If longer cables are used, they must be active (externally supplied with electricity) because of relatively high consumption of cameras (typically

¹<https://www.raspberrypi.org/>

about 2 A at 5 V), causing undesirable voltage drop.

Regarding the data transfer, optic fibers are a promising technology for extreme applications when high-speed cameras are utilized. Because these fibers are not capable of conducting electricity, an additional power supply for the camera must be provided. In addition, powerful cameras require active cooling; the higher the temperature on a sensor, the higher the optical noise.

The PCI express (second generation) cards is nowadays recommended by manufacturers for state-of-the art cameras instead of USB 3.1, increasing the bandwidth from 10 GBit/s to 20 GBit/s and more. Such a bandwidth is needed for, e.g., 50 Mpx at 22 fps and 12 bit depth¹.



Figure 5.3: Real-time measurement of bridge deflections under the passing traffic.

5.3 Remote long-term monitoring

For a remote long-term monitoring, the demands on sampling rates are not usually high. To assess development of cracks or movements of structural elements under the quasi-static loading due to a loss of stiffness caused by degradation construction materials, only about an image a day can be considered sufficient for the monitoring. Such a measurement can be challenging, especially when considering a fully autonomous off-grid solution. Special measuring unit has been designed for a remote monitoring of an unstable rock massif near Vrané nad Vltavou, Czech Republic (Figure 5.4).

The basic requirements on a remote long-term monitoring system can be summarized as follows:

¹<https://www.ximea.com>

1. Reliability—the remote measurement line is often out of reach, which can be easily resolved using remote control when connected to a grid, but off-grid solutions being idle most of the time require a GSM- or Wi-Fi (if available) remote switch; it is important to send a log-file during each session to a server, containing the information about voltage on battery provided by a voltmeter and CPU temperature for an elementary diagnostics.
2. Availability of GSM, at least 3G, optimally 4G (LTE)—the images are analyzed on a cloud server to avoid energy consumption due to excessive loading of the CPU unit and enable back-up of the data; it is inconvenient to store the data on the integrated SD card because of its limited service life and capacity.
3. Weather-resistance—low temperatures can shorten the battery life and capacity, while high temperatures impose a risk of damaging the electrical circuits and components and introduce an additional optical noise during image acquisition; the exposure to low temperatures can result in vapor condensation and therefore the protective box must be completely sealed at cold and dry environment and silica gel should be placed inside.
4. Longevity of components—for example, DSLR cameras cannot be used for this type of applications due to wear of shutter components that require replacement after capturing about 200k images.

For an on-going project, the PLC unit has been represented by a Raspberry Pi 3 single-board computer. The unit was assembled using a Raspberry Pi 3 v.2 NoIR camera, GSM LTE modem, AGM 12 V gel battery, solar panel for charging the battery, charge controller, and DC-to-DC bulk converter. While the charge controller was included to regulate the charging current and taper it as the battery reaches fully charged voltage, DC-to-DC lowered the relatively high voltage on the battery (about 12 V) to 5 V required by the Raspberry PLC board. In order to save as much energy as possible, the turning on/off cycles were controlled using a Sleepy Pi power management board, playing the role of a real-time clock (RTC) trigger. Scheme of this assembly is provided in Figure 5.5 and its work-flow diagram is presented in Figure 5.6.

After turning on the PLC unit (Raspberry Pi), the computer first establishes a connection with a cloud at which the data are further processed (Figure 5.6). Next, the camera is initialized, images are taken and uploaded to the cloud along with a log-file. Once the process is successfully finished, the PLC unit is switched off to save energy. This strategy proved to be reasonable since the measurement has operated continuously for over 11 months and yields 2 images each day. This experiment is very valuable in terms of experience to be exploited if reproduced in the future; the main issues encountered and respective measures/solutions adopted during the project are summarized in Table 5.1.



Figure 5.4: Assembly for a long-term remote monitoring of an unstable rock massif.

Table 5.1: Issues related to long-term remote measurements

Issue	Measures/Solution
Camera movement	Fixed reference point in the frame, fixed stiff attachment to the ground
Low temperatures	Heating using resistance wires
High temperatures	Active or passive cooling system
Direct sunlight	Camera shielding
Memory media failure	Data synchronization with a cloud server
Illumination failure	Redundant light source
Power source failure	Redundant power source connected in-parallel, optimally to an independent branch
Unstable GSM signal	External antenna with a high gain
High power consumption of GSM modem	External trigger for waking the modem up (only) when needed

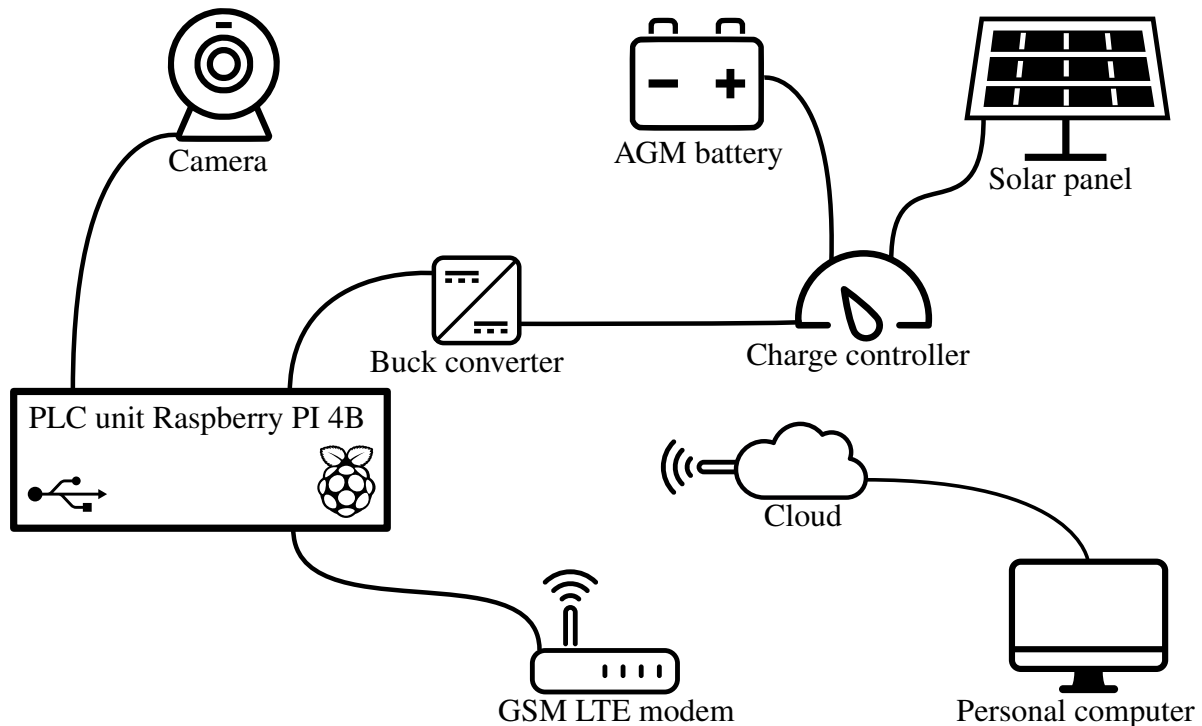


Figure 5.5: Scheme of an autonomous assembly for a long monitoring.

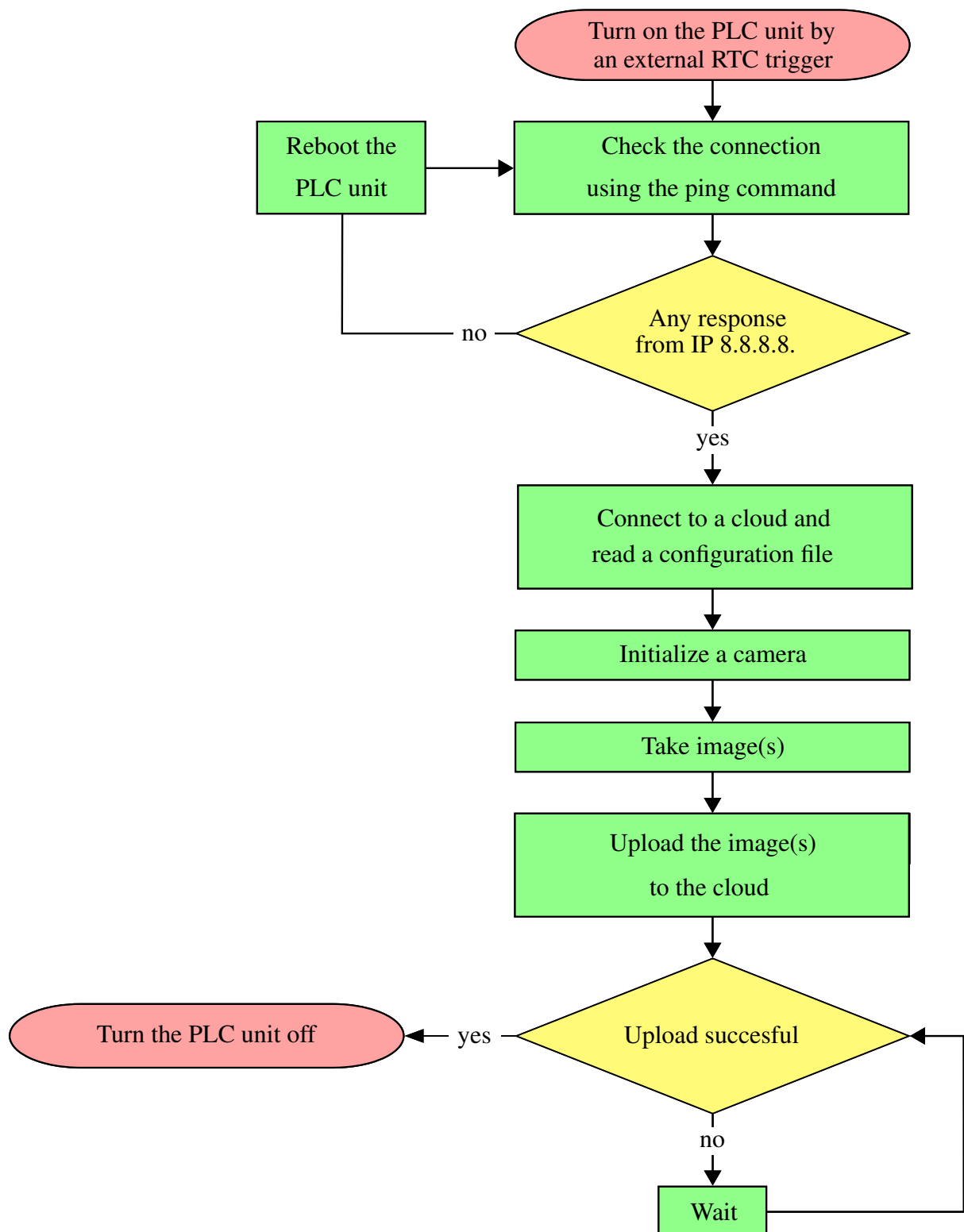


Figure 5.6: Work-flow diagram for a long-term remote measurement.

Chapter 6

Real-time measurements

Based on: J. Antoš, V. Nežerka, and M. Somr, Real-time optical measurement of displacements using subpixel image registration, *Experimental Techniques* 43 (2019) 315–323, doi: [10.1007/s40799-019-00315-1](https://doi.org/10.1007/s40799-019-00315-1)

Despite the rapid emergence of advanced turnkey commercial DIC systems during the last two decades [187], a simple open-source DIC tool for real-time monitoring displacements has not been available. The proposed solution offers real-time measurement of displacements in 2D at predefined locations by using virtual extensometers, being a couple of pixel subsets. The developed open-source software utilizes algorithms based on discrete Fourier transform (DFT) optimized for fast evaluation of subset translations with subpixel accuracy. It is worth mentioning that real-time 3D positioning and tracking systems have been developed [188], but these require much more sophisticated equipment, skilled operators, and their use is usually limited to laboratory conditions.

The real-time measurement system proposed here consists of three fundamental elements: a camera, a communication channel (cable or wireless), and a computer. There are several requirements on the camera, including high resolution, low digital noise, and a long lifetime period. The last requirement rules out reflex cameras that have a limited lifespan regarding the number of acquired images. On the other hand, cameras equipped with monochrome CMOS (complementary metal-oxide-semiconductor) chips allow for obtaining the same or higher spatial resolution with the satisfying sensitivity at a lower price. The communication channel should not be the weakest link in the system; commonly used USB 3.x or Ethernet cables are sufficient and reliable.

Besides these basic components, a strong illumination is recommended to reduce digital noise by allowing a high signal to noise ratio. High levels of illumination also enable a reduction in a lens diaphragm opening by setting lower f-number (aperture), resulting in a higher depth of field for the acquired images. This is particularly advantageous if the observed surface is uneven. Moreover, a sufficient exposure can be reached at higher shutter speed, providing blur-free images at higher displacement/deformation rates.

6.1 Algorithms and program work flow

The developed software tool RTCorr (Real-Time Correlation) for real-time optical measurement of displacements was developed in Python 3.6. It offers a user-friendly graphical user interface (GUI), see Figure 6.1, enabling placement and management of virtual extensometers, setting DIC parameters, and export of data. In addition, it provides information about the camera chip temperature and allows for precise focusing by calculation of a mean intensity gradient [58, 189], defined as

$$\Psi_f = \sum_{i=1}^W \sum_{j=1}^H |\nabla f(x, y)| \frac{1}{WH}, \quad (6.1)$$

where $|\nabla f(x, y)| = \sqrt{f_x(x, y)^2 + f_y(x, y)^2}$, in which $f_x(x, y)$ and $f_y(x, y)$ are the x - and y -directional intensity derivatives at pixel located at (x, y) within the image f , respectively. W and H are the image width and height, respectively. After zooming to a region of interest, maximizing Ψ leads to a perfect camera focus, see the demonstration in Figure 6.2.

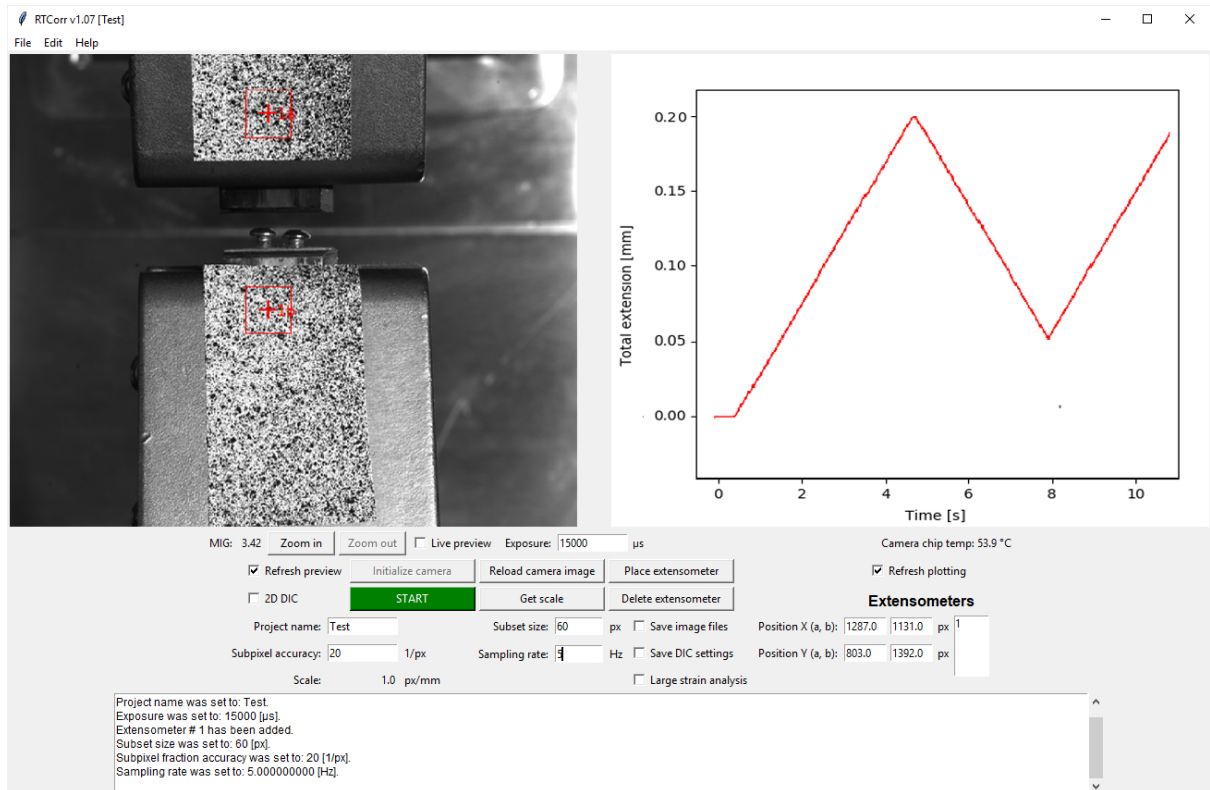


Figure 6.1: Graphical user interface of RTCorr v1.07.

6.1.1 Sub-pixel registration

RTCorr employs the upsampled matrix-multiplication discrete Fourier transform (DFT), proposed by Guizar-Sicairos et al. [158], to reach subpixel accuracy of aligning subsets. Using

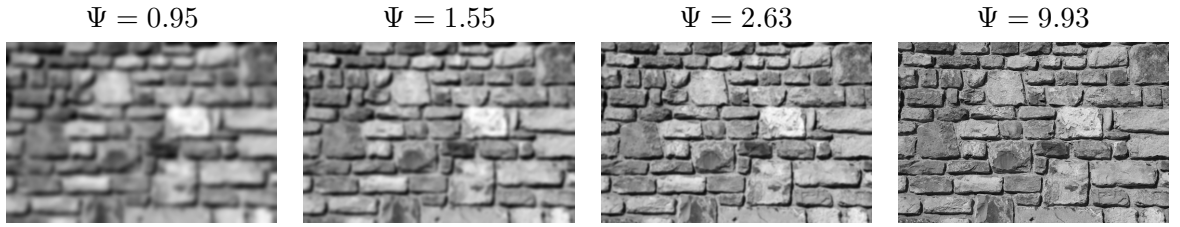


Figure 6.2: Dependence of the mean intensity gradient on a camera focus.

this approach, cross-correlation for each square subset of pixels of a side length N is accomplished in a frequency domain [190, 191]. The utilization of Fourier transform renders the registration computationally efficient [134] and insensitive to optical noise or changes in illumination [142, 143]. Unlike the majority of DIC software, based on determining locations of reference subsets within current images, the subsets in RTCorr are fixed and represent an imaginary window through which a motion of the underlying pattern is observed. Since the pixel subsets are registered by phase retrieval, only their translation is evaluated, and the displacement field is averaged over the subset area.

The employed registration algorithm is capable of computing subset shifts within a fraction of a pixel, $1/\kappa$. The difference between the pixel and subpixel accuracy of results is clearly illustrated in Figure 6.3 on an example of a 2D displacement field, calculated considering $\kappa = 1 \text{ px}^{-1}$ (pixel accuracy) and $\kappa = 50 \text{ px}^{-1}$ (subpixel accuracy).

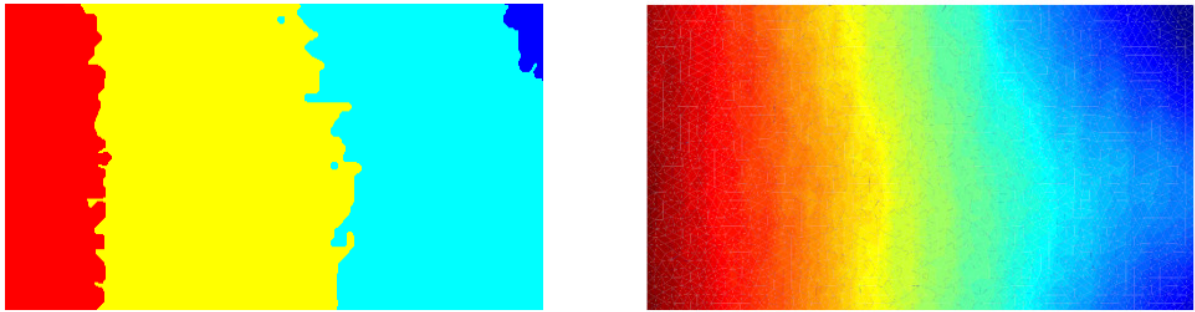


Figure 6.3: Illustration of pixel (left) and subpixel (right) accuracy of displacements ranging between 0.2 and 3.7 pixels on results of a direct tensile test.

The program is capable of accomplishing simultaneous measurements of relative displacements in 2D using an arbitrary number of virtual extensometers, equivalent to physical ones. A full-field 2D DIC analysis can be carried out once the measurement is finished from the acquired images that are saved (if required) to a project folder. The measurement is carried out in pixels, but it can be scaled to physical units. Otherwise, it is carried out in pixels. The collected data are saved on a hard drive during the measurement so that they cannot be lost in the case of a software crash. The saved data include time steps, displacements of extensometer ends and relative displacements, calculated as the ratio of an extensometer extension to its length.

The source files and manual with a thorough description of the program structure and GUI controls are provided at GitHub [185].

6.1.2 Registration of large displacements

In the small-displacement mode, reaching up to about $1/4N$, the shift of subsets $\Delta\mathbf{u}$ at a time T is calculated by comparing their configuration with the one in a reference image acquired at $T = 0$, so that

$$\mathbf{u}(T) = \Delta\mathbf{u}(0, T). \quad (6.2)$$

RTCorr also offers a large-displacement mode, in which the shift is calculated as

$$\mathbf{u}(T) = \Delta\mathbf{u}(T - 1, T) + \mathbf{u}(T - 1). \quad (6.3)$$

By relating the subsets at time T to their configuration at $T - 1$, an arbitrary displacement can be tracked, limited only by the ROI size. However, the displacement of a subset between T and $T - 1$ still should not exceed the value of $1/4N$. The large-displacement mode should be used only if needed because summing the measured shifts may result in accumulating measurement errors.

The small-displacement mode is analogic to the Eulerian approach to observing motion of a body [192]. In this mode the deformed and shifted image flows through the fixed extensometers. In the large-displacement mode the extensometers deform with the underlying image and their position is updated for each frame, analogically to the Lagrangian approach [193]. This allows for evaluating displacements exceeding the subset size and severe deformations of subsets.

6.2 Testing and validation

The testing and validation were primarily accomplished on a custom-built desktop computer equipped with an Intel 4 core i3-8350K CPU, 16 GB RAM, and 500 GB SSD hard drive. Besides, performance tests were carried out on three different computers, all listed in Table 6.1; CPU π_{10^6} test score refers to a time needed to computing 10^6 digits of π using SymPy package in Python. All the computers were equipped with a USB 3.1 hub.

Table 6.1: Computers used for the performance tests; the abbreviations in parentheses are used in the following figures

Computer	CPU (CPU cores)	π_{10^6} test	Operating system
Laptop Lenovo T440 (L1)	Intel i5-4200U, 1.6 GHz (4)	72.91 s	Ubuntu 18.04.1
Laptop Lenovo T480 (L2)	Intel i5-8250U, 1.6 GHz (8)	52.31 s	Ubuntu 18.04.1
Custom-built desktop (D1)	Intel i3-8350K, 4.4 GHz (4)	44.34 s	Ubuntu 18.04.1
Desktop Dell T1600 (D2)	Intel Xeon E31280, 3.5 GHz (8)	51.69 s	Ubuntu 18.04.1

The images were taken using a Ximea MC050MG-SY monochromatic camera, equipped with a $3.45 \times 3.45 \mu\text{m}$ pixel-size CMOS sensor capable of delivering 76 frames per second at a 5 Mpx resolution. Low distortion was ensured by using a Kowa LM50HC C-mount objective lens with a fixed focal length of 50 mm. Using long objective lenses is favorable to reduce the

distortions if telecentric lenses are not available. The data transfer was accomplished using a USB 3.1 cable.

With the specified hardware configuration and setting of DIC parameters as $N = 36$ px and $\kappa = 32 \text{ px}^{-1}$, the maximum sampling frequency ν reached for a single extensometer was equal to 67.05 ± 0.22 Hz, see Figure 6.4. The results of the performance study and the π_{10^6} test demonstrate that the maximum sampling frequency ν is proportional to the CPU speed.

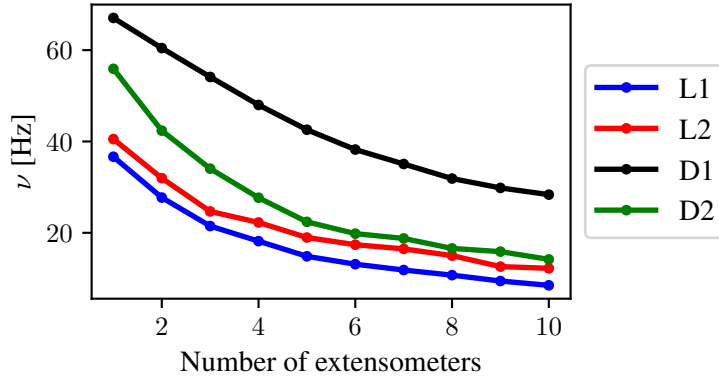


Figure 6.4: Relationship between the maximum sampling frequency ν and a number of extensometers with the specified hardware available and setting of DIC parameters as $N = 132$ px and $\kappa = 128 \text{ px}^{-1}$.

6.2.1 Measurement bias

A static test with a perfectly fixed specimen was performed in order to assess the systematic error of the measurement system. The camera was focused on a random pattern, consisting of black speckles ranging approximately between 0.05 and 2 mm in diameter, applied to an illuminated white wall. LED lights with a constant current driver were used provide flicker-free illumination. The distance between the camera and the observed surface was 50 cm, yielding a scaling factor of 22.89 px/mm.

The study was focused on the impact of a subset size N and the required subpixel accuracy κ on measurement errors and a maximum sampling frequency ν . The impact on ν was studied when using 10 virtual extensometers to highlight the role of CPU speed. The observed random pattern contained speckles small enough so that even the smallest studied subset of $N = 4$ px was unique in its neighborhood and contained sufficient amount of features to track. With larger N the pattern randomness within subsets increased, as demonstrated by their entropy [177], see Figure 6.5. The entropies of the model subsets were calculated as

$$H = - \sum p_k \log_2(p_k), \quad (6.4)$$

where k is the number of intensity levels within subsets, and p_k is the probability associated with the particular intensity level [194]. The length of a virtual extensometer, i.e., the distance between the centroids of two coupled subsets, was 100 mm. The oscillations of the extensometer extensions were monitored for 10 min at a maximum possible sampling frequency. The

measurement variation σ was calculated as a standard deviation of relative extensions:

$$\sigma = \sqrt{\frac{\sum_{i=1}^n \epsilon_k^2}{n}}, \quad (6.5)$$

where n is a number of images (measurements) and ϵ_k is a relative extension of the k^{th} measurement, calculated as the ratio of the extensometer extension to its length, i.e., strain.

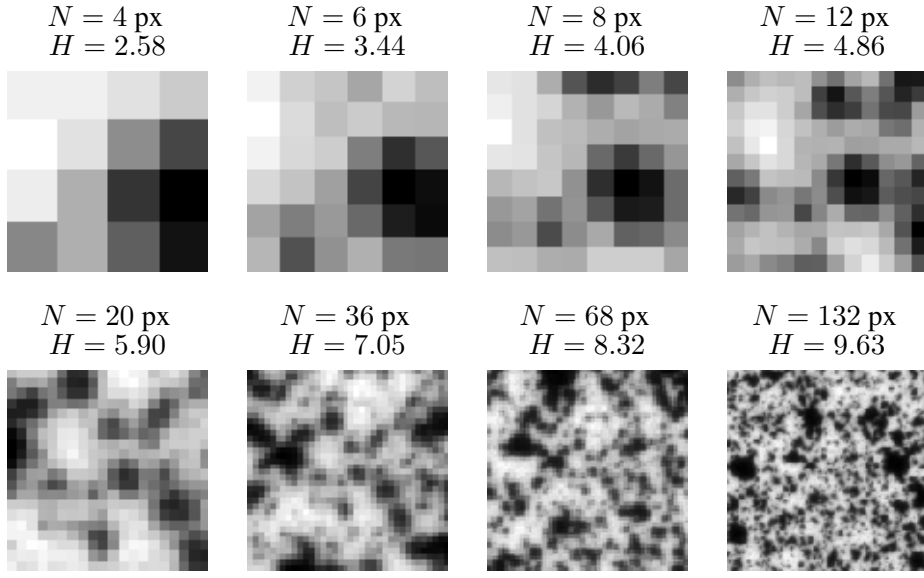


Figure 6.5: Studied subsets of various size, $N \times N$, and their entropy, H , being a measure of gray intensity randomness.

The relationships between the both user-defined DIC parameters, N and κ , and the system performance in terms of σ and ν are presented in Figures 6.6 and 6.7. First, $\kappa = 32 \text{ px}^{-1}$ was fixed and the influence of N was tested. Next, $N = 36 \text{ px}$ was fixed and the same procedure was repeated for κ .

Larger subsets contribute to a lower oscillation around the true (zero) extension, and the measurement variation, σ , was very small, around 0.8×10^{-5} , and almost constant for $N > 70 \text{ px}$. However, increasing the subset size, N , came at a cost of higher demands on CPU resulting in a lower sampling frequency, ν , and the measured shift was averaged over a larger area. The value of ν was dependent on the CPU speed.

An opposite trend was observed regarding κ . For values of $\kappa < 4 \text{ px}^{-1}$ there was no oscillation in extensions and $\sigma = 0$. The measurement variation stabilized for $\kappa > 40 \text{ px}^{-1}$ at $\sigma \approx 1.5 \times 10^{-5}$. The impact of κ on ν was similar to the impact of N . With increasing κ , ν decreased exponentially and its value was also dependent on the CPU speed.

It may be concluded that for the hardware used and the experimental setup considered here, the optimum setting of the image registration parameters is $N \approx 40 \text{ px}$ and $\kappa \leq 4 \text{ px}^{-1}$ if large displacements are anticipated or $\kappa \geq 60 \text{ px}^{-1}$ for measurement of small displacements where setting of high κ makes sense. The measurement error, σ , appears to be constant beyond these thresholds.

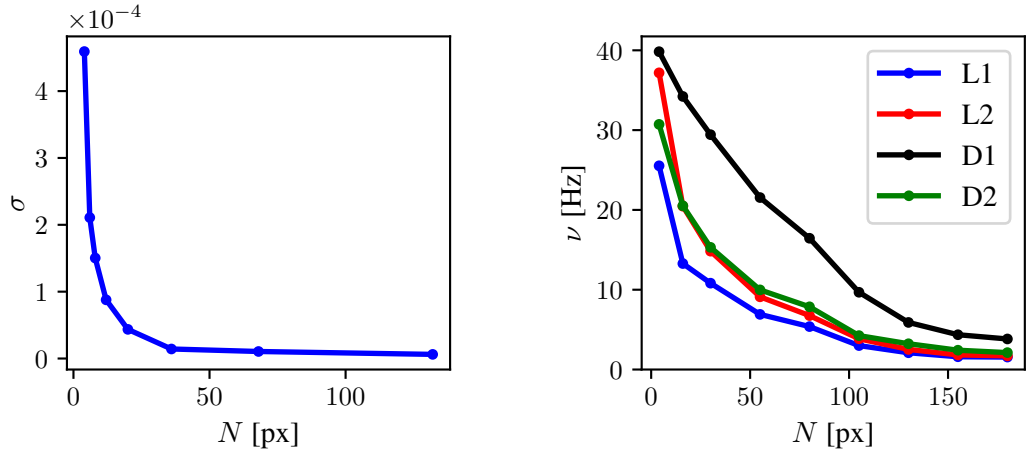


Figure 6.6: Relationship between the subset size and the measurement variation of results (left) and the maximum sampling frequency (right); the required subpixel accuracy was fixed at $\kappa = 32 \text{ px}^{-1}$.

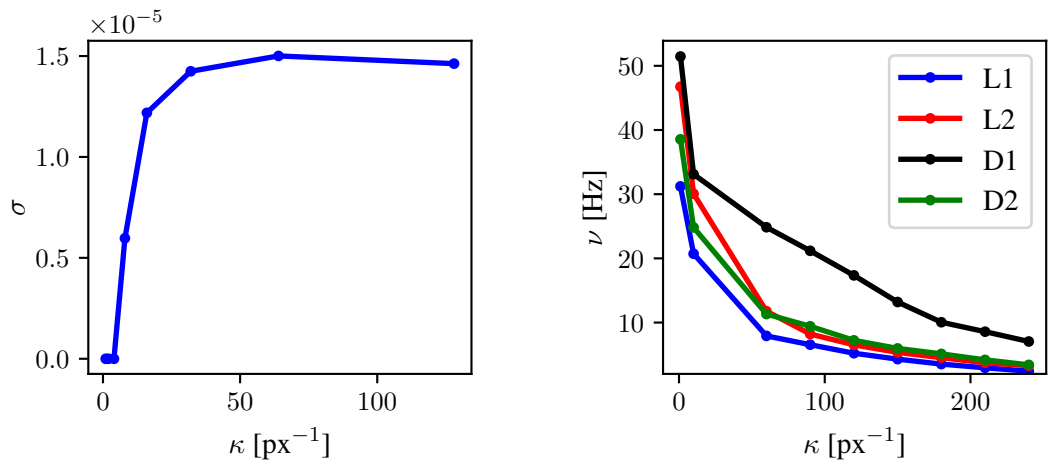


Figure 6.7: Relationship between the required subpixel accuracy and the measurement variation of results (left) and the maximum sampling frequency (right); the subset size was fixed at $N = 36 \text{ px}$.

6.2.2 Experimental verification

A periodically displaced steel plate with a sprayed random pattern was observed and the vertical motion evaluated in order to verify the measurement procedure thoroughly. The periodic harmonic motion was accomplished using a hydraulic dynamic actuator. The camera was positioned perpendicularly to the observed plane at a distance of 60 cm. The camera was turned on 5 minutes before the experimental testing in order to reach a saturation temperature and eliminate the error due to the camera self-heating [195]. The correlation parameters were set as $N = 80$ px and $\kappa = 60$ px⁻¹. The displacements were recorded during 10 sine waves having an amplitude of 0.93 mm and frequency 0.017 Hz. The images were saved during the analysis, thus significantly reducing the sampling frequency to approximately 0.5 Hz.

The saved images were collected and used after the test for a calculation of displacements using a DIC software Ncorr. This software was thoroughly tested and validated using distorted synthetic images and analysis of experimental datasets from the SEM 2D-DIC challenge [81, 196]. Ncorr was selected for benchmarking because it is robust, open-source, and accepted by a scientific community [197]. However, the algorithms implemented in Ncorr, based on subset matching in the spatial domain, do not allow for the real-time analysis.

The measurement was carried out twice, separately for the modes for small and large displacements, recall Section 6.1.2. The comparison of vertical displacement, $y(T)$, evaluated using RTCorr and Ncorr and deviations from the theoretical curves, Δy , are provided in Figures 6.8 and 6.9. The theoretical curves follow the prescribed harmonic displacement function defined as

$$y(T) = 0.93 \sin(2\pi 0.017T). \quad (6.6)$$

There was an almost perfect overlap of curves (theoretical according to Eq. (6.6)) and outcomes of Ncorr and real-time measurement using RTCorr, manifesting a high accuracy of the real-time correlation procedure. The Δy plots provide more detailed information about the measurement errors. The encountered discrepancy, in order of 10^{-5} m, between the measured vertical displacements, both by RTCorr and Ncorr, is attributed to asynchronous motion of the observed specimen with respect to the prescribed displacement according to Eq. (6.6). More importantly, there is an agreement between RTCorr and Ncorr. The possible error cumulation was not observed in the case of RTCorr measurement in large-displacement mode. However, compared to the small-displacement mode, the disagreement between Ncorr and RTCorr was slightly increased.

6.2.3 Outdoor measurements

RTCorr was primarily developed for and tested during laboratory measurements, but it can be exploited for structural health monitoring [198, 199]. To demonstrate that capability, experimental measurements of deflections of bridges under traffic loading were carried out. Such measurements enabled continuous monitoring without affecting the traffic.

It must be noted that such outdoor measurements have to be thoroughly prepared, especially in the case of long-term monitoring. The accuracy of DIC measurements carried out outdoors can be more likely compromised due to temperature changes, camera motion, turbulences, or poor illumination [65].

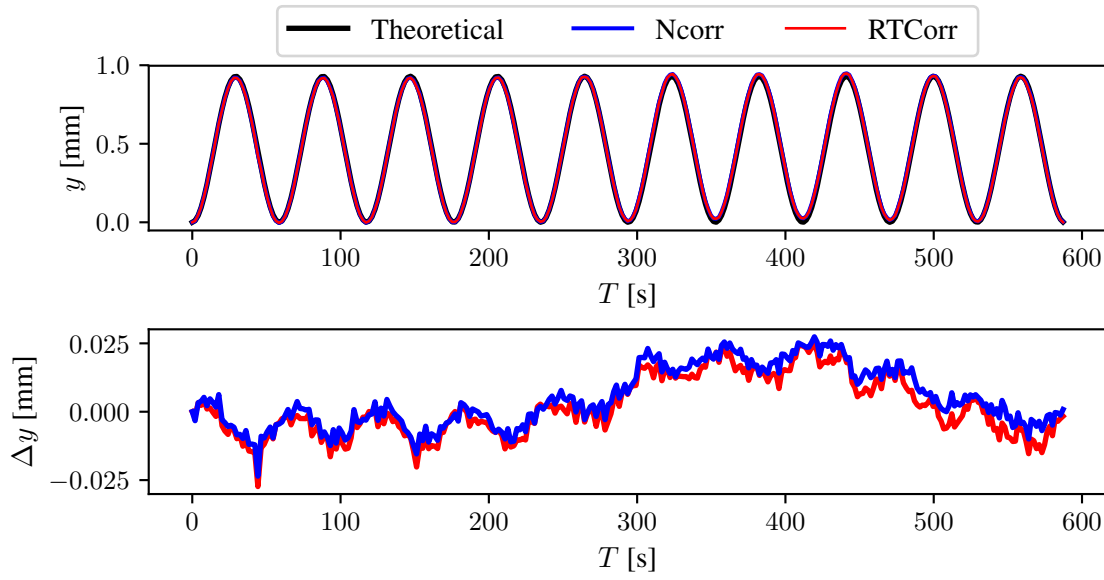


Figure 6.8: Comparison of theoretical displacement and results from RTCorr and Ncorr (top) and deviations from a theoretical curve (bottom) in the small-displacement mode.

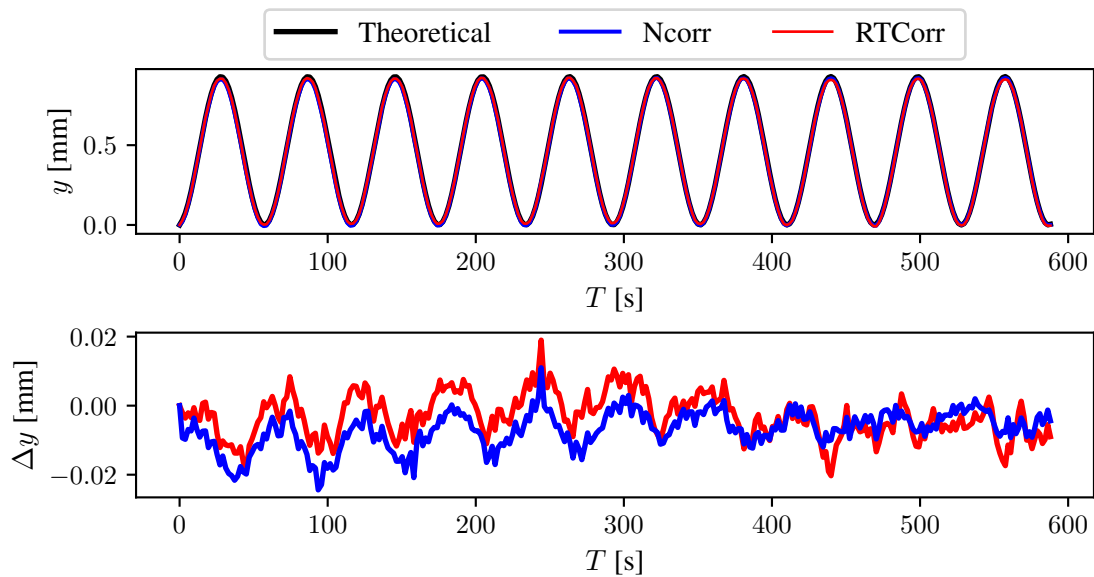


Figure 6.9: Comparison of results from RTCorr and Ncorr (top) and deviations from a theoretical curve (bottom) in the large-displacement mode.

The displacements were recorded from a 11 m distance, yielding a scaling factor of 1.16 px/mm. The sampling frequency was set to 5 Hz for 1 h and the DIC parameters as $N = 70$ px and $\kappa = 20$ px $^{-1}$. The measurement setup is presented Figure 6.10 and the results in Figure 6.11. Even though there are no reference data, the maximum deflections correspond to predictions based on previous measurements. Moreover, there is a proportionality between the train weight and measured deflections. The high sampling frequency allowed to capture also the bridge vibrations after its unloading.



Figure 6.10: Real-time measurement of a steel bridge deflection under a 40 t train engine using RTCorr.

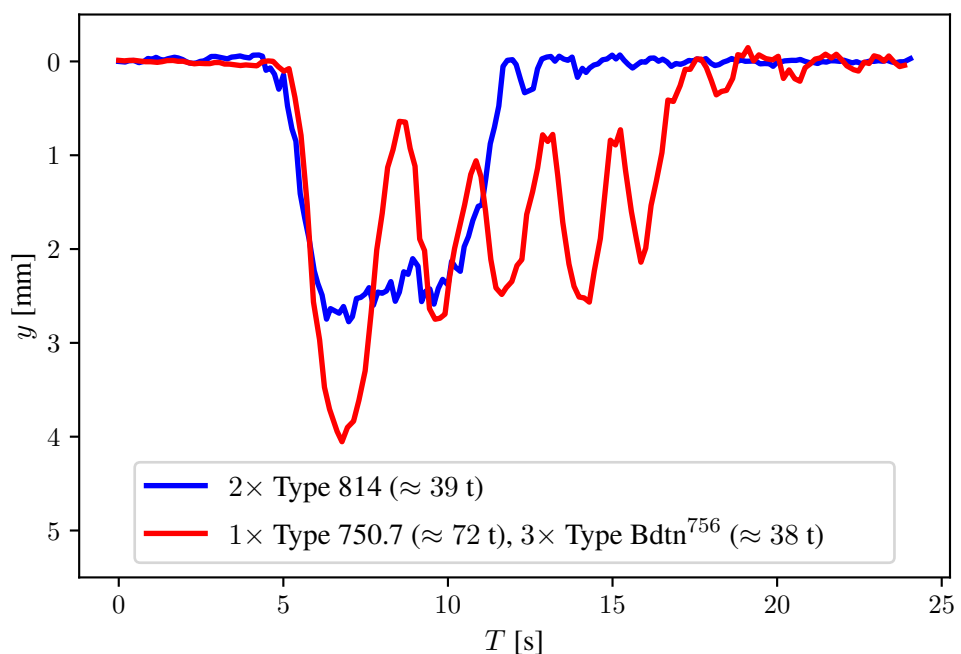


Figure 6.11: Bridge deflection due to loading by a passing train measured near the midspan.

Chapter 7

Off-line mode measurements

It is indisputable that the simplicity and low computational cost of the image registration algorithms employed for displacement measurements in this work make the method suitable for real-time measurements, especially when using miniified equipment. However, the same algorithms are suitable also for batch processing of large amount of data, e.g., generated by long-term measurements or, typically, by high-speed cameras. High speed imaging opens up a range of new possibilities to tackle dynamic or impact behavior of structures, but the basic principle of DIC in itself is unchanged. Yet, many software tools are unable to process hundreds of thousands images that can document a dynamic event. Here, the advantage of using computationally efficient subpixel registration algorithms implemented in the developed software RTCorr is presented using two examples—recording minute vibrations due to sound excitation on over 80,000 images and modal analysis of an aircraft wing from a video sequence.

7.1 Audio recovery

The reproduction of the experiment presented by Davis et al. [200] demonstrated offline capabilities of the developed algorithms for measurement of displacements. Davis et al. proposed a passive method to recover audio signal from a sequence of images recorded using a high-speed camera. By detecting tiny vibrations of an object excited by a sound, the displacements can be converted back into an audio signal.

Such an approach of audio recovery is based on the principle of traditional microphones that convert motion of an diaphragm into an electrical signal. Here, a microphone diaphragm was replaced by a withered part of a potted plant's leaf (Figure 7.1), having a rich texture suitable for image registration. The images were taken using an iX i-SPEED 726 high-speed camera equipped with CMOS sensor with a $13.5\text{ }\mu\text{m}$ pixel size at a frame rate of 20,000 fps and 1344×978 px resolution.

The experiment fully tested the proposed methodology for calculation of local displacement fields since over 4 second recording at 20,000 fps yielded an enormous amount of images to be processed and commonly used DIC software, such as Ncorr or VIC 2D, cannot handle such an amount of data. On the contrary, calculation of 50×50 subset's displacements with 1/200 px accuracy took only about 7 minutes using the Lenovo T480 laptop specified in

Section 6, Table 6.1. Since the resulting 1D signal obtained in the form of the subset displacements was correlated with the input pressure of sound waves, it could be played and analyzed as sound.



Figure 7.1: Experimental setup: leafs of potted plant excited by a sound from a loudspeaker; a powerful LED illumination is required for high frame rate recording.

At first, synthetic tones of 200, 400, 600, 800, and 1000 Hz were played by a loudspeaker to validate the procedure. It can be seen from the spectral analysis presented in Figure 7.2 that the frequency peaks of the reproduced sound match those played by the loudspeaker. The observed potted plant's leaf resonated with a different normalized amplitude for each frequency.

After successful validation, a piano solo of the Beethoven's famous composition Für Elise was played by the loudspeaker and the leaf vibrations were monitored. The sound reproduced from the leaf displacements can be easily recognized by a human and the similarity is demonstrated by a sound spectra plot shown in Figure 7.3. The presented audio recovery procedure is sensitive to noise at low frequencies (lower than 300 Hz). This noise can be attributed to movement of the camera induced by a cooling fan. Vibrations of the leaf due to draft were eliminated by a high-pass filter eliminating all displacements with a frequency lower than 20 Hz.

7.2 Modal analysis

Conventionally, mode shapes of structures have been extracted using contact-based sensors such as accelerometers [201, 202]. Even though accelerometers can be easily attached and are capable of providing high sampling rates and high signal-to-noise ratio [203], they cannot provide full-field data and given their weight, they may constitute a significant component of a measured structure, especially in case of small/lightweight vibrating bodies. These drawbacks have been eliminated by introduction of DIC-based measurements, which also allow retrospective evaluation of dynamic events from a sequence of images [121, 204–210].

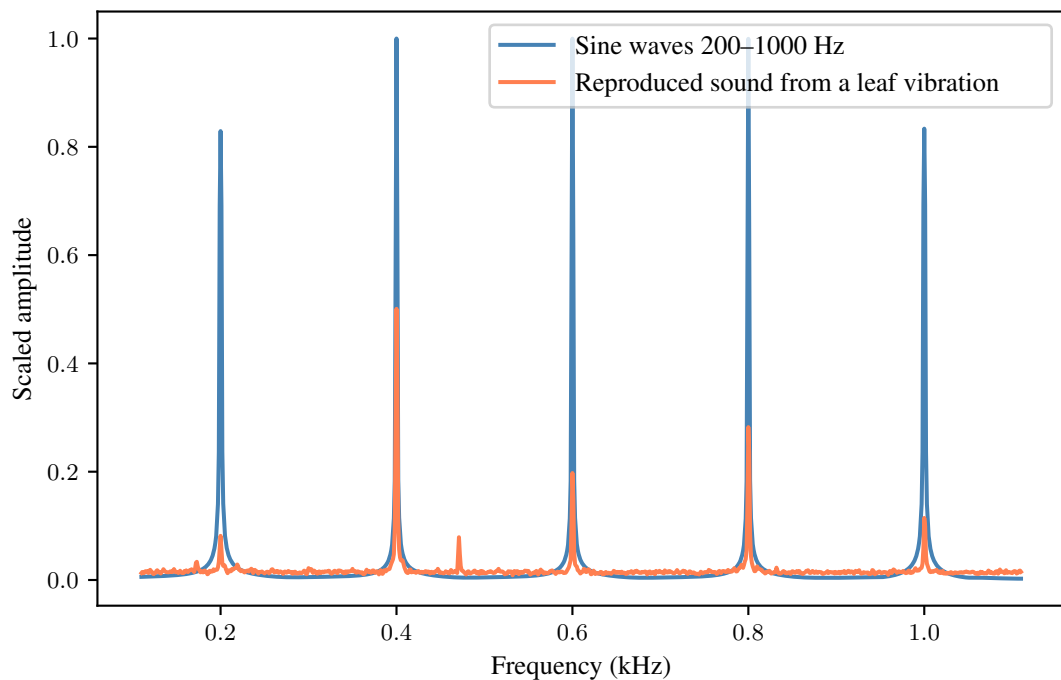


Figure 7.2: Comparison original and recovered synthetic tones of 200, 400, 600, 800, and 1,000 Hz using spectral analysis.

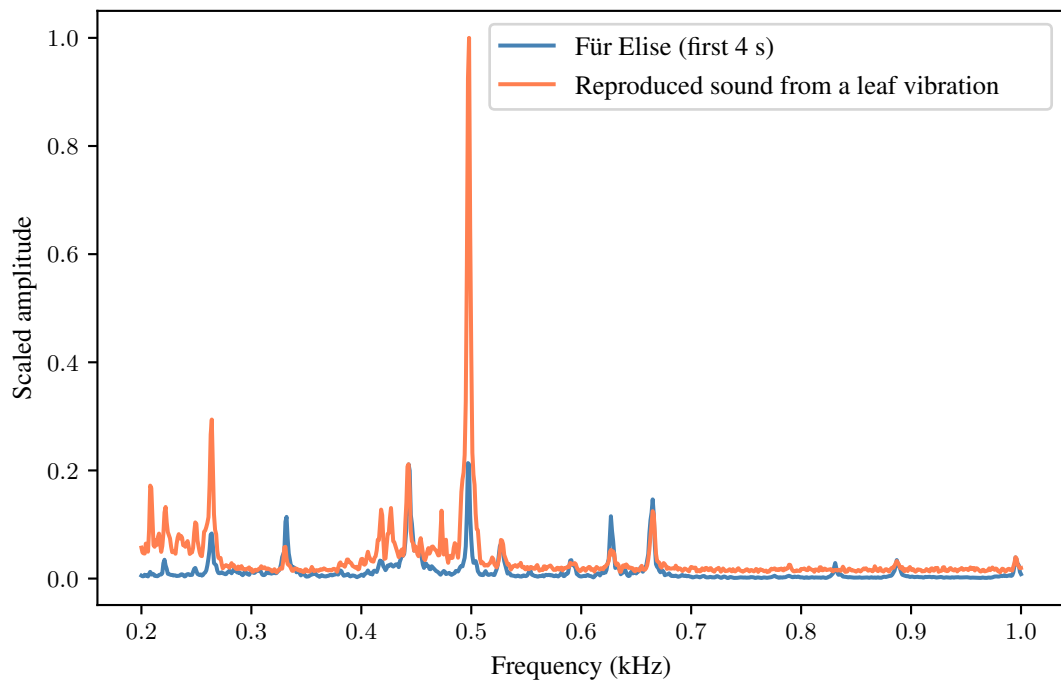


Figure 7.3: Comparison original and recovered beginning of the Mozart's Für Elise spectral analysis.

Example of such a measurement using subpixel registration algorithms is provided in Figure 7.4. Here, a slow-motion recording of an Airbus A380 aircraft taking off at the Düsseldorf Airport, Germany, was used for the analysis of wing vibration. The video was recorded at the sampling rate of 1,000 fps. The use of efficient image registration algorithms allowed to carry out the modal analysis in less than 10 s of computational time using the Lenovo T480 laptop specified in Section 6, Table 6.1.

The first natural frequency of bending vibration identified by registration of subsets' displacement was equal to 8.85 Hz, which is in agreement with numerical calculations by Ghaith and Haque [211]. Their study carried out using ABAQUS software described the dynamics of an Airbus A380 wing; the numerical model predicted the first natural frequency of 8.082 Hz. However, this value can be influenced by the amount of fuel carried by the wing tanks.



Figure 7.4: Upscaled first mode amplitudes at monitoring subsets with a maximum first-mode deflection $u_{y,\max}^I = 150$ mm measured at the end of an Airbus A380 wing.

Conducting a modal analysis under operating conditions offers involvement of sometimes hardly anticipated excitation. In such a case, besides affecting the dynamics of the system, use of accelerometers presents an additional obstacle since these delicate devices require careful handling and usually also connection to a PLC unit. The use of efficient algorithms for evaluation of natural frequencies from a video stream can provide a useful tool in the area of health monitoring or quality control as any deviations in dynamic behavior can indicate a presence of defects [212, 213].

Chapter 8

Conclusions and Final Remarks

The demand for DIC-based measurement system capable of real-time evaluation of displacements led to development of solutions presented in this thesis. Such solutions, usually exploited outdoors for structural health assessment, pose specific requirements on both hardware and software. Here, an optical system for real-time measurements of displacements offering an arbitrary number of virtual extensometers was presented. High sampling rates were reached through an efficient image registration algorithm based on upsampled matrix-multiplication DFT. A careful performance-focused implementation of this algorithm in an in-house software allowed to reach sampling frequencies exceeding 60 Hz with a 1/100 px subpixel accuracy. The software was validated on a series of laboratory and outdoor measurements, exploiting several measurement techniques for benchmarking to prove the developed software accurate and reliable.

The hardware was designed and tested for two modes of measurements with different goals in mind; the performance-focused assembly was intended for real-time measurements with collection of data at high sampling rates, while the reliability-focused assembly was designed primarily to withstand long-term exposure to variable weather conditions and possibly a lack of electricity from the grid. Both solutions were thoroughly tested both in laboratory and outdoor conditions.

The proposed method is robust and very fast, but an experimentalist using the proposed algorithms must be familiar with their limitations:

- Large translations of a subset within a single time-step (between two frames/images) are not allowed because correlation with a reference frame/image to seek for initial location of translated subsets with an integer-pixel accuracy was eliminated from the process.
- Large deformations of a subset in a single time-step are not allowed because subsets are assumed to be undeformable.

These restrictions allow efficient evaluation of subset translations in a single steps and do not limit measurements in most applications; when monitoring, e.g., bridge deflections from a distance, local deformations are negligible and displacements do not exceed the size of subsets required for a the measurement.

The developed solution has not gained only the interest of scientific community, as evidenced by the growing number of citations in peer-reviewed papers, but also engineers. In November 2019, deflections were monitored on a highway bridge (Figure 8.1) on a request of Ředitelství silnic a dálnic (ŘSD) ČR (Directorate of Roads and Motorways Czech Republic). This proof-of-concept measurement took place near on a 25 m long precast prestressed concrete bridge on the D5 highway⁶, near Drahelčice/Rudná (D5-005..1, 3.927 km). Future measurements for ŘSD ČR are prearranged.

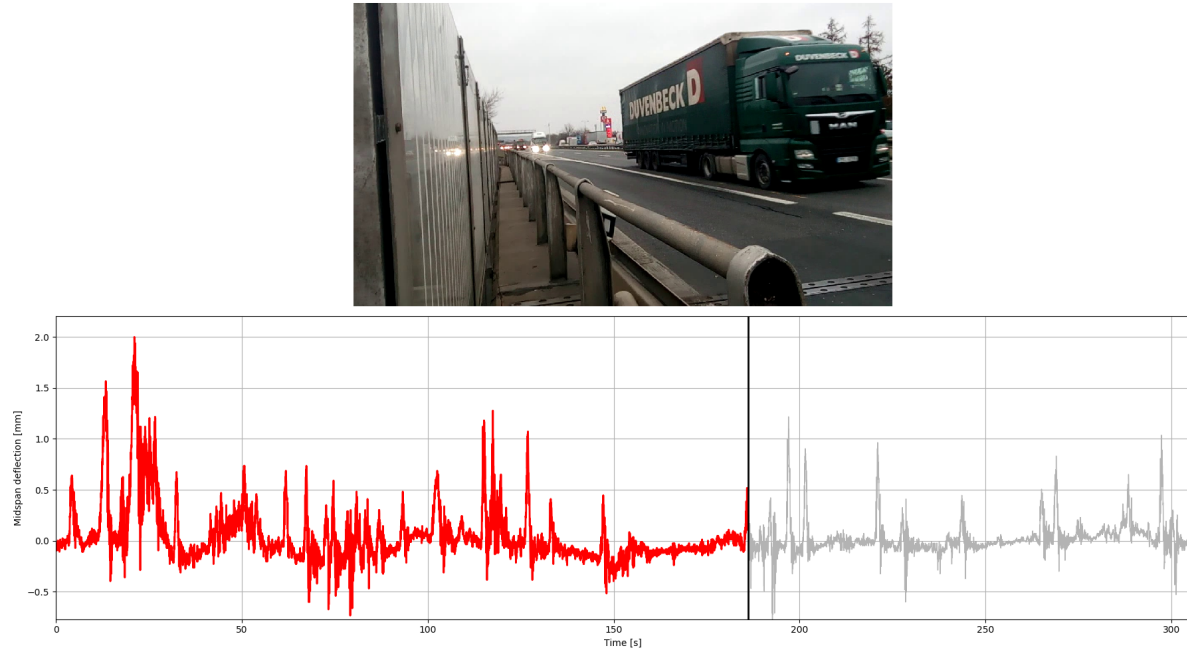


Figure 8.1: Continuous measurement of displacements on a highway bridge near Rudná u Prahy (frame from a video sequence presented as the measurement output).

⁶<https://youtu.be/54OEy3lDEl4>

Research outcomes

The applicability and usefulness of the research is demonstrated by the outcomes listed below.

Research outcome	Relationship to this thesis
<i>Software</i> RTCorr [185]	Implementation of the proposed algorithms for real-time DIC measurement in a single GUI-controlled tool
<i>Article #1</i> Antoš et al. [58]	Assessment of stochastic patterns for DIC
<i>Article #2</i> Antoš et al. [214]	Study on the practical use of the RTCorr software
<i>Article #3</i> Prošek et al. [215]	Long-term shrinkage measurement using the developed algorithm
<i>Article #4</i> Nežerka et al. [216]	Monitoring of shrinkage cracking using the developed algorithms

References

- [1] Hepi Hapsari Handayani, Yuwono, and M. Taufik. Preliminary study of bridge deformation monitoring using GPS and CRP (case study: Suramadu bridge). *Procedia Environmental Sciences*, 24:266–276, 2015. DOI: [10.1016/j.proenv.2015.03.035](https://doi.org/10.1016/j.proenv.2015.03.035).
- [2] Fanis Moschas and Stathis Stiros. Measurement of the dynamic displacements and of the modal frequencies of a short-span pedestrian bridge using GPS and an accelerometer. *Engineering Structures*, 33:10–17, 2011. DOI: [10.1016/j.engstruct.2010.09.013](https://doi.org/10.1016/j.engstruct.2010.09.013).
- [3] Moe M. S. Cheung and Ben Y. B. Chan. Operational requirements for long-span bridges under strong wind events. *Journal of Bridge Engineering*, 15:131–143, 2010. DOI: [10.1061/\(ASCE\)BE.1943-5592.0000044](https://doi.org/10.1061/(ASCE)BE.1943-5592.0000044).
- [4] Giulia Bossi, Luca Schenato, and Gianluca Marcato. Structural health monitoring of a road tunnel intersecting a large and active landslide. *Applied Sciences*, 7:1271, 2017. DOI: [10.3390/app7121271](https://doi.org/10.3390/app7121271).
- [5] Richard M. Iverson. Landslide triggering by rain infiltration. *Water Resources Research*, 36:1897–1910, 2000. DOI: [10.1029/2000WR900090](https://doi.org/10.1029/2000WR900090).
- [6] C. H. Jenkins, L. Kjerengtroen, and H. Oestensen. Sensitivity of parameter changes in structural damage detection. *Shock and Vibration*, 4:27–37, 1997. DOI: [10.1155/1997/807239](https://doi.org/10.1155/1997/807239).
- [7] Peter C. Chang, Alison Flatau, and S. C. Liu. Review paper: Health monitoring of civil infrastructure. *Structural Health Monitoring: An International Journal*, 2:257–267, 2003. DOI: [10.1177/1475921703036169](https://doi.org/10.1177/1475921703036169).
- [8] Corneliu Bob. About the causes of the koror bridge collapse. *Open Journal of Safety Science and Technology*, 04:119–126, 2014. DOI: [10.4236/ojsst.2014.42013](https://doi.org/10.4236/ojsst.2014.42013).
- [9] Claus-Peter Fritzen. Vibration-based techniques for structural health monitoring. In *Structural Health Monitoring*, pages 45–224. ISTE, 2006. DOI: [10.1002/9780470612071.ch2](https://doi.org/10.1002/9780470612071.ch2).
- [10] C. A. Sciammarella and F. M. Sciammarella. *Experimental Mechanics of Solids*. Wiley-Blackwell, 2012. DOI: [10.1002/9781119994091](https://doi.org/10.1002/9781119994091).
- [11] V. V. Shabarov. Wide-range strain-gauge device for static strain measurement. *Measurement Techniques*, 14:1851–1853, 1971. DOI: [10.1007/bf00994948](https://doi.org/10.1007/bf00994948).

- [12] Stefan Keil. *Technology and Practical Use of Strain Gages With Particular Consideration of Stress Analysis Using Strain Gages*. Wilhelm Ernst & Sohn, 2017. [DOI: 10.1002/9783433606667](https://doi.org/10.1002/9783433606667).
- [13] J. A. Coutts and A. J. Coombs. A method of installing a strain gauge. *Strain*, 5: 101–104, 1969. [DOI: 10.1111/j.1475-1305.1969.tb01588.x](https://doi.org/10.1111/j.1475-1305.1969.tb01588.x).
- [14] Yu. I. Koval and V. I. Boiko. Reliability of foil strain gauges in multiple cyclic deformations. *Strength of Materials*, 12:1047–1050, 1980. [DOI: 10.1007/bf00770540](https://doi.org/10.1007/bf00770540).
- [15] Sam-Deok Cho, Kwang-Wu Lee, Zhuang Li, and Uk-Gie Kim. Evaluation of reliability of strain gauge measurements for geosynthetics. *Journal of the Korean Geosynthetic Society*, 14:87–96, 2015. [DOI: 10.12814/jkgss.2015.14.4.087](https://doi.org/10.12814/jkgss.2015.14.4.087).
- [16] Majid Talebi, Christopher L. Meehan, and Tyler M. Poggigalle. Strain in a GRS bridge abutment: Strain gauge attachment techniques, performance and survivability during construction and operation. In *IFCEE 2018*. American Society of Civil Engineers, 2018. [DOI: 10.1061/9780784481608.025](https://doi.org/10.1061/9780784481608.025).
- [17] S. Zike and L P Mikkelsen. Correction of gauge factor for strain gauges used in polymer composite testing. *Experimental Mechanics*, 54:393–403, 2013. [DOI: 10.1007/s11340-013-9813-7](https://doi.org/10.1007/s11340-013-9813-7).
- [18] David S. Nyce. The LVDT. In *Linear Position Sensors*, pages 94–108. John Wiley & Sons, Inc., 2003. [DOI: 10.1002/0471474282.ch6](https://doi.org/10.1002/0471474282.ch6).
- [19] Hani H. Nassif, Mayrai Gindy, and Joe Davis. Comparison of laser doppler vibrometer with contact sensors for monitoring bridge deflection and vibration. *NDT & E International*, 38:213–218, 2005. [DOI: 10.1016/j.ndteint.2004.06.012](https://doi.org/10.1016/j.ndteint.2004.06.012).
- [20] Carmelo Gentile and Giulia Bernardini. An interferometric radar for non-contact measurement of deflections on civil engineering structures: laboratory and full-scale tests. *Structure and Infrastructure Engineering*, 6:521–534, 2009. [DOI: 10.1080/15732470903068557](https://doi.org/10.1080/15732470903068557).
- [21] G.A. Stephen, J.M.W. Brownjohn, and C.A. Taylor. Measurements of static and dynamic displacement from visual monitoring of the humber bridge. *Engineering Structures*, 15:197–208, 1993. [DOI: 10.1016/0141-0296\(93\)90054-8](https://doi.org/10.1016/0141-0296(93)90054-8).
- [22] J. J. Lee and M. Shinozuka. Real-time displacement measurement of a flexible bridge using digital image processing techniques. *Experimental Mechanics*, 46:105–114, 2006. [DOI: 10.1007/s11340-006-6124-2](https://doi.org/10.1007/s11340-006-6124-2).
- [23] Jong Jae Lee and Masanobu Shinozuka. A vision-based system for remote sensing of bridge displacement. *NDT & E International*, 39:425–431, 2006. [DOI: 10.1016/j.ndteint.2005.12.003](https://doi.org/10.1016/j.ndteint.2005.12.003).
- [24] M. Malesa, D. Szczepanek, M. Kujawińska, A. Świercz, and P. Kołakowski. Monitoring of civil engineering structures using digital image correlation technique. *EPJ Web of Conferences*, 6:31014, 2010. [DOI: 10.1051/epjconf/20100631014](https://doi.org/10.1051/epjconf/20100631014).

- [25] E Bell, J Peddle, and A Goudreau. Bridge condition assessment using digital image correlation and structural modeling. In *Bridge Maintenance, Safety, Management, Resilience and Sustainability*, pages 330–337. CRC Press, 2012.
[DOI: 10.1201/b12352-41](https://doi.org/10.1201/b12352-41).
- [26] David V. Jáuregui, Kenneth R. White, Clinton B. Woodward, and Kenneth R. Leitch. Noncontact photogrammetric measurement of vertical bridge deflection. *Journal of Bridge Engineering*, 8:212–222, 2003. [DOI: 10.1061/\(asce\)1084-0702\(2003\)8:4\(212\)](https://doi.org/10.1061/(asce)1084-0702(2003)8:4(212)).
- [27] Wonjo Jung, Do Hyoung Shin, SungKwon Woo, Won jin Park, and Sangbin Kim. Hibrid approach of cameras and GPS for displacement measurements of super long-sapn bridges. In *28th International Symposium on Automation and Robotics in Construction (ISARC 2011)*. International Association for Automation and Robotics in Construction (IAARC), 2011. [DOI: 10.22260/isarc2011/0190](https://doi.org/10.22260/isarc2011/0190).
- [28] J.N. Périé, S. Calloch, C. Cluzel, and F. Hild. Analysis of a multiaxial test on a c/c composite by using digital image correlation and a damage model. *Experimental Mechanics*, 42(3):318–328, sep 2002. [DOI: 10.1007/bf02410989](https://doi.org/10.1007/bf02410989).
- [29] K. H Laermann, editor. *Optical Methods in Experimental Solid Mechanics*. Springer Nature, 2000. [DOI: 10.1007/978-3-7091-2586-1](https://doi.org/10.1007/978-3-7091-2586-1).
- [30] Victor Giurgiutiu and JingJing Bao. Embedded-ultrasonics structural radar for in situ structural health monitoring of thin-wall structures. *Structural Health Monitoring: An International Journal*, 3:121–140, 2004. [DOI: 10.1177/1475921704042697](https://doi.org/10.1177/1475921704042697).
- [31] Carmelo Gentile and Giulia Bernardini. Radar-based measurement of deflections on bridges and large structures. *European Journal of Environmental and Civil engineering*, 14:495–516, 2010. [DOI: 10.3166/ejce.14.495-516](https://doi.org/10.3166/ejce.14.495-516).
- [32] M. Figurski, M. Gałuszkiewicz, and M. Wrona. A bridge deflection monitoring with GPS. *Artificial Satellites*, 42:229–238, 2007. [DOI: 10.2478/v10018-008-0010-3](https://doi.org/10.2478/v10018-008-0010-3).
- [33] Fabio Casciati and Clemente Fuggini. Monitoring a steel building using GPS sensors. *Smart Structures and Systems*, 7:349–363, 2011. [DOI: 10.12989/sss.2011.7.5.349](https://doi.org/10.12989/sss.2011.7.5.349).
- [34] Mosbeh Kaloop, Emad Elbeltagi, Jong Hu, and Ahmed Elrefai. Recent advances of structures monitoring and evaluation using GPS-time series monitoring systems: A review. *ISPRS International Journal of Geo-Information*, 6:382, 2017.
[DOI: 10.3390/ijgi6120382](https://doi.org/10.3390/ijgi6120382).
- [35] Claus P. Keferstein and Michael Marxer. Testing bench for laser triangulation sensors. *Sensor Review*, 18:183–187, 1998. [DOI: 10.1108/02602289810226408](https://doi.org/10.1108/02602289810226408).
- [36] Armin B. Mehrabi. In-service evaluation of cable-stayed bridges, overview of available methods and findings. *Journal of Bridge Engineering*, 11:716–724, 2006.
[DOI: 10.1061/\(asce\)1084-0702\(2006\)11:6\(716\)](https://doi.org/10.1061/(asce)1084-0702(2006)11:6(716)).

- [37] Filip Dvoracek. LONG RANGE DISTANCE MEASUREMENT WITH LEICA AT401 LASER TRACKER. In *16th International Multidisciplinary Scientific GeoConference SGEM2016, Informatics, Geoinformatics and Remote Sensing*. Stef92 Technology, 2016. [DOI: 10.5593/sgem2016/b22/s09.051](https://doi.org/10.5593/sgem2016/b22/s09.051).
- [38] Vlatko Brčić. Basic concepts in holography and hologram interferometry. In *Application of Holography and Hologram Interferometry to Photoelasticity*, pages 12–18. Springer Vienna, 1974. [DOI: 10.1007/978-3-7091-2646-2_2](https://doi.org/10.1007/978-3-7091-2646-2_2).
- [39] Pascal Picart. Evaluation of phase shifting speckle interferometry accuracy. In *Interferometry in Speckle Light*, pages 431–438. Springer Berlin Heidelberg, 2000. [DOI: 10.1007/978-3-642-57323-1_53](https://doi.org/10.1007/978-3-642-57323-1_53).
- [40] Daniel Post, Bongtae Han, and Peter G. Ifju. Moiré methods for engineering and science — moiré interferometry and shadow moiré. In *Topics in Applied Physics*, pages 151–196. Springer Berlin Heidelberg, 2000. [DOI: 10.1007/3-540-48800-6_5](https://doi.org/10.1007/3-540-48800-6_5).
- [41] H. Schreier, J. Orteu, and M. Sutton. *Image Correlation for Shape, Motion and Deformation Measurements*. Springer Nature, 2009. [DOI: 10.1007/978-0-387-78747-3](https://doi.org/10.1007/978-0-387-78747-3).
- [42] J. S. Sirkis and T. J. Lim. Displacement and strain measurement with automated grid methods. *Experimental Mechanics*, 31:382–388, 1991. [DOI: 10.1007/bf02325997](https://doi.org/10.1007/bf02325997).
- [43] I. Yamaguchi. A laser speckle strain gauge. *Journal of Physics E: Scientific Instruments*, 14:1270, 1981. [DOI: 10.1088/0022-3735/14/11/012](https://doi.org/10.1088/0022-3735/14/11/012).
- [44] W. H. Peters and W. F. Ranson. Digital imaging techniques in experimental stress analysis. *Optical Engineering*, 21:427–431, 1982. [DOI: 10.1117/12.7972925](https://doi.org/10.1117/12.7972925).
- [45] M.A. Sutton, J.H. Yan, V. Tiwari, H.W. Schreier, and J.J. Orteu. The effect of out-of-plane motion on 2D and 3D digital image correlation measurements. *Optics and Lasers in Engineering*, 46:746–757, 2008. [DOI: 10.1016/j.optlaseng.2008.05.005](https://doi.org/10.1016/j.optlaseng.2008.05.005).
- [46] Marco Palanca, Gianluca Tozzi, and Luca Cristofolini. The use of digital image correlation in the biomechanical area: a review. *International Biomechanics*, 3:1–21, 2015. [DOI: 10.1080/23335432.2015.1117395](https://doi.org/10.1080/23335432.2015.1117395).
- [47] A. H. Salmanpour and N. Mojsilović. Application of Digital Image Correlation for strain measurements of large masonry walls. *APCOM & ISCM*, 2013.
- [48] S. H. Tung, M. H. Shih, and W. P. Sung. Development of digital image correlation method to analyse crack variations of masonry walls. *Sadhana*, 33:767–779, 2008.
- [49] Christopher Niegrecki, Peter Avitabile, Christopher Warren, Pawan Pingle, Mark Helfrick, and E. P. Tomasini. A review of digital image correlation applied to structural dynamics. *AIP*, 2010. [DOI: 10.1063/1.3455461](https://doi.org/10.1063/1.3455461).
- [50] S. Russev, G. Tsutsumanova, S. Angelov, and K. Bachev. An electron beam lithography and digital image acquisition system for scanning electron microscopes. *Journal of Microscopy*, 226(1):64–70, 2007. [DOI: 10.1111/j.1365-2818.2007.01753.x](https://doi.org/10.1111/j.1365-2818.2007.01753.x).

- [51] C.E. Sloane and M.J. Mills. Analysis of strain localization at high angle grain boundaries during creep of a polycrystalline superalloy using SEM-based digital image correlation. *Microscopy and Microanalysis*, 22:2018–2019, 2016. DOI: [10.1017/s143192761601093x](https://doi.org/10.1017/s143192761601093x).
- [52] C. Popescu, G. Sas, and B. Arntsen. Structural health monitoring of a buttress dam using digital image correlation. In *Sustainable and Safe Dams Around the World*, pages 1671–1680. CRC Press, 2019. DOI: [10.1201/9780429319778-151](https://doi.org/10.1201/9780429319778-151).
- [53] A. Hoag, N. Hoult, A. Take, and H. Le. Monitoring of rail bridge displacements using digital image correlation. In *Structural Health Monitoring 2015*. Destech Publications, 2015. DOI: [10.12783/shm2015/52](https://doi.org/10.12783/shm2015/52).
- [54] P. Wang, F. Pierron, and O. T. Thomsen. Identification of material parameters of PVC foams using digital image correlation and the virtual fields method. *Experimental Mechanics*, 53:1001–1015, 2012. DOI: [10.1007/s11340-012-9703-4](https://doi.org/10.1007/s11340-012-9703-4).
- [55] Roberto Fedele and Roberta Santoro. Extended identification of mechanical parameters and boundary conditions by digital image correlation. *Procedia IUTAM*, 4:40–47, 2012. DOI: [10.1016/j.piutam.2012.05.005](https://doi.org/10.1016/j.piutam.2012.05.005).
- [56] B. Thimm, J. Steden, M. Reuber, and H.-J. Christ. Using digital image correlation measurements for the inverse identification of constitutive material parameters applied in metal cutting simulations. *Procedia CIRP*, 82:95–100, 2019. DOI: [10.1016/j.procir.2019.04.156](https://doi.org/10.1016/j.procir.2019.04.156).
- [57] V. Nežerka, J. Antoš, T. Sajdlová, and P. Tesárek. Use of open source DIC tools for analysis of multiple cracking in fiber-reinforced concrete. *Applied Mechanics and Materials*, 827:336–339, 2016. DOI: [10.4028/www.scientific.net/amm.827.336](https://doi.org/10.4028/www.scientific.net/amm.827.336).
- [58] Jakub Antoš, Václav Nežerka, and Michael Somr. Assessment of 2D-DIC stochastic patterns. *Acta Polytechnica CTU Proceedings*, 13:1–10, 2017. DOI: [10.14311/app.2017.13.0001](https://doi.org/10.14311/app.2017.13.0001).
- [59] B. Pan, H. Xie, and Z. Wang. Equivalence of digital image correlation criteria for pattern matching. *Applied Optics*, 49:5501–5509, 2010.
- [60] A. W. Gruen. Adaptive least squares correlation: a powerful image matching technique. *South African Journal of Photography, Remote Sensing and Cartography*, 14:175–187, 1985.
- [61] Y. Altunbasak, R. M. Mersereau, and A. J. Patti. A fast parametric motion estimation algorithm with illumination and lens distortion correction. *IEEE Transactions on Image Processing*, 12:395–408, 2003. DOI: [10.1109/tip.2003.809012](https://doi.org/10.1109/tip.2003.809012).
- [62] B. Pan, A. Asundi, H. Xie, and J. Gao. Digital image correlation using iterative least squares and pointwise least squares for displacement field and strain field measurements. *Optics and Lasers in Engineering*, 47:865–874, 2009. DOI: [10.1016/j.optlaseng.2008.10.014](https://doi.org/10.1016/j.optlaseng.2008.10.014).

- [63] B. Pan, Z. Wang, and H. Xie. Generalized spatial-gradient-based digital image correlation for displacement and shape measurement with subpixel accuracy. *The Journal of Strain Analysis for Engineering Design*, 44:659–669, 2009. [DOI: 10.1243/03093247jsa546](https://doi.org/10.1243/03093247jsa546).
- [64] K. Triconnet, K. Derrien, F. Hild, and D. Baptiste. Parameter choice for optimized digital image correlation. *Optics and Lasers in Engineering*, 47:728–737, 2009. [DOI: 10.1016/j.optlaseng.2008.10.015](https://doi.org/10.1016/j.optlaseng.2008.10.015).
- [65] Phillip L. Reu. A realistic error budget for two dimension digital image correlation. In *Advancement of Optical Methods in Experimental Mechanics, Volume 3*, pages 189–193. 2016. [DOI: 10.1007/978-3-319-22446-6_24](https://doi.org/10.1007/978-3-319-22446-6_24).
- [66] Zhenxing Hu, Huimin Xie, Jian Lu, Tao Hua, and Jianguo Zhu. Study of the performance of different subpixel image correlation methods in 3d digital image correlation. *Applied Optics*, 49:4044–4052, 2010. [DOI: 10.1364/ao.49.004044](https://doi.org/10.1364/ao.49.004044).
- [67] Zhenxing Hu, Huimin Xie, Jian Lu, Huaixi Wang, and Jianguo Zhu. Error evaluation technique for three-dimensional digital image correlation. *Applied Optics*, 50: 6239–6248, 2011. [DOI: 10.1364/ao.50.006239](https://doi.org/10.1364/ao.50.006239).
- [68] Thorsten Siebert, Thomas Becker, Karsten Spiltthof, Isabell Neumann, and Rene Krupka. Error estimations in digital image correlation technique. *Applied Mechanics and Materials*, 7–8:265–270, 2007. [DOI: 10.4028/www.scientific.net/amm.7-8.265](https://doi.org/10.4028/www.scientific.net/amm.7-8.265).
- [69] H. A. Bruck, S. R. McNeill, M. A. Sutton, and W. H. Peters. Digital image correlation using newton-raphson method of partial differential correction. *Experimental Mechanics*, 29:261–267, 1989. [DOI: 10.1007/bf02321405](https://doi.org/10.1007/bf02321405).
- [70] Jun Zhang, Guanchang Jin, Shaopeng Ma, and Libo Meng. Application of an improved subpixel registration algorithm on digital speckle correlation measurement. *Optics & Laser Technology*, 35:533–542, 2003. [DOI: 10.1016/s0030-3992\(03\)00069-0](https://doi.org/10.1016/s0030-3992(03)00069-0).
- [71] B. Pan, K. Qian, H. Xie, and A. Asundi. Two-dimensional digital image correlation for in-plane displacement and strain measurement: a review. *Measurement Science and Technology*, 20:062001, 2009. [DOI: 10.1088/0957-0233/20/6/062001](https://doi.org/10.1088/0957-0233/20/6/062001).
- [72] B. Pan, K. Li, and W. Tong. Fast, robust and accurate Digital Image Correlation calculation without redundant computations. *Experimental Mechanics*, 53:1277–1289, 2013.
- [73] Yaofeng Sun, John H. L. Pang, Chee Khuen Wong, and Fei Su. Finite element formulation for a digital image correlation method. *Applied Optics*, 44:7357–7369, 2005. [DOI: 10.1364/ao.44.007357](https://doi.org/10.1364/ao.44.007357).
- [74] G. Besnard, F. Hild, and S. Roux. “finite-element” displacement fields analysis from digital images: Application to portevin–le châtelier bands. *Experimental Mechanics*, 46:789–803, 2006. [DOI: 10.1007/s11340-006-9824-8](https://doi.org/10.1007/s11340-006-9824-8).

- [75] Shaopeng Ma, Zilong Zhao, and Xian Wang. Mesh-based digital image correlation method using higher order isoparametric elements. *The Journal of Strain Analysis for Engineering Design*, 47:163–175, 2012. DOI: [10.1177/0309324712437488](https://doi.org/10.1177/0309324712437488).
- [76] J. Réthoré, T. Elguedj, P. Simon, and M. Coret. On the use of NURBS functions for displacement derivatives measurement by digital image correlation. *Experimental Mechanics*, 50:1099–1116, 2009. DOI: [10.1007/s11340-009-9304-z](https://doi.org/10.1007/s11340-009-9304-z).
- [77] Gilles Besnard, Hugo Leclerc, François Hild, Stéphane Roux, and Nicolas Swiergiel. Analysis of image series through global digital image correlation. *The Journal of Strain Analysis for Engineering Design*, 47:214–228, 2012. DOI: [10.1177/0309324712441435](https://doi.org/10.1177/0309324712441435).
- [78] L. Wittevrongel, P. Lava, S. V. Lomov, and D. Debruyne. A self adaptive global digital image correlation algorithm. *Experimental Mechanics*, 55:361–378, 2014. DOI: [10.1007/s11340-014-9946-3](https://doi.org/10.1007/s11340-014-9946-3).
- [79] Bo Wang and Bing Pan. Subset-based local vs. finite element-based global digital image correlation: A comparison study. *Theoretical and Applied Mechanics Letters*, 6: 200–208, 2016. DOI: [10.1016/j.taml.2016.08.003](https://doi.org/10.1016/j.taml.2016.08.003).
- [80] P. Bing, X. Hui-min, X. Bo-qin, and D. Fu-long. Performance of sub-pixel registration algorithms in digital image correlation. *Measurement Science and Technology*, 17: 1615–1621, 2006. DOI: [10.1088/0957-0233/17/6/045](https://doi.org/10.1088/0957-0233/17/6/045).
- [81] J. Blaber, B. Adair, and A. Antouniou. Ncorr: Open-source 2d digital image correlation matlab software. *Experimental Mechanics*, 55:1105–1122, 2015. DOI: [10.1007/s11340-015-0009-1](https://doi.org/10.1007/s11340-015-0009-1).
- [82] J. Blaber. Ncorr digital image correlation software algorithms, <http://www.ncorr.com/index.php/dic-algorithms>. *Georgia Institute of Technology*, 2014.
- [83] Bing Pan, Huimin Xie, Jianxin Gao, and Anand Asundi. Improved speckle projection profilometry for out-of-plane shape measurement. *Applied Optics*, 47:5527..5542, 2008. DOI: [10.1364/ao.47.005527](https://doi.org/10.1364/ao.47.005527).
- [84] D. Lecompte, A. Smits, Bossuyt S., H. Sol, J. Vantomme, D. Van Hemelrijck, and A.M. Habraken. Quality assessment of speckle patterns for digital image correlation. *Optics and Lasers in Engineering*, 44:1132–1145, 2006.
- [85] B. Pan, H. Xie, Z. Wang, K. Qian, and Z. Wang. Study on subset size selection in digital image correlation for speckle patterns. *Optics Express*, 16:7037, 2008. DOI: [10.1364/oe.16.007037](https://doi.org/10.1364/oe.16.007037).
- [86] B. Pan, Z. Lu, and H. Xie. Mean intensity gradient: An Effective global parameter for quality assessment of the speckle patterns used in digital image correlation. *Optics and Lasers in Engineering*, 48:469–477, 2010.
- [87] J. Blaber. Ncorr digital image correlation software, <http://www.ncorr.com/>. *Georgia Institute of Technology*, 2014.

- [88] Markus J. Hochrainer. A cost effective DIC system for measuring structural vibrations. In *Rotating Machinery, Hybrid Test Methods, Vibro-Acoustics & Laser Vibrometry, Volume 8*, pages 139–146. Springer International Publishing, 2016.
[DOI: 10.1007/978-3-319-30084-9_12](https://doi.org/10.1007/978-3-319-30084-9_12).
- [89] Simon Baker and Iain Matthews. Lucas-Kanade 20 Years On: A Unifying Framework. *International Journal of Computer Vision*, 56:221–255, 2004.
[DOI: 10.1023/b:visi.0000011205.11775.fd](https://doi.org/10.1023/b:visi.0000011205.11775.fd).
- [90] G. Tao and Z. Xia. A non-contact real-time strain measurement and control system for multiaxial cyclic / fatigue tests of polymer materials by digital image correlation method. *Polymer Testing*, 24:844–855, 2005.
- [91] Y. H. Huang, L. Liu, T. W. Yeung, and Y. Y. Hung. Real-time monitoring of clamping force of a bolted joint by use of automatic digital image correlation. *Optics & Laser Technology*, 41:408–414, 2009. [DOI: 10.1016/j.optlastec.2008.08.010](https://doi.org/10.1016/j.optlastec.2008.08.010).
- [92] J. Le Flohic, V. Parpoil, S. Bouissou, M. Poncelet, and H. Leclerc. A 3d displacement control by digital image correlation for the multiaxial testing of materials with a stewart platform. *Experimental Mechanics*, 2014. [DOI: 10.1007/s11340-013-9837-z](https://doi.org/10.1007/s11340-013-9837-z).
- [93] T. Dallej, N. Andreff, Y. Mezouar, and P. Martinet. 3d pose visual servoing relieves parallel robot control from joint sensing. In *2006 IEEE/RSJ International Conference on Intelligent Robots and Systems*. Institute of Electrical and Electronics Engineers (IEEE), 2006. [DOI: 10.1109/iros.2006.281959](https://doi.org/10.1109/iros.2006.281959).
- [94] X. Fayolle, S. Calloch, and F. Hild. Controlling testing machines with digital image correlation. *Experimental Techniques*, 31:57–63, 2007.
[DOI: 10.1111/j.1747-1567.2007.00152.x](https://doi.org/10.1111/j.1747-1567.2007.00152.x).
- [95] R. Wu, C. Kong, K. Li, and D. Zhang. Real-time digital image correlation for dynamic strain measurement. *Experimental Mechanics*, 56:833–843, 2016.
[DOI: 10.1007/s11340-016-0133-6](https://doi.org/10.1007/s11340-016-0133-6).
- [96] Pakize Erdoganmus. Introductory chapter: Swarm intelligence and particle swarm optimization. In *Particle Swarm Optimization with Applications*. InTech, may 2018.
[DOI: 10.5772/intechopen.74076](https://doi.org/10.5772/intechopen.74076).
- [97] Lurng-Kuo Liu and E. Feig. A block-based gradient descent search algorithm for block motion estimation in video coding. *IEEE Transactions on Circuits and Systems for Video Technology*, 6:419–422, 1996. [DOI: 10.1109/76.510936](https://doi.org/10.1109/76.510936).
- [98] J. B. Xu, L. M. Po, and Ch. K. Cheung. Adaptive motion tracking block matching algorithms for video coding. *IEEE Transactions on Circuits and Systems for Video Technology*, 9:1025–1029, 1999. [DOI: 10.1109/76.795056](https://doi.org/10.1109/76.795056).
- [99] R. E. Jacobson, S. F. Ray, G. G. Attridge, and N. R. Axford. *The Manual of Photography*. Reed Educational and Professional Publishing Ltd, 2000. ISBN 0-240-51574-9.

- [100] S. N. Bezdidko. Orthogonal aberrations: theory, methods, and practical applications in computational optics. *Journal of Optical Technology*, 83:351, 2016.
[DOI: 10.1364/jot.83.000351](https://doi.org/10.1364/jot.83.000351).
- [101] Jie Jiang. Distortion correction for a wide-angle lens based on real-time digital image processing. *Optical Engineering*, 42:2029, 2003. [DOI: 10.1117/1.1580155](https://doi.org/10.1117/1.1580155).
- [102] Saturu Yoneyama. Lens distortion correction for digital image correlation by measuring rigid body displacement. *Optical Engineering*, 45:023602, 2006.
[DOI: 10.1117/1.2168411](https://doi.org/10.1117/1.2168411).
- [103] Qiucheng Sun, Yueqian Hou, and Jian Chen. Lens distortion correction for improving measurement accuracy of digital image correlation. *Optik*, 126:3153–3157, 2015.
[DOI: 10.1016/j.ijleo.2015.07.068](https://doi.org/10.1016/j.ijleo.2015.07.068).
- [104] H. W. Schreier, D. Garcia, and M. A. Sutton. Advances in light microscope stereo vision. *Experimental Mechanics*, 44:278–288, 2004. [DOI: 10.1007/bf02427894](https://doi.org/10.1007/bf02427894).
- [105] V. Tiwari, M. A. Sutton, and S. R. McNeill. Assessment of high speed imaging systems for 2d and 3d deformation measurements: Methodology development and validation. *Experimental Mechanics*, 47:561–579, 2007. [DOI: 10.1007/s11340-006-9011-y](https://doi.org/10.1007/s11340-006-9011-y).
- [106] H. Haddadi and S. Belhabib. Use of rigid-body motion for the investigation and estimation of the measurement errors related to digital image correlation technique. *Optics and Lasers in Engineering*, 46:185–196, 2008.
[DOI: 10.1016/j.optlaseng.2007.05.008](https://doi.org/10.1016/j.optlaseng.2007.05.008).
- [107] R. Tsai. A versatile camera calibration technique for high-accuracy 3d machine vision metrology using off-the-shelf TV cameras and lenses. *IEEE Journal on Robotics and Automation*, 3:323–344, 1987. [DOI: 10.1109/jra.1987.1087109](https://doi.org/10.1109/jra.1987.1087109).
- [108] J. Weng, P. Cohen, and M. Herniou. Camera calibration with distortion models and accuracy evaluation. *IEEE Transactions on Pattern Analysis and Machine Intelligence*, 14:965–980, 1992. [DOI: 10.1109/34.159901](https://doi.org/10.1109/34.159901).
- [109] Z. Zhang. A flexible new technique for camera calibration. *IEEE Transactions on Pattern Analysis and Machine Intelligence*, 22:1330–1334, 2000.
[DOI: 10.1109/34.888718](https://doi.org/10.1109/34.888718).
- [110] B. Pan, L. Yu, D. Wu, and L. Tang. Systematic errors in two-dimensional digital image correlation due to lens distortion. *Optics and Lasers in Engineering*, 51:140–147, 2013.
[DOI: 10.1016/j.optlaseng.2012.08.012](https://doi.org/10.1016/j.optlaseng.2012.08.012).
- [111] Rory Bigger, Benoît Blaysat, Christofer Boo, Manuel Grewer, Jun Hu, Amanda Jones, Markus Klein, Kavesary Raghavan, Phillip Reu, Timothy Schmidt, Thorsten Siebert, Micah Simenson, Daniel Turner, Alessandro Vieira, and Thorsten Weikert. A good practices guide for digital image correlation. Technical report, 2018.
- [112] L. Wittevrongel, M. Badaloni, R. Balcaen, P. Lava, and D. Debruyne. Evaluation of methodologies for compensation of out of plane motions in a 2D digital image correlation setup. *Strain*, 51:357–369, 2015. [DOI: 10.1111/str.12146](https://doi.org/10.1111/str.12146).

- [113] Robert Whitrow. Image file formats. In *OpenGL Graphics Through Applications*, pages 39–59. Springer London. [DOI: 10.1007/978-1-84800-023-0-2](https://doi.org/10.1007/978-1-84800-023-0-2).
- [114] Nanette Salvaggio. *Basic Photographic Materials and Processes*. Routledge, 2013. [DOI: 10.4324/9780080927664](https://doi.org/10.4324/9780080927664).
- [115] Weidong Kou. Principles of digital image compression. In *Digital Image Compression*, pages 1–8. Springer US, 1995. [DOI: 10.1007/978-1-4757-2361-8_1](https://doi.org/10.1007/978-1-4757-2361-8_1).
- [116] Rohit M. Thanki and Ashish Kothari. *Hybrid and Advanced Compression Techniques for Medical Images*. Springer International Publishing, 2019. [DOI: 10.1007/978-3-030-12575-2](https://doi.org/10.1007/978-3-030-12575-2).
- [117] L.K. Tan. Image file formats. *Biomedical Imaging and Intervention Journal*, 2:1–7, 2006. [DOI: 10.2349/bij.2.1.e6](https://doi.org/10.2349/bij.2.1.e6).
- [118] Xiangui Kang, Xianyu Xu, Anjie Peng, and Wenjun Zeng. Scalable lossy compression for pixel-value encrypted images. In *2012 Data Compression Conference*. IEEE, 2012. [DOI: 10.1109/dcc.2012.55](https://doi.org/10.1109/dcc.2012.55).
- [119] Y. Bentoutou, N. Taleb, K. Kpalma, and J. Ronsin. An automatic image registration for applications in remote sensing. *IEEE Transactions on Geoscience and Remote Sensing*, 43:2127–2137, 2005. [DOI: 10.1109/tgrs.2005.853187](https://doi.org/10.1109/tgrs.2005.853187).
- [120] Jordi Ingla, Vincent Muron, Damien Pichard, and Thomas Feuvrier. Analysis of artifacts in subpixel remote sensing image registration. *IEEE Transactions on Geoscience and Remote Sensing*, 45:254–264, 2007. [DOI: 10.1109/tgrs.2006.882262](https://doi.org/10.1109/tgrs.2006.882262).
- [121] Kun Yang, Anning Pan, Yang Yang, Su Zhang, Sim Ong, and Haolin Tang. Remote sensing image registration using multiple image features. *Remote Sensing*, 9:581, 2017. [DOI: 10.3390/rs9060581](https://doi.org/10.3390/rs9060581).
- [122] C. Studholme, D.L.G. Hill, and D.J. Hawkes. Automated 3-d registration of MR and CT images of the head. *Medical Image Analysis*, 1:163–175, 1996. [DOI: 10.1016/s1361-8415\(96\)80011-9](https://doi.org/10.1016/s1361-8415(96)80011-9).
- [123] Wolfgang Wein, Shelby Brunke, Ali Khamene, Matthew R. Callstrom, and Nassir Navab. Automatic CT-ultrasound registration for diagnostic imaging and image-guided intervention. *Medical Image Analysis*, 12:577–585, 2008. [DOI: 10.1016/j.media.2008.06.006](https://doi.org/10.1016/j.media.2008.06.006).
- [124] Sascha E.A. Muenzing, Bram van Ginneken, Keelin Murphy, and Josien P.W. Pluim. Supervised quality assessment of medical image registration: Application to intra-patient CT lung registration. *Medical Image Analysis*, 16:1521–1531, 2012. [DOI: 10.1016/j.media.2012.06.010](https://doi.org/10.1016/j.media.2012.06.010).
- [125] Vladlena Gorbunova, Jon Sporring, Pechin Lo, Martine Loeve, Harm A. Tiddens, Mads Nielsen, Asger Dirksen, and Marleen de Bruijne. Mass preserving image registration for lung CT. *Medical Image Analysis*, 16:786–795, 2012. [DOI: 10.1016/j.media.2011.11.001](https://doi.org/10.1016/j.media.2011.11.001).

- [126] Pattathal V. Arun and Sunil K. Katiyar. A CNN based hybrid approach towards automatic image registration. *Geodesy and Cartography*, 62:33–49, 2013.
[DOI: 10.2478/geocart-2013-0005](https://doi.org/10.2478/geocart-2013-0005).
- [127] Lance M. Kaplan and Nasser M. Nasrabadi. Block wiener-based image registration for moving target indication. *Image and Vision Computing*, 27:694–703, 2009.
[DOI: 10.1016/j.imavis.2008.07.008](https://doi.org/10.1016/j.imavis.2008.07.008).
- [128] A. Seginer. Rigid-body point-based registration: The distribution of the target registration error when the fiducial registration errors are given. *Medical Image Analysis*, 15:397–413, 2011. [DOI: 10.1016/j.media.2011.01.001](https://doi.org/10.1016/j.media.2011.01.001).
- [129] Scott Robertson, Elisabeth Weiss, and Geoffrey D. Hugo. Deformable mesh registration for the validation of automatic target localization algorithms. *Medical Physics*, 40:071721, 2013. [DOI: 10.1111/1.4811105](https://doi.org/10.1111/1.4811105).
- [130] Pierantonio Facco, Andrea Masiero, and Alessandro Beghi. Advances on multivariate image analysis for product quality monitoring. *Journal of Process Control*, 23:89–98, 2013. [DOI: 10.1016/j.jprocont.2012.08.017](https://doi.org/10.1016/j.jprocont.2012.08.017).
- [131] D. I. Barnea and H. F. Silverman. A class of algorithms for fast digital image registration. *IEEE Transactions on Computers*, C-21:179–186, 1972.
[DOI: 10.1109/tc.1972.5008923](https://doi.org/10.1109/tc.1972.5008923).
- [132] C. D. Kuglin and D. C. Hines. The phase correlation image alignment method. In *Proc. Int. Conference Cybernetics Society*, pages 163–165, 1975.
- [133] Joseph L. Horner and Peter D. Gianino. Phase-only matched filtering. *Applied Optics*, 23:812, 1984. [DOI: 10.1364/ao.23.000812](https://doi.org/10.1364/ao.23.000812).
- [134] E. De Castro and C. Morandi. Registration of translated and rotated images using finite fourier transforms. *IEEE Transactions on Pattern Analysis and Machine Intelligence*, 9:700–703, 1987. [DOI: 10.1109/tpami.1987.4767966](https://doi.org/10.1109/tpami.1987.4767966).
- [135] *Computational Vision*. Elsevier, 1990. [DOI: 10.1016/c2009-0-21627-8](https://doi.org/10.1016/c2009-0-21627-8). URL <https://doi.org/10.1016/c2009-0-21627-8>.
- [136] A.Y.M. Ontman and G.J. Shiflet. Application of artificial neural networks for feature recognition in image registration. *Journal of Microscopy*, 246:20–32, 2011.
[DOI: 10.1111/j.1365-2818.2011.03580.x](https://doi.org/10.1111/j.1365-2818.2011.03580.x).
- [137] Murat D. Aykin and Shahriar Negahdaripour. On feature matching and image registration for two-dimensional forward-scan sonar imaging. *Journal of Field Robotics*, 30:602–623, 2013. [DOI: 10.1002/rob.21461](https://doi.org/10.1002/rob.21461).
- [138] Xiao-Hua Shu and Zhen-Kang Shen. Automatic image registration based on feature region. *Journal of Computer Applications*, 32:759–761, 2013.
[DOI: 10.3724/sp.j.1087.2012.00759](https://doi.org/10.3724/sp.j.1087.2012.00759).

- [139] B.K. Ghaffary and A.A. Sawchuk. A survey of new techniques for image registration and mapping. *Proceedings of the SPIE: Applications of Digital Image Processing*, 432: 222–239, 1983. DOI: [10.1117/12.936668](https://doi.org/10.1117/12.936668).
- [140] Lisa Gottesfeld Brown. A survey of image registration techniques. *ACM Computing Surveys*, 24:325–376, 1992. DOI: [10.1145/146370.146374](https://doi.org/10.1145/146370.146374).
- [141] Barbara Zitová and Jan Flusser. Image registration methods: a survey. *Image and Vision Computing*, 21:977–1000, 2003. DOI: [10.1016/s0262-8856\(03\)00137-9](https://doi.org/10.1016/s0262-8856(03)00137-9).
- [142] Jinchang Ren, Jianmin Jiang, and Theodore Vlachos. High-accuracy sub-pixel motion estimation from noisy images in fourier domain. *IEEE Transactions on Image Processing*, 19:1379–1384, 2010. DOI: [10.1109/tip.2009.2039056](https://doi.org/10.1109/tip.2009.2039056).
- [143] William J. Scharpf. Global registration and moving objects detection in noisy airborne image sequences. *Optical Engineering*, 49:127005, 2010. DOI: [10.1117/1.3520057](https://doi.org/10.1117/1.3520057).
- [144] V. Čížek. *Diskrétní Fourierova transformace a její použití*. Matematický seminář SNTL. SNTL, 1981.
- [145] Henri J. Nussbaumer. *Fast Fourier Transform and Convolution Algorithms*. Springer Berlin Heidelberg, 1982. DOI: [10.1007/978-3-642-81897-4](https://doi.org/10.1007/978-3-642-81897-4).
- [146] Charles Van Loan. *Computational Frameworks for the Fast Fourier Transform*. Society for Industrial and Applied Mathematics, jan 1992. DOI: [10.1137/1.9781611970999](https://doi.org/10.1137/1.9781611970999).
- [147] M. Heideman, D. Johnson, and C. Burrus. Gauss and the history of the fast fourier transform. *IEEE ASSP Magazine*, 1:14–21, 1984. DOI: [10.1109/massp.1984.1162257](https://doi.org/10.1109/massp.1984.1162257).
- [148] V. Bezdová. *Dvojrozměrná diskrétní Fourierova transformace a její použití: pro posl. fak. přírodrověd. Teorie a obecné užití*. Number díl 1. SPN, 1988.
- [149] Eric Stade. *Fourier Analysis*. John Wiley & Sons, Inc., 2005.
DOI: [10.1002/9781118165508](https://doi.org/10.1002/9781118165508).
- [150] Kedar Khare. *Fourier Optics and Computational Imaging*. John Wiley & Sons, Ltd, 2015. DOI: [10.1002/9781118900352](https://doi.org/10.1002/9781118900352).
- [151] K.R. Rao, D.N. Kim, and J.-J. Hwang. *Fast Fourier Transform - Algorithms and Applications*. Springer Netherlands, 2010. DOI: [10.1007/978-1-4020-6629-0](https://doi.org/10.1007/978-1-4020-6629-0).
- [152] B.S. Reddy and B.N. Chatterji. An FFT-based technique for translation, rotation, and scale-invariant image registration. *IEEE Transactions on Image Processing*, 5: 1266–1271, 1996. DOI: [10.1109/83.506761](https://doi.org/10.1109/83.506761).
- [153] M. Druckmüller. Phase correlation method for the alignment of total solar eclipse images. *The Astrophysical Journal*, 706:1605–1608, 2009.
DOI: [10.1088/0004-637x/706/2/1605](https://doi.org/10.1088/0004-637x/706/2/1605).
- [154] Inkscape Project. Inkscape. URL <https://inkscape.org>.

- [155] Hongjie Xie, Nigel Hicks, G. Randy Keller, Haitao Huang, and Vladik Kreinovich. An IDL/ENVI implementation of the FFT-based algorithm for automatic image registration. *Computers & Geosciences*, 29:1045–1055, 2003.
[DOI: 10.1016/s0098-3004\(03\)00104-3](https://doi.org/10.1016/s0098-3004(03)00104-3).
- [156] Jacqueline Le Moigne, Nathan S. Netanyahu, and Roger D. Eastman. *Image Registration for Remote Sensing*. Cambridge University Press, 2009.
[DOI: 10.1017/cbo9780511777684](https://doi.org/10.1017/cbo9780511777684).
- [157] H. Foroosh, J.B. Zerubia, and M. Berthod. Extension of phase correlation to subpixel registration. *IEEE Transactions on Image Processing*, 11:188–200, 2002.
[DOI: 10.1109/83.988953](https://doi.org/10.1109/83.988953).
- [158] M. Guizar-Sicairos, S. T. Thurman, and J. R. Fienup. Efficient subpixel image registration algorithms. *Optics Letters*, 33:156, 2008. [DOI: 10.1364/ol.33.000156](https://doi.org/10.1364/ol.33.000156).
- [159] Cai Ling Wang, Chun Xia Zhao, and Jing Yu Yang. Local upsampling fourier transform for high accuracy image rotation estimation. *Advanced Materials Research*, 268-270: 1488–1493, 2011. [DOI: 10.4028/www.scientific.net/amr.268-270.1488](https://doi.org/10.4028/www.scientific.net/amr.268-270.1488).
- [160] V. N. Dvornychenko. Bounds on (deterministic) correlation functions with application to registration. *IEEE Transactions on Pattern Analysis and Machine Intelligence*, 5: 206–213, 1983. [DOI: 10.1109/tpami.1983.4767373](https://doi.org/10.1109/tpami.1983.4767373).
- [161] Jaime Almonacid-Caballer, Josep Pardo-Pascual, and Luis Ruiz. Evaluating fourier cross-correlation sub-pixel registration in landsat images. *Remote Sensing*, 9:1051, 2017. [DOI: 10.3390/rs9101051](https://doi.org/10.3390/rs9101051).
- [162] Manuel Guizar-Sicairos, Samuel T. Thurman, and James R. Fienup. Efficient image registration algorithms for computation of invariant error metrics. In *Adaptive Optics: Analysis and Methods/Computational Optical Sensing and Imaging/Information Photonics/Signal Recovery and Synthesis Topical Meetings on CD-ROM*. OSA, 2007. [DOI: 10.1364/srs.2007.smc3](https://doi.org/10.1364/srs.2007.smc3).
- [163] R. A. Reed. Comparison of subpixel phase correlation methods for image registration. Technical report, 2010.
- [164] Amr Yousef, Jiang Li, and Mohammad Karim. High-speed image registration algorithm with subpixel accuracy. *IEEE Signal Processing Letters*, 22:1796–1800, 2015. [DOI: 10.1109/lsp.2015.2437881](https://doi.org/10.1109/lsp.2015.2437881).
- [165] P. J. Withers. Strain measurement by digital image correlation. *Strain*, 44:421–422, 2008. [DOI: 10.1111/j.1475-1305.2008.00556.x](https://doi.org/10.1111/j.1475-1305.2008.00556.x).
- [166] S. Yaofeng and J. H.L. Pang. Study of optimal subset size in digital image correlation of speckle pattern images. *Optics and Lasers in Engineering*, 45:967–974, 2007. [DOI: 10.1016/j.optlaseng.2007.01.012](https://doi.org/10.1016/j.optlaseng.2007.01.012).
- [167] H. W. Schreier and M. A. Sutton. Systematic errors in digital image correlation due to undermatched subset shape functions. *Experimental Mechanics*, 42:303–310, 2002. [DOI: 10.1007/bf02410987](https://doi.org/10.1007/bf02410987).

- [168] H. W. Schreier. Systematic errors in digital image correlation caused by intensity interpolation. *Optical Engineering*, 39:2915, 2000. DOI: [10.1117/1.1314593](https://doi.org/10.1117/1.1314593).
- [169] P. Hung and A. S. Voloshin. In-plane strain measurement by digital image correlation. *Journal of the Brazilian Society of Mechanical Sciences and Engineering*, 25, 2003. DOI: [10.1590/s1678-58782003000300001](https://doi.org/10.1590/s1678-58782003000300001).
- [170] Y. Q. Wang, M. A. Sutton, H. A. Bruck, and H. W. Schreier. Quantitative error assessment in pattern matching: Effects of intensity pattern noise, interpolation, strain and image contrast on motion measurements. *Strain*, 45:160–178, 2009. DOI: [10.1111/j.1475-1305.2008.00592.x](https://doi.org/10.1111/j.1475-1305.2008.00592.x).
- [171] M. et al. Bornert. Assessment of digital image correlation measurement errors: Methodology and results. *Experimental Mechanics*, 49:353–370, 2008. DOI: [10.1007/s11340-008-9204-7](https://doi.org/10.1007/s11340-008-9204-7).
- [172] J.C. Dupré, M. Bornert, L. Robert, and B. Watrisse. Digital image correlation: displacement accuracy estimation. *EPJ Web of Conferences*, 6:31006, 2010. DOI: [10.1051/epjconf/20100631006](https://doi.org/10.1051/epjconf/20100631006).
- [173] B. Pan, K. Qian, H. Xie, and A. Asundi. On errors of digital image correlation due to speckle patterns. In X. He, H. Xie, and Y. Kang, editors, *ICEM 2008: International Conference on Experimental Mechanics 2008*, 2008. DOI: [10.1111/12.839326](https://doi.org/10.1111/12.839326).
- [174] T. Hua, H. Xie, S. Wang, Z. Hu, P. Chen, and Q. Zhang. Evaluation of the quality of a speckle pattern in the digital image correlation method by mean subset fluctuation. *Optics & Laser Technology*, 43:9–13, 2011. DOI: [10.1016/j.optlastec.2010.04.010](https://doi.org/10.1016/j.optlastec.2010.04.010).
- [175] C. Lane, R. L. Burguete, and A. Shterenlikht. An objective criterion for the selection of an optimum dic pattern and subset size. In *Proceedings of the SEM XI international congress and exposition on experimental and applied mechanics*, 2008.
- [176] G. Crammond, S. W. Boyd, and J. M. Dulieu-Barton. Speckle pattern quality assessment for digital image correlation. *Optics and Lasers in Engineering*, 51: 1368–1378, 2013. DOI: [10.1016/j.optlaseng.2013.03.014](https://doi.org/10.1016/j.optlaseng.2013.03.014).
- [177] C. E. Shannon. A mathematical theory of communication. *Bell System Technical Journal*, 27:379–423, 1948. DOI: [10.1002/j.1538-7305.1948.tb01338.x](https://doi.org/10.1002/j.1538-7305.1948.tb01338.x).
- [178] O. Duda and E. H. Peter. Pattern classification and scene analysis. *Artificial Intelligence*, 4:139–143, 1973. DOI: [10.1016/0004-3702\(73\)90004-0](https://doi.org/10.1016/0004-3702(73)90004-0).
- [179] R. C. Gonzalez, R. E. Woods, and B. R. Masters. Digital image processing, third edition. *Journal of Biomedical Optics*, 14:029901, 2009. DOI: [10.1117/1.3115362](https://doi.org/10.1117/1.3115362).
- [180] R. Brunelli and T. Poggio. Face recognition: features versus templates. *IEEE Transactions on Pattern Analysis and Machine Intelligence*, 15:1042–1052, 1993. DOI: [10.1109/34.254061](https://doi.org/10.1109/34.254061).

- [181] D. Lecompte, S. Bossuyt, S. Cooreman, H. Sol, and J. Vantomme. Study and generation of optimal speckle patterns for dic. In *Proceedings of the SEM annual conference and exposition on experimental and applied mechanics*, 2007.
- [182] G. Stoilov, V. Kavardzhikov, and D. Pashkouleva. A comparative study of random patterns for digital image correlation. *Journal of Theoretical and Applied Mechanics*, 42:55–66, 2012.
- [183] Toru Yoshizawa, editor. *Handbook of Optical Metrology*. CRC Press, jul 2017.
DOI: [10.1201/b18328](https://doi.org/10.1201/b18328).
- [184] Devin K. Harris, John M. Civitillo, and Amir Gheitasi. Performance and behavior of hybrid composite beam bridge in virginia: Live load testing. *Journal of Bridge Engineering*, 21:04016022, 2016. DOI: [10.1061/\(ASCE\)BE.1943-5592.0000820](https://doi.org/10.1061/(ASCE)BE.1943-5592.0000820).
- [185] J. Antoš and V. Nežerka. Rtcrr: Real-time digital image correlation sofware, <https://github.com/jacobantos/rtcorr>. *CTU in Prague*, 2018.
- [186] V. Nežerka. Ncorr_post: Instruction manual, http://mech.fsv.cvut.cz/~nezerka/dic/_files/ncorr_post20-20manual.pdf. *CTU in Prague*, 2014.
- [187] Bing Pan. Digital image correlation for surface deformation measurement: historical developments, recent advances and future goals. *Measurement Science and Technology*, 29:082001, 2018. DOI: [10.1088/1361-6501/aac55b](https://doi.org/10.1088/1361-6501/aac55b).
- [188] Yuan Xue, Teng Cheng, Xiaohai Xu, Zeren Gao, Qianqian Li, Xiaojing Liu, Xing Wang, Rui Song, Xiangyang Ju, and Qingchuan Zhang. High-accuracy and real-time 3d positioning, tracking system for medical imaging applications based on 3d digital image correlation. *Optics and Lasers in Engineering*, 88:82–90, 2017.
DOI: [10.1016/j.optlaseng.2016.07.002](https://doi.org/10.1016/j.optlaseng.2016.07.002).
- [189] Bing Pan, Zixing Lu, and Huimin Xie. Mean intensity gradient: An effective global parameter for quality assessment of the speckle patterns used in digital image correlation. *Optics and Lasers in Engineering*, 48:469–477, 2010.
DOI: [10.1016/j.optlaseng.2009.08.010](https://doi.org/10.1016/j.optlaseng.2009.08.010).
- [190] J. R. Fienup. Reconstruction of an object from the modulus of its fourier transform. *Optics Letters*, 3:27–29, 1978. DOI: [10.1364/ol.3.000027](https://doi.org/10.1364/ol.3.000027).
- [191] J. R. Fienup. Phase retrieval algorithms: a comparison. *Applied Optics*, 21:2758–2769, 1982. DOI: [10.1364/ao.21.002758](https://doi.org/10.1364/ao.21.002758).
- [192] J.M. Kennedy and T.B. Belytschko. Theory and application of a finite element method for arbitrary lagrangian-eulerian fluids and structures. *Nuclear Engineering and Design*, 68:129–146, 1982. DOI: [10.1016/0029-5493\(82\)90026-7](https://doi.org/10.1016/0029-5493(82)90026-7).
- [193] H. Xiao, O.T. Bruhns, and A. Meyers. Direct relationship between the lagrangean logarithmic strain and the lagrangean stretching and the lagrangean kirchhoff stress. *Mechanics Research Communications*, 25:59–67, 1998.
DOI: [10.1016/s0093-6413\(98\)00007-x](https://doi.org/10.1016/s0093-6413(98)00007-x).

- [194] Yue Wu, Yicong Zhou, George Saveriades, Sos Agaian, Joseph P. Noonan, and Premkumar Natarajan. Local shannon entropy measure with statistical tests for image randomness. *Information Sciences*, 222:323–342, 2013.
[DOI: 10.1016/j.ins.2012.07.049](https://doi.org/10.1016/j.ins.2012.07.049).
- [195] Qinwei Ma and Shaopeng Ma. Experimental investigation of the systematic error on photomechanic methods induced by camera self-heating. *Optics Express*, 21:7686, 2013. [DOI: 10.1364/oe.21.007686](https://doi.org/10.1364/oe.21.007686).
- [196] P. L. Reu, E. Toussaint, E. Jones, H. A. Bruck, M. Iadicola, R. Balcaen, D. Z. Turner, T. Siebert, P. Lava, and M. Simonsen. DIC challenge: Developing images and guidelines for evaluating accuracy and resolution of 2D analyses. *Experimental Mechanics*, 58:1067–1099, 2017. [DOI: 10.1007/s11340-017-0349-0](https://doi.org/10.1007/s11340-017-0349-0).
- [197] R. Harilal and M. Ramji. Adaptation of open source 2d dic software ncorr for solid mechanics applications. *9th International Symposium on Advanced Science and Technology in Experimental Mechanics*, 2014. [DOI: 10.13140/2.1.4994.1442](https://doi.org/10.13140/2.1.4994.1442).
- [198] Jan Winkler and Chris Hendy. Improved structural health monitoring of london’s docklands light railway bridges using digital image correlation. *Structural Engineering International*, 27:435–440, 2017. [DOI: 10.2749/101686617x14881937384648](https://doi.org/10.2749/101686617x14881937384648).
- [199] Sinan Acikgoz, Matthew J. DeJong, and Kenichi Soga. Sensing dynamic displacements in masonry rail bridges using 2D digital image correlation. *Structural Control and Health Monitoring*, 25:e2187, 2018. [DOI: 10.1002/stc.2187](https://doi.org/10.1002/stc.2187).
- [200] Abe Davis, Michael Rubinstein, Neal Wadhwa, Gautham J. Mysore, Frédo Durand, and William T. Freeman. The visual microphone. *ACM Transactions on Graphics*, 33:1–10, 2014. [DOI: 10.1145/2601097.2601119](https://doi.org/10.1145/2601097.2601119).
- [201] E.V. Bohn. Modal functions for continuous-time MIMO parameter and state estimation. *IFAC Proceedings Volumes*, 21:927–930, 1988. [DOI: 10.1016/s1474-6670\(17\)54847-8](https://doi.org/10.1016/s1474-6670(17)54847-8).
- [202] Javad Baqersad, Peyman Poozesh, Christopher Niezrecki, and Peter Avitabile. Comparison of modal parameters extracted using MIMO, SIMO, and impact hammer tests on a three-bladed wind turbine. In *Topics in Modal Analysis II, Volume 8*, pages 185–197. Springer International Publishing, 2014.
[DOI: 10.1007/978-3-319-04774-4_19](https://doi.org/10.1007/978-3-319-04774-4_19).
- [203] Aral Sarrafi and Zhu Mao. Probabilistic uncertainty quantification of wavelet-transform-based structural health monitoring features. In Tribikram Kundu, editor, *Health Monitoring of Structural and Biological Systems 2016*. SPIE, 2016.
[DOI: 10.1111/12.2222048](https://doi.org/10.1111/12.2222048).
- [204] Peyman Poozesh, Kai Aizawa, Christopher Niezrecki, Javad Baqersad, Murat Inalpolat, and Gunnar Heilmann. Structural health monitoring of wind turbine blades using acoustic microphone array. *Structural Health Monitoring: An International Journal*, 16:471–485, 2016. [DOI: 10.1177/1475921716676871](https://doi.org/10.1177/1475921716676871).

- [205] Dongming Feng and Maria Q. Feng. Experimental validation of cost-effective vision-based structural health monitoring. *Mechanical Systems and Signal Processing*, 88:199–211, 2017. [DOI: 10.1016/j.ymssp.2016.11.021](https://doi.org/10.1016/j.ymssp.2016.11.021).
- [206] Shervin Tashakori, Amin Baghalian, Muhammet Unal, Hadi Fekrmandi, volkan y şenyürek, Dwayne McDaniel, and Ibrahim N. Tansel. Contact and non-contact approaches in load monitoring applications using surface response to excitation method. *Measurement*, 89:197–203, 2016. [DOI: 10.1016/j.measurement.2016.04.013](https://doi.org/10.1016/j.measurement.2016.04.013).
- [207] Alberto Lavatelli and Emanuele Zappa. Modeling uncertainty for a vision system applied to vibration measurements. *IEEE Transactions on Instrumentation and Measurement*, 65:1818–1826, 2016. [DOI: 10.1109/tim.2016.2541359](https://doi.org/10.1109/tim.2016.2541359).
- [208] T. Lundstrom, J. Baqersad, and C. Niezrecki. Monitoring the dynamics of a helicopter main rotor with high-speed stereophotogrammetry. *Experimental Techniques*, 40: 907–919, 2016. [DOI: 10.1007/s40799-016-0092-y](https://doi.org/10.1007/s40799-016-0092-y).
- [209] Javad Baqersad, Peyman Poozesh, Christopher Niezrecki, and Peter Avitabile. Photogrammetry and optical methods in structural dynamics – a review. *Mechanical Systems and Signal Processing*, 86:17–34, 2017. [DOI: 10.1016/j.ymssp.2016.02.011](https://doi.org/10.1016/j.ymssp.2016.02.011).
- [210] Peyman Poozesh, Javad Baqersad, Christopher Niezrecki, Peter Avitabile, Eric Harvey, and Rahul Yarala. Large-area photogrammetry based testing of wind turbine blades. *Mechanical Systems and Signal Processing*, 86:98–115, 2017. [DOI: 10.1016/j.ymssp.2016.07.021](https://doi.org/10.1016/j.ymssp.2016.07.021).
- [211] Fadi A. Ghaith and MD F. Haque. Elastodynamic modeling and simulation of the Airbus A380 wing. In *Volume 8: 26th Conference on Mechanical Vibration and Noise*. American Society of Mechanical Engineers, 2014. [DOI: 10.1115/detc2014-34010](https://doi.org/10.1115/detc2014-34010).
- [212] O.V. Bocharova, I.E. Andzjikovich, A.V. Sedov, and V.V. Kalinchuk. An effective method of signal processing in problems of low-frequency defectoscopy. *Procedia Engineering*, 199:2034–2039, 2017. [DOI: 10.1016/j.proeng.2017.09.469](https://doi.org/10.1016/j.proeng.2017.09.469).
- [213] Ulrika Lagerblad, Henrik Wentzel, and Artem Kulachenko. Dynamic response identification based on state estimation and operational modal analysis. *Mechanical Systems and Signal Processing*, 129:37–53, 2019. [DOI: 10.1016/j.ymssp.2019.04.019](https://doi.org/10.1016/j.ymssp.2019.04.019).
- [214] J. Antoš, V. Nežerka, and M. Somr. Real-time optical measurement of displacements using subpixel image registration. *Experimental Techniques*, 43:315–323, 2019. [DOI: 10.1007/s40799-019-00315-1](https://doi.org/10.1007/s40799-019-00315-1).
- [215] Z. Prošek, V. Nežerka, R. Hlúžek, J. Trejbal, P. Tesárek, and G. Karra'a. Role of lime, fly ash, and slag in cement pastes containing recycled concrete fines. *Construction and Building Materials*, 201:702–714, 2019. [DOI: 10.1016/j.conbuildmat.2018.12.227](https://doi.org/10.1016/j.conbuildmat.2018.12.227).
- [216] V. Nežerka, P. Havlásek, J. Antoš, and J. Trejbal. Mitigating inclusion-induced shrinkage cracking in cementitious composites by incorporating recycled concrete fines. *submitted to: Cement and Concrete Research*, 2019.